

# Bar-Driven AGN Growth

Izzy L. Garland



Physics

Department of Physics

Lancaster University

March 2024

A thesis submitted to Lancaster University for the degree of  
Doctor of Philosophy in the Faculty of Science and Technology

*Supervised by* Dr. Brooke D. Simmons

# Abstract

The co-evolution observed between supermassive black holes (SMBHs) and the galaxies that host them is poorly understood, and there are many unanswered questions. Until very recently, it was assumed that this co-evolution was driven by two or more galaxies merging, growing both the stellar mass of the galaxy and the SMBH mass. Whilst certainly a contributor to the co-evolution relationships, this theory does not account for the rapidly accreting SMBHs, also known as active galactic nuclei (AGN), observed in galaxies with merger-free histories. The majority of black hole growth has occurred in the absence of mergers, but determining the exact pathways remains elusive.

In this thesis, we examine the link between the presence of large-scale, galactic bars and AGN. We first use a sample of luminous, unobscured AGN in unambiguously disk-dominated galaxies, and we describe the spectroscopic data reduction. After carefully controlling for the confounding parameters of stellar mass ( $M_*$ ) and star formation rate, we look at the bar fraction in our sample and compare it to a controlled sample of inactive disk-dominated galaxies. We find that the bar fraction in the AGN hosts,  $f_{\text{bar}} = 0.59^{+0.08}_{-0.09}$ , is slightly higher than the inactive sample,  $f_{\text{bar}} = 0.44^{+0.08}_{-0.09}$ , however the two values are in agreement to within  $2\sigma$ , giving us nothing more than a tantalising hint at a correlation, and preventing us from drawing conclusions with any real certainty. It is worth noting that this small sample was able to reproduce similar levels of uncertainty as previous works, despite being a factor of 20 smaller, highlighting the progress that can be made with careful controlling and sample selection.

We then examine this potential correlation over a larger subset of the population of disk-dominated galaxies using GZ DESI. We identify a sample of disk galaxies, and separate them into strongly barred, weakly barred and unbarred, and we examine the AGN fraction in each. After controlling for  $M_*$  and  $(g - r)_0$  colour, we find that the AGN fraction in strongly barred galaxies,  $f_{\text{AGN,SBAR}} = 0.316 \pm 0.009$ , is greater than than in weakly barred galaxies,  $f_{\text{AGN,WBAR}} = 0.233 \pm 0.008$ , which is in turn greater than that in unbarred galaxies,  $f_{\text{AGN,UBAR}} = 0.142 \pm 0.006$ . These results are highly statistically significant, and resolve the decade-long debate on the correlation between large-scale galactic bars and AGN.

In summary, the work presented here demonstrates not only the existence of this correlation, but emphasises the importance of large-scale surveys combined with highly controlled, extreme samples to tease out robust results. This paves the way for future work to further investigate this correlation, and understand the physics behind it in greater detail.

To anyone who has been reprimanded for staring into space.

## Acknowledgements

There are so many people without whom this thesis wouldn't exist. I think if I thanked everyone by name I would still be writing the list now, but there are some particular people I want to mention.

Firstly, I would like to thank my supervisor. Brooke, you have been amazing! I could not have done this without your support, your encouragement and your approach to seeing the humans behind the science. Thank you for dealing with my off-topic brain wanderings, and for just smiling and sighing whenever I start a meeting with "So, I did a thing". Thanks as well to the rest of the Obs Astro Faculty, who make the department such a fun place to work, and are always happy to give advice.

Thank you to everyone in the Lancaster PhD office. Particular thanks must go to David, Jamie and Brenda – here's to many more taco nights!

To my family, thank you for always being so supportive, even when we're stuck hundreds of miles away in the midst of a global pandemic. Thank you for your understanding, your patience, and your kindness.

Getting through a PhD without friends would be an insurmountable task. Ruby, I could not have gotten through the lockdowns with any other flatmate. Even though we both lost braincells we didn't even know we had left, thank you for all of the times you've listened to rants about data reduction and spectral fitting, and offered much needed python assistance. Thank you to Bambi and Codie for Bake-Off nights, and Pokemon walks! Jen, thank for the times when you were always there for an emergency weekend away, dog and guinea pig snugs, or just trips to Walling's and the beach. Esme, thank you for listening to my problems without judgement, and always being ready to drop everything if I just wanted to talk.

To my Guiding friends, my fellow volunteers, thank you for unforgettable memories, from camping in non-stop rain, to sleepovers in the library, to making district meetings fun. You all remind me there is so much more to life than a PhD, and we can all make little changes all the time. Thank you especially to Abi for first getting me into volunteering and giving me a life outside uni, to Joanna for dealing with my abysmal admin skills before just taking them over, and to Marie for taking on our Guides, being a mentor to me from the day I started, and showing me that everything always works out in the end.

This research is in part based on observations made with the NASA/ESA Hubble Space Telescope, obtained at the Space Telescope Science Institute, which is operated by the Association of Universities for Research in Astronomy, Inc., under NASA contract NAS5-26555. These observations are associated with program HST-GO-14606.

Support for program HST-GO-14606 was provided by NASA through a grant from the Space Telescope Science Institute, which is operated by the Association of Universities for Research in Astronomy, Inc., under NASA contract NAS5-26555.

This research has made use of the Spanish Virtual Observatory (<https://svo.cab.inta-csic.es>) project funded by MCIN/AEI/10.13039/501100011033/ through grant PID2020-112949GB-I00 (Rodrigo et al., 2012; Rodrigo & Solano, 2020).

Funding for SDSS-III has been provided by the Alfred P. Sloan Foundation, the Participating Institutions, the National Science Foundation, and the U.S. Department of Energy Office of Science. The SDSS-III web site is <http://www.sdss3.org/>.

SDSS-III is managed by the Astrophysical Research Consortium for the Participating Institutions of the SDSS-III Collaboration including the University of Arizona, the Brazilian Participation Group, Brookhaven National Laboratory, Carnegie Mellon University, University of Florida, the French Participation Group, the German Participation Group, Harvard University, the Instituto de Astrofísica

de Canarias, the Michigan State/Notre Dame/JINA Participation Group, Johns Hopkins University, Lawrence Berkeley National Laboratory, Max Planck Institute for Astrophysics, Max Planck Institute for Extraterrestrial Physics, New Mexico State University, New York University, Ohio State University, Pennsylvania State University, University of Portsmouth, Princeton University, the Spanish Participation Group, University of Tokyo, University of Utah, Vanderbilt University, University of Virginia, University of Washington, and Yale University.

The DESI Legacy Imaging Surveys consist of three individual and complementary projects: the Dark Energy Camera Legacy Survey (DECaLS), the Beijing-Arizona Sky Survey (BASS), and the Mayall z-band Legacy Survey (MzLS). DECaLS, BASS and MzLS together include data obtained, respectively, at the Blanco telescope, Cerro Tololo Inter-American Observatory, NSF's NOIRLab; the Bok telescope, Steward Observatory, University of Arizona; and the Mayall telescope, Kitt Peak National Observatory, NOIRLab. NOIRLab is operated by the Association of Universities for Research in Astronomy (AURA) under a cooperative agreement with the National Science Foundation. Pipeline processing and analyses of the data were supported by NOIRLab and the Lawrence Berkeley National Laboratory (LBNL). Legacy Surveys also uses data products from the Near-Earth Object Wide-field Infrared Survey Explorer (NEOWISE), a project of the Jet Propulsion Laboratory/California Institute of Technology, funded by the National Aeronautics and Space Administration. Legacy Surveys was supported by: the Director, Office of Science, Office of High Energy Physics of the U.S. Department of Energy; the National Energy Research Scientific Computing Center, a DOE Office of Science User Facility; the U.S. National Science Foundation, Division of Astronomical Sciences; the National Astronomical Observatories of China, the Chinese Academy of Sciences and the Chinese National Natural Science Foundation. LBNL is managed by the Regents of the University of California under contract to the

U.S. Department of Energy. The complete acknowledgments can be found at <https://www.legacysurvey.org/acknowledgment/>.

The data in this paper are the result of the efforts of the Galaxy Zoo volunteers, without whom none of this work would be possible. Their efforts are individually acknowledged at <http://authors.galaxyzoo.org>.

This research has made use of Topcat (Taylor, 2005), an interactive graphical tool for analysis and manipulation of tabular data.

This research has made use of SAOImage DS9 (Joye & Mandel, 2003), an astronomical imaging and data visualisation application.

This research has made extensive use of the following Python packages:

- **Astropy**, a community-developed core Python package for Astronomy (Astropy Collaboration et al., 2013, 2018, 2022).
- **Matplotlib**, a 2D graphics package for Python (Hunter, 2007).
- **Numpy**, a package for scientific computing (Harris et al., 2020).
- **Scipy**, a package for fundamental algorithms in scientific computing (Virtanen et al., 2020).

## **Declaration**

This thesis is my own work and no portion of the work referred to in this thesis has been submitted in support of an application for another degree or qualification at this or any other institute of learning.

---

“For my part I know nothing with any certainty, but the sight of the stars makes me dream.”  
– *Vincent van Gogh*

# Contents

<b>List of Figures</b>	<b>xi</b>
<b>1 Introduction</b>	<b>1</b>
1.1 Galaxies . . . . .	1
1.1.1 Galaxy Observations . . . . .	3
1.1.1.1 Imaging and Spectroscopy . . . . .	3
1.1.1.2 The Sloan Digital Sky Survey . . . . .	6
1.1.1.3 DESI Legacy Surveys . . . . .	7
1.1.2 Morphological Components . . . . .	8
1.1.2.1 Central Bulge and Elliptical Galaxies . . . . .	8
1.1.2.2 Galactic Disk . . . . .	10
1.1.2.3 Large-Scale Galactic Bars . . . . .	11
1.1.3 Classifying Morphology . . . . .	14
1.1.3.1 Galaxy Zoo and Galaxy Zoo 2 . . . . .	14
1.1.3.2 GZ DESI . . . . .	19
1.1.3.3 AGN Contamination . . . . .	22
1.2 Active Galactic Nuclei . . . . .	22
1.2.1 AGN structure . . . . .	22
1.2.2 AGN Identification . . . . .	24
1.2.2.1 BPT Diagrams . . . . .	25
1.2.2.2 Infrared and X-Ray Identification . . . . .	28
1.2.2.3 Radio Identification . . . . .	29
1.2.3 BH–Galaxy Co-evolution . . . . .	30
1.2.3.1 Switch On and Fuelling . . . . .	32

---

1.2.3.2	Feedback . . . . .	33
<b>2</b>	<b>Reduction of the Shane/Kast Data</b>	<b>35</b>
2.1	Introduction . . . . .	35
2.2	Reduction . . . . .	39
2.2.1	Overscan, Biases and Flats . . . . .	39
2.2.2	CCD Calibration . . . . .	40
2.2.3	Background Subtraction . . . . .	41
2.2.4	Flux Calibration . . . . .	42
2.2.5	Extraction of 1D Spectra . . . . .	43
2.3	Analysis of the Spectra . . . . .	45
2.3.1	Redshift Determination . . . . .	45
2.3.2	Fitting the spectra and accounting for AGN flux leakage . . . . .	45
<b>3</b>	<b>The most luminous, merger-free AGN show only marginal correlation with bar presence</b>	<b>48</b>
3.1	Introduction . . . . .	49
3.2	Sample and Observations . . . . .	53
3.2.1	AGN-host Sample . . . . .	53
3.2.2	Inactive Sample . . . . .	53
3.2.3	Data Reduction and Fitting . . . . .	55
3.2.3.1	Lick Data Reduction . . . . .	55
3.2.3.2	Spectral Fitting . . . . .	56
3.2.3.3	<i>HST</i> Data Reduction and Photometric Fitting . . . . .	59
3.2.4	Bar presence . . . . .	63
3.2.5	Bulge Classification . . . . .	64
3.3	Stellar properties of the samples . . . . .	65
3.3.1	Stellar Mass . . . . .	65
3.3.2	Star Formation Rate . . . . .	67
3.3.2.1	Dealing with upper limits . . . . .	68
3.4	Star Formation in Merger-Free AGN hosts . . . . .	74
3.5	Bar Fractions of AGN-host vs Inactive disks . . . . .	78
3.6	Conclusions . . . . .	82

---

<b>4 Galaxy Zoo DESI: large-scale bars as a secular mechanism for triggering AGN</b>	<b>84</b>
4.1 Introduction . . . . .	85
4.2 Data Collation . . . . .	87
4.2.1 Sample Selection . . . . .	87
4.2.2 Morphology Classification . . . . .	88
4.2.3 Activity Classification . . . . .	91
4.3 Results . . . . .	95
4.3.1 AGN–bar correlation with stellar mass and colour . . . . .	97
4.4 Discussion . . . . .	102
4.5 Conclusions . . . . .	105
<b>5 Conclusions</b>	<b>107</b>
5.1 Future Work . . . . .	111
<b>Appendix A Glossary</b>	<b>114</b>
<b>Appendix B Chapter 2</b>	<b>116</b>
<b>Appendix C Chapter 3</b>	<b>136</b>
C.1 SDSS thumbnails . . . . .	136
C.2 <i>HST</i> thumbnails . . . . .	136
<b>Appendix D Chapter 4</b>	<b>139</b>
D.1 Subsample Counts . . . . .	139
D.2 Full stellar mass and colour distributions . . . . .	139
<b>References</b>	<b>142</b>

# List of Figures

1.1	The Hubble Sequence . . . . .	2
1.2	SDSS filter profiles . . . . .	4
1.3	Galaxy Zoo 2 question tree . . . . .	16
1.4	Galaxy Zoo DECaLS question tree . . . . .	21
1.5	Active galactic nucleus structure . . . . .	23
1.6	Example BPT diagrams . . . . .	26
1.7	The star formation and black hole accretion history . . . . .	31
2.1	The Shane Telescope and Kast Double Spectrograph . . . . .	38
2.2	Example galaxy with the region observed with longslit spectroscopy	44
2.3	Example fits to AGN and galaxy spectra over different wavelength ranges . . . . .	46
3.1	Full example spectra of J081324.00+542236.9 AGN, galaxy, and variance . . . . .	57
3.2	Fitted spectra over H $\alpha$ region for AGN and galaxy . . . . .	58
3.3	The fraction of the flux contained within the PSF for both <i>HST</i> and SDSS . . . . .	61
3.4	SFR against $M_*$ , for AGN hosts and the inactive comparison sample	75
3.5	$M_*$ and SFR distributions of AGN hosts and inactive comparison sample after controlling for $M_*$ . . . . .	77
3.6	$M_*$ and SFR distributions of AGN hosts and inactive comparison sample after controlling for $M_*$ and SFR, split by bar presence . .	79
4.1	Absolute $r$ -band magnitude against redshift . . . . .	89

---

4.2	Classification of disk-dominated sources on a trio of BPT diagrams	90
4.3	Examples of each morphology and activity classification . . . . .	94
4.4	The distributions in $M_*$ and $(g-r)_0$ colour for a variety of subsamples	96
4.5	The distribution of activity classification within each bar category	98
4.6	The difference between the AGN fraction in two bar categories for every combination of SBAR, WBAR and UBAR . . . . .	99
4.7	The distributions of the median difference between AGN fractions, and the fraction of bins where one bar type are more prevalent than another . . . . .	100
C.1	SDSS postage stamps of unambiguously disk-dominated AGN host galaxies . . . . .	137
C.2	<i>HST</i> postage stamps of unambiguously disk-dominated AGN host galaxies . . . . .	138
D.1	The distributions in $M_*$ and $(g-r)_0$ colour for a variety of subsamples, including for weakly barred galaxies . . . . .	141

## Relevant Publications by the Author

### Chapter 2+3

- “The most luminous, merger-free AGNs show only marginal correlation with bar presence”; **Garland, I.**, Fahey, M., Simmons, B., Smethurst, R., Lintott, C., Shanahan, J., Silcock, M., Smith, J., Keel, W., Coil, A., Geron, T., Kruk, S., Masters, K., O’Ryan, D., Thorne, M., Wiersema, K. **2023**, [MNRAS, 522, 1](#).

### Chapter 4

- “Galaxy Zoo DESI: large-scale bars as a secular mechanism for triggering AGN”; **Garland, I.**, Walmsley, M., Silcock, M., Potts, L., Smith J., Simmons, B., Lintott, C., Smethurst, R., Dawson, J., Keel, W., Kruk, S., Mantha, K., Masters, K., O’Ryan, D., Popp, J., Thorne, M., **2024**, [MNRAS, 532, 2](#).

# Chapter 1

## Introduction

### 1.1 Galaxies

The first recorded observation of a galaxy, Andromeda, was by Abd al-Rahman al-Sūfī in his Book Of Fixed Stars (al Sūfī, 964), although its status as a galaxy would not be confirmed for almost a thousand years. It was not until Hubble (1926) that, via the observation of Cepheids, Andromeda was confirmed to be outside of our own Milky Way. Hubble (1926) observed 400 ‘extragalactic nebulae’ (as they were then known) and classified them into a number of types based on their overall shape, in a system known as the Hubble Sequence (Figure 1.1, Hubble, 1936).

Broad visual classification of galaxies into this scheme is still widely used, and is often combined with citizen science and machine learning techniques (*e.g.*, Lintott et al., 2008; Walmsley et al., 2023a). We rely heavily on the observed morphology of a galaxy to inform us about the stellar dynamics, which are challenging to observe directly due to the required on-sky time. Understanding the dynamics can then aid us in developing a well-backed theory for the transfer of material to the centre of a galaxy towards the supermassive black hole (SMBH), and from there how this material is accreted in such a way as to trigger an active galactic nucleus (AGN).

In this chapter, we discuss how galaxies can be observed (Section 1.1.1), what

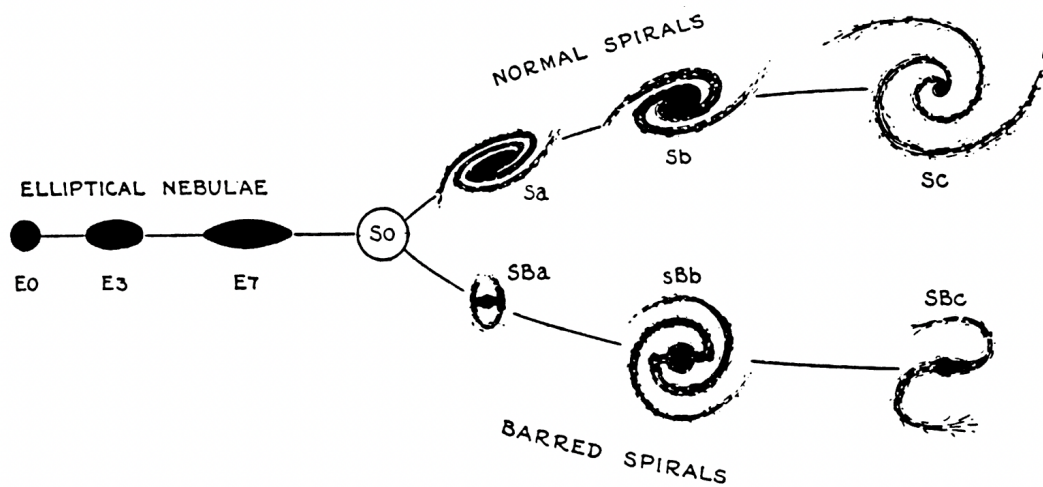


**Figure 1.1:** Taken from [Hubble \(1936\)](#). The Hubble Sequence shows the different morphologies of galaxies. Ellipticals are on the left, denoted with  $E_x$  where  $x$  represents the ellipticity of the galaxy.  $x = 0$  is more spheroidal, and  $x = 7$  is more flattened. Spiral galaxies are on the right, with unbarred spirals, denoted as  $S_y$  on the upper branch and barred spirals, denoted as  $SB_y$  on the lower branch.  $y$  represents the tightness of the spiral and prominence of the bulge, with  $y = a$  being tightly wound and a bright bulge, and  $y = c$  being loosely wound with a faint bulge. [de Vaucouleurs \(1959\)](#) added a fourth spiral category,  $y = d$ , which indicates very loosely wound spiral arms and negligible bulge.

information we can glean about the galactic dynamics from these observations (Section 1.1.2), and the classification methods used to identify the morphology (Section 1.1.3).

## 1.1.1 Galaxy Observations

### 1.1.1.1 Imaging and Spectroscopy

Broadly, the two ways that we observe a galaxy are through imaging (photometry), and spectroscopy. Although imaging is often quicker and easier to obtain, both are needed in order to garner a fuller understanding of the system. We cover both methods briefly here and note some key examples.

Photometry involves using a filter (usually referred to with an abbreviation such as a single letter or a short code) which allows photons within a specific wavelength range to pass through, and blocks light from other wavelengths. Naturally, transmission is imperfect, and every filter has its own transmission profile. In Figure 1.2, we show the filter profiles for the five Sloan Digital Sky Survey (SDSS; see Section 1.1.1.2) filters. These are all broadband filters, although narrowband filters also exist (which, as the name suggests, are more restrictive on the wavelengths that are allowed through). The data resulting from each image is thus limited in the wavelength information, but we can obtain the right ascension, the declination and the flux in each band at each pixel. Different features from galaxies appear brightest in different wavelengths. For example, most stellar activity is revealed in optical filters, but to trace dust infrared filters must be used.

Spectroscopy means that the light from the source is dispersed through a prism or grating before reaching the detector, and thus we can see how the intensity of the flux varies with wavelength. With high enough spectral resolution, we can measure how much emission is coming from specific atomic, ionic and molecular species, as well as the velocity of these various components. This allows for far more accurate insights into the contents of a galaxy. Here, we cover a few key emission lines utilised in this work that can be measured from optical spectroscopy.

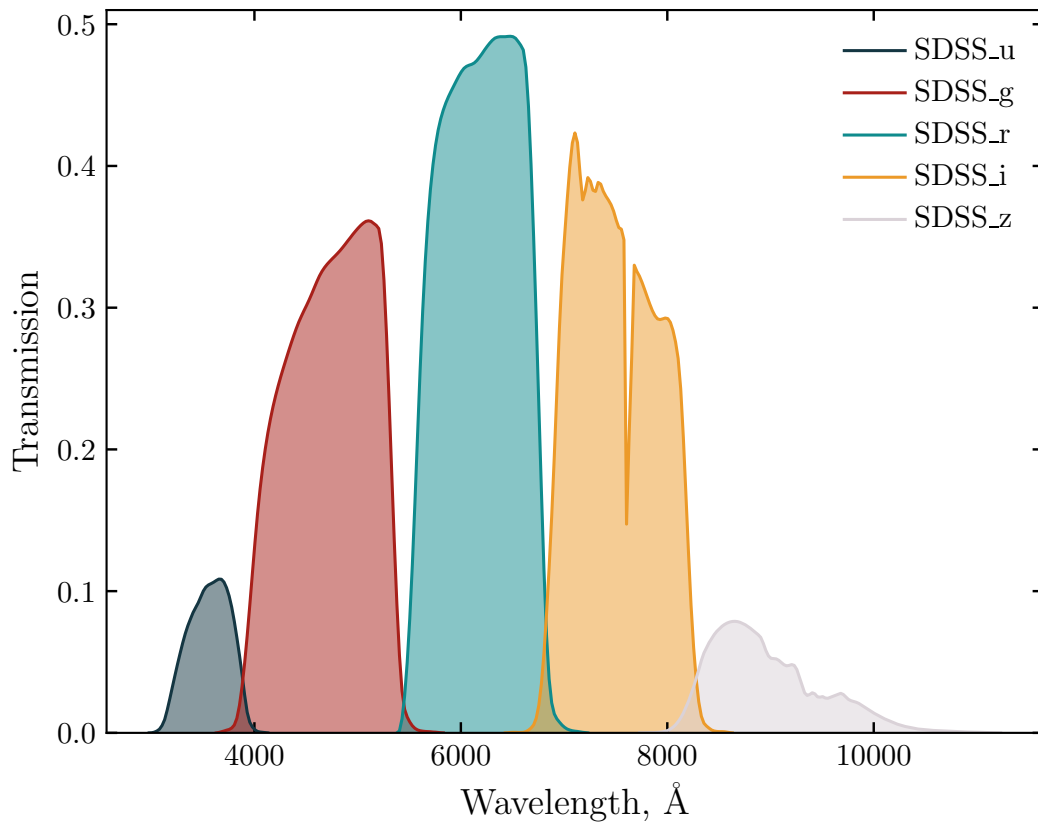


**Figure 1.2:** The filter profiles of the five broad-band SDSS filters (Rodrigo et al., 2012; Rodrigo & Solano, 2020). The transmission shows the fraction of the light incident on the filter with that wavelength that can be transmitted. SDSS covers the optical and Near-Infrared (NIR) region of the electromagnetic spectrum. Note that SDSS does not cover the full infrared regime.

- 
- **Hydrogen.** The two hydrogen lines used in this thesis are  $H\alpha$  and  $H\beta$ .  $H\alpha$  has a peak at  $6563 \text{ \AA}$ , and its emission occurs when an electron in a hydrogen atom transfers from the third energy level to the second ( $n = 3 \rightarrow 2$ ), making it part of the Balmer series.  $H\alpha$  is one of the brightest hydrogen lines. The other transition we utilise in the Balmer series,  $H\beta$ , is a transition from the fourth to the second energy level ( $n = 4 \rightarrow 2$ ), and occurs at a wavelength of  $4861 \text{ \AA}$ , meaning it is a higher energy transition than  $H\alpha$ . We use  $H\alpha$  here to determine star formation rates, since it can trace the ionised gas surrounding young stars. By measuring the ratio of  $H\alpha$  to  $H\beta$ , the Balmer decrement, this can allow calculation of how much  $H\alpha$  is being attenuated by dust. Both of these hydrogen lines are also used to determine whether a source is an active galactic nucleus, a star-forming galaxy (SFG), a low-ionisation nuclear emission line region (LINER), composite (a mix between AGN and SFG), or ‘undetermined’. See Section 1.2.2 for more detail on how this is done, using the emission lines below as well.
  - **Nitrogen.**  $[\text{NII}]\lambda\lambda 6548 \text{ \AA}, 6584 \text{ \AA}$  is a transition observed in singly-ionised nitrogen, appearing as a doublet due to the fine structure in the ion.  $[\text{NII}]$  is a forbidden transition, meaning that it requires very low gas densities to occur, such as those found in interstellar medium. This is because it takes a long time (on the order of a second, compared to an allowed transition’s  $10^{-8}$  seconds) to occur spontaneously, and thus in higher density environments a collision is likely to occur with another atom before the transition happens. Since the doublet fluxes always appear in a strict ratio, we only require constraints of one peak to determine the constraints of the other. We primarily use the  $6584 \text{ \AA}$  peak.
  - **Oxygen.** The two oxygen emission lines we use in this thesis are  $[\text{OI}]\lambda 6300 \text{ \AA}$  and  $[\text{OIII}]\lambda\lambda 4959 \text{ \AA}, 5007 \text{ \AA}$ . As with  $[\text{NII}]$ , these are both also forbidden transitions, although this time in the oxygen neutral atom and in doubly-ionised oxygen respectively. The doublet in  $[\text{OIII}]$  occurs in a well-known ratio, similar to  $[\text{NII}]$ , so again we only need constraints on one peak to obtain constraints for both. We primarily use the  $5007 \text{ \AA}$  peak.

- **Sulphur.** The transition we observe from sulphur is  $[\text{SII}]\lambda\lambda 6717 \text{ \AA}, 6731 \text{ \AA}$ . Although this also occurs as a doublet, the two peaks do not occur in any specific ratio, and thus both are required to understand the total flux from this transition. Like  $[\text{NII}]$  and  $[\text{OIII}]$ ,  $[\text{SII}]$  is a forbidden transition.

There are a number of challenges posed by the fact that each of these emission lines can occur in a varying environments due to varying causes, so commonly emission line ratios are used. The ratios at which these emission lines occur in are often highly sensitive to temperature, pressure, density, hardness of the ionisation field, and so can be used as diagnostics for the main power sources in a galaxy (see Section 1.2.2).

#### 1.1.1.2 The Sloan Digital Sky Survey

With operations beginning in 2000, the Sloan Digital Sky Survey (SDSS; York et al., 2000) has been observing the sky for over two decades. A number of facilities are used to conduct SDSS, primarily the Sloan 2.5 m telescope at Apache Point Observatory (APO), which was the sole facility for a number of years.

The initial aim was to obtain optical photometry of 10,000 square degrees of sky in five bands ( $u$ ,  $g$ ,  $r$ ,  $i$  and  $z$ ), and spectra of 100,000 quasars and 1 million galaxies. There have now been five generations of SDSS, styled as SDSS-I, SDSS-II, SDSS-III, SDSS-IV, and SDSS-V, spread out over 18 data releases (at the time of writing) and comprising of a large number of sub-programmes. The data release we predominantly make use of in this thesis is DR7 (Abazajian et al., 2009).

DR7 marks the end of SDSS-II, and contains around 357 million unique photometric objects over  $11,663 \text{ deg}^2$  and 1.6 million fibre spectra (comprising of 930,000 galaxies, 120,000 quasars and 460,000 stars) over  $9,380 \text{ deg}^2$ . This means that spectroscopy is complete for a large area of the North Galactic Cap (NGC). The programme achieved 95% completeness limits in the photometric images of AB magnitudes 22.0, 22.2, 22.2, 21.3 and 20.5 in  $u$ ,  $g$ ,  $r$ ,  $i$  and  $z$  filters respectively, with an approximate pixel scale of  $0''.396/\text{px}$ .

### 1.1.1.3 DESI Legacy Surveys

The Dark Energy Spectroscopic Instrument (DESI) is installed on the Mayall 4 m telescope at Kitt Peak National Observatory (KPNO), and will measure redshifts of 35 million galaxies and quasars in order to provide constraints on the equation of state of dark matter (DESI Collaboration et al., 2016, 2022). The DESI Legacy Surveys (DESI-LS) are designed to select targets to be observed by DESI.

DESI-LS combines three different projects in order to maximise data collection in a suitable time span for DESI to commence. These are: the Dark Energy Camera Legacy Survey (DECaLS), the Beijing-Arizona Sky Survey (BASS), and the Mayall  $z$ -band Legacy Survey (MzLS). DECaLS uses the Blanco 4 m telescope at the Cerro Tololo Inter-American Observatory, BASS uses the Bok 90 inch telescope at KPNO, and MzLS uses the Mayall 4 m telescope (where DESI is installed). These three surveys together result in two regions of the sky with wide coverage – the NGC, which spans  $9,900 \text{ deg}^2$ , and the South Galactic Cap (SGC), which spans  $4,400 \text{ deg}^2$ .

Given the goals of DESI, this places a number of requirements on DESI-LS. These requirements are laid out in Appendix A of Dey et al. (2019), but the key components are: DESI-LS must image  $14,000 \text{ deg}^2$  of the sky, in three bands, to depths of  $g = 24.0$ ,  $r = 23.4$  and  $z = 22.5$ , the  $z$ -band image PSF must be smaller than  $1.5''$  FWHM (full-width-half-maximum), and the targets must be visible from KPNO.

These requirements were achieved with the publication of DR8<sup>1</sup>, which also includes data from the Dark Energy Camera (DECam) and from non-DECaLS surveys, notably the Dark Energy Survey (DES).

DES is not part of DESI-LS, since its footprint is too far south to be observed from KPNO. However, given that it uses the same instrumentation as DECaLS, it is included in DESI-LS data releases.

At the time of writing, DESI-LS DR10<sup>2</sup> (the most recent data release) contains around 2.8 billion unique sources, with a pixel scale of  $0''.262/\text{px}$ , over  $19,437 \text{ deg}^2$  covered in all bands (although some individual bands have up to  $21,619 \text{ deg}^2$ ). The reported seeing is  $1.5''$ .

<sup>1</sup>Available at <https://www.legacysurvey.org/dr8/>

<sup>2</sup>Available at <https://www.legacysurvey.org/dr10/>

We discuss in Section 1.1.3.2 how we use a combination of citizen science and machine learning to classify the morphologies of the brightest galaxies in DESI-LS DR8.

## 1.1.2 Morphological Components

The term ‘stellar dynamics’ is used to describe the motion of the stars in a galaxy (which can be treated as point masses) under the influence of other stars. Other galactic components can also cause stellar motion, such as the supermassive black hole and dark matter halo. Obtaining the stellar dynamics directly is very costly to do, requiring many on-sky observing hours. Yet the morphology is an excellent tracer of the stellar dynamics (*e.g.*, Sandage et al., 1970; Sandage, 1986; Mo et al., 1998; D’Onghia et al., 2006; Falcón-Barroso et al., 2015; Rodriguez-Gomez et al., 2017), which could affect black hole growth (see Section 1.2.3.1). In this chapter, we discuss key components of morphology and their relation to the dynamics of the galaxy as a whole.

The motion of the stars in a galaxy can be decomposed into rotational velocity,  $v_{\text{rot}}$  and random velocities,  $\sigma$ , arising from random motion. Most galaxies will have at least some contribution from both  $v_{\text{rot}}$  and  $\sigma$ , but an elliptical galaxy or a central bulge is dominated by  $\sigma$ , and a disk component is dominated by  $v_{\text{rot}}$  (Binney & Merrifield, 1998).

### 1.1.2.1 Central Bulge and Elliptical Galaxies

The remarkable similarity between classical bulges and elliptical galaxies, observed firstly via the Hubble Sequence (Hubble, 1930), led to the theory that they share a formation mechanism — predominantly that of major mergers between galaxies redistributing stars from rotation-dominated orbits in a disk to dispersion-dominated orbits in a spheroid. This is evidenced in a number of works, from the theoretical (Toomre & Toomre, 1972), to the observational (Schweizer, 1990), and the numerical (Barnes, 1989, 1992).

In a cold dark matter ( $\Lambda$ CDM) universe (*e.g.*, Riess et al., 1998; Perlmutter et al., 1999), structure forms hierarchically (*e.g.*, White & Frenk, 1991), leading

to morphology being dynamic throughout a galaxy’s life. In other words, initial density perturbations in the early universe provided gravitational wells for the build up of matter to form stars and eventually galaxies. These galaxies then merge together over time, leading to merger-driven morphological transformation. From this, theory was developed that elliptical galaxies can regrow their disks, transitioning to disk galaxies with a bulge component as a remnant of the elliptical. [Steinmetz & Navarro \(2002\)](#) show via simulations that elliptical galaxies can rebuild a disk by slowly and smoothly accreting gas from their wider environment, leading to a disk that is younger than the bulge. Observationally, we do see that bulge components are more often than not redder than their corresponding disks (*e.g.*, [Moorthy & Holtzman, 2006](#); [Hudson et al., 2010](#); [Cocato et al., 2018](#); [Nedkova et al., 2024](#)), indicating that the stellar populations are much younger in disks.

It is not just that bulges and elliptical galaxies *can* form through mergers, rather they are an inevitable consequence of a major or minor merger (mass ratio greater than 1:4, or 1:10 respectively), as shown in simulation-based work by [Martig et al. \(2012\)](#). In other words, if a galaxy at  $z = 0$  has little-to-no bulge component, it has had a secular (*i.e.*, slow and calm) evolution since  $z \sim 2$ . We make use of this in [Chapter 4](#) in order to isolate AGN grown in the absence of major mergers. It is important to note that bulges can form through other mechanisms (such as bars causing material to flow inwards and build up a component that can look like a classical bulge, but has stellar properties more similar to those of disks and is referred to as a pseudobulge, or minor mergers with a mass ratio between 1:4 and 1:10 [Parry et al., 2009](#); [Bell et al., 2017](#); [Gargiulo et al., 2017](#)), so this is a one-sided correlation — all bulgeless galaxies at low redshift have been major-merger free since  $z \sim 2$ , but not all galaxies with a bulge have experienced a major merger.

In an elliptical galaxy, the orbits of the stars are dominated by random motion. However given that very few ellipticals are perfect spheres, there must still be a reasonable amount of systematic motion in the stellar orbits. The more ‘flattened’ an elliptical galaxy, the smaller the contribution of random motion ([Binney & Merrifield, 1998](#)). The rotational velocity gives the galaxy a preferred rotational

axis which, over time, flattens the galaxy further, increasing the contribution from rotation, and thus elliptical galaxies can relax into disks.

Given that bulges reside in disks, it can be assumed that their axis of rotation lines up with that of the disk, meaning that determining how various properties relate to the rotation can be done with a greater confidence of the rotation axis. However, observing bulge parameters is complicated by the starlight from the disk contaminating that from the bulge. By using the bulges in edge-on galaxies, this contamination can be reduced. Such observations have led to the conclusion that, in general, the rotational velocities are higher for bulges than for ellipticals (*e.g.*, [Kormendy & Illingworth, 1982](#); [Davies & Illingworth, 1983](#)). This is further solidified by numerical modelling by [Jarvis & Freeman \(1985\)](#), who show that describing a bulge as a rotationally flattened system can adequately reproduce the observed properties.

Pseudobulges have a more secular evolution than their classical counterparts (see [Kormendy & Kennicutt, 2004](#), for a review), with higher rotational velocities, younger stellar populations, and more diffuse surface-brightness profiles (*e.g.*, [Kormendy et al., 2006](#); [Drory & Fisher, 2007](#); [Fisher & Drory, 2008](#)). Although appearing similar to classical bulges on first inspection, they are structurally very different ([Gadotti, 2009](#)), and act as an intermediary between classical bulges and disks.

### 1.1.2.2 Galactic Disk

As mentioned briefly in Section [1.1.2.1](#), galactic disks are formed from the slow, smooth accretion of gas from the wider environment, which in turn is converted into stars in the disk. This means that, barring a sudden and violent event such as a major merger, the disk remains relatively undisturbed.

Gas is collisional, and so energy will be dissipated during collisions, cooling the gas down. Due to the conservation of angular momentum, this speeds up rotation, and a spheroid will flatten into a disk. As this gas in the disk forms stars, their collisionless nature means that they will stay in this flattened disk, unless a major event occurs ([Binney & Merrifield, 1998](#)) This means that the stars are all in approximately the same plane, with very little random motion.

This ongoing star-formation gives the disk a bluer appearance. With the advent of large surveys such as SDSS, an important bimodality was discovered between a blue cloud consisting primarily of disk galaxies, and a red sequence, consisting primarily of elliptical galaxies (Baldry et al., 2004, 2006; Willmer et al., 2006; Ball et al., 2008; Brammer et al., 2009). It is worth noting however that this dichotomy is not strong enough that colour can be used as a proxy for morphology (Smethurst et al., 2022); there also exists a blue, elliptical population and a red, spiral population (Schawinski et al., 2009; Bamford et al., 2009; Skibba et al., 2009; Bundy et al., 2010; Masters et al., 2010; Rowlands et al., 2012; Mahajan et al., 2020).

Late-type disk galaxies (*i.e.*, those with a minimal bulge component) have a poorly understood formation mechanism, due to the ‘angular momentum problem’ (Navarro & Benz, 1991; Navarro & White, 1994) leading to bulge-dominated disk galaxies. This is solved by preventing gas from forming stars too fast at high redshifts. Invoking supernovae feedback (the injection of matter and energy into the interstellar medium from exploding massive stars — see Section 1.2.3.2 for the AGN analogue) redistributes the matter with low angular momentum from the centre of the disk to the edges, resulting in more extended structures (*e.g.*, Sommer-Larsen et al., 2003; Governato et al., 2007), however this alone is not sufficient (Agertz et al., 2011), and should be combined with other methods of gaseous outflows enriching the intergalactic medium, such as AGN outflows (Oppenheimer & Davé, 2006; Di Matteo et al., 2005).

### 1.1.2.3 Large-Scale Galactic Bars

Kiloparsec-scale bars are elongated stellar structures that form in a significant proportion of disk galaxies in the local Universe. Masters et al. (2011) used SDSS to show that the bar fraction in disk galaxies at redshifts  $0.01 < z < 0.06$  is  $29.4 \pm 0.5\%$  when observed in the optical regime, although Barazza et al. (2008) report the bar fraction to be between 48% and 52% in the  $r$ -band, and this fraction could potentially be as high as 70% when infrared observations are made (Eskridge et al., 2000; Knapen et al., 2000). Usually the centre of the bar

aligns with the centre of the galaxy, but around 2% of bars in Milky Way-mass galaxies are offset from their host (Kruk et al., 2017).

Bars can form via two mechanisms in disks. The first is through disk instabilities. There are two different quantities used to measure the stability of the galactic disk. The Toomre stability parameter,  $Q$ , (Toomre, 1964) is defined as

$$Q = \frac{\kappa\sigma_r}{3.36G\Sigma} \quad (1.1)$$

where  $\kappa$  is the epicyclic frequency,  $\sigma_r$  is the velocity dispersion in the radial direction,  $G$  is the gravitational constant,  $\Sigma$  is the disk surface density. The disk is more unstable, and more likely to form a bar if it has a low radial velocity dispersion, a low velocity dispersion, and a high surface density. The ELN-criterion,  $\epsilon$ , (Efstathiou et al., 1982) is defined as

$$\epsilon = \frac{V_{\max}}{\sqrt{GM_d/R_d}} \quad (1.2)$$

where  $V_{\max}$  is the maximum rotational velocity,  $M_d$  is the total disk mass, and  $R_d$  is the scale length of the disk. The disk is more unstable and more likely to form a bar if it has a low rotational velocity, a high disk mass, and a small scale length.

If  $Q < 1$  or  $\epsilon < 1.1$  then the disk is unstable, and can form a bar. The Toomre parameter is more commonly used in simulations to induce bar formation (*e.g.*, Fanali et al., 2015; Seo et al., 2019).

The second is through tidal interactions and minor mergers (Noguchi, 1987; Barnes & Hernquist, 1991; Elmegreen et al., 1991; Skibba et al., 2012), which disturb the disk. The angle of approach between the two interacting galaxies can dictate whether a bar is formed — prograde interactions tend to form bars, but retrograde interactions do not (Lang et al., 2014; Lang, Holley-Bockelmann & Sinha, 2018; Lokas, 2018). However, this is not viable for low mass galaxies, since their smaller disks are easily tidally heated, which inhibits bar formation, whilst massive galaxies have disks that can maintain their stability and low dynamic temperatures throughout interactions (Méndez-Abreu et al., 2012).

Bars in disks can facilitate the transfer of angular momentum outwards from the centre, which traps stars in various bar orbits, making the bar longer (Sellwood, 1981; Athanassoula, 2003; Athanassoula et al., 2013). Due to the conservation of angular momentum, this then drives gas into the central regions of the galaxy (Athanassoula, 1992; Spinoso et al., 2017; George et al., 2019). This can create a burst of star formation in the centre of the galaxy, and a gas-poor region around the reach of the bar. The gas build-up at the centre, however, has been shown in simulations to potentially weaken the bar by disrupting the stellar bar orbits (*e.g.*, Athanassoula et al., 2013; Seo et al., 2019), although according to observations the gas build-up is rarely massive enough to facilitate this (Shen & Sellwood, 2004).

However, this gas build-up may be massive enough to trigger and fuel an AGN (Laine et al., 2002; Laurikainen et al., 2004; Oh et al., 2012; Galloway et al., 2015; Silva-Lima et al., 2022), although a number of studies find no such correlation (Cheung et al., 2015; Cisternas et al., 2015; Goulding et al., 2017). This is the focus of this thesis, and will be explored further in the subsequent chapters.

de Vaucouleurs (1959, 1963) divided spiral galaxies into three categories: unbarred, weakly barred and strongly barred, with strong bars being longer, brighter and more obvious than weak bars, which are fainter and smaller. But what makes a bar strong or weak is not easily defined. As stated in Athanassoula (2003), “Although the notion of bar strength is clear to everyone, and it is very often easy, when comparing two bars, to say which one is strongest, a precise definition is not trivial”. It remains to be seen if strong and weak bars are two, discrete categories (Buta et al., 2007; Buta, 2013), or whether bar strength is a continuous spectrum (Géron et al., 2021).

There are a number of ways in which bar strength is classified. Many studies use visual classification, such as Nair & Abraham (2010), who define the strength using the ratio of bar flux to the total galaxy flux, and Galaxy Zoo DECaLS (Walmsley et al., 2022), who use citizen science to obtain vote fractions (see Section 1.1.3.1). The volunteer-driven classifications tend to assign longer, brighter bars as strong, and shorter bars as weak, which reflects the icons they are shown in the project’s workflow. Another common method is to use ellipse fitting. Isophotes are measured, and their shape and orientation relative to each

other are analysed (Laine et al., 2002; Marinova & Jogee, 2007; Barazza et al., 2008). In this work, we predominantly use visual analysis, however Sheth et al. (2008) observed that the method used has no bearing on the results.

### 1.1.3 Classifying Morphology

#### 1.1.3.1 Galaxy Zoo and Galaxy Zoo 2

With the advent of large-scale surveys such as SDSS (Section 1.1.1.2), obtaining morphological classifications for all of the available galaxies became a mammoth task. The data were available, but there was no reasonable way to visually analyse them all. Asking a small handful of astronomers to classify hundreds of thousands of galaxies is simply not feasible, but the task can be divided amongst volunteers who, via an online platform, can classify galaxies.

This was done in a project known as Galaxy Zoo<sup>1</sup> (GZ1; Lintott et al., 2008), which soon spawned a mass citizen science platform known as the Zooniverse<sup>2</sup>. Thanks to the help of 100,000 volunteers, GZ1 was able to classify 1 million galaxies in the SDSS DR7 Legacy Catalogue (Abazajian et al., 2009) within six months of launch (Lintott et al., 2008, 2011).

GZ1 simply asked volunteers one multiple choice question, with six possible answers, each accompanied by an example icon:

**Choose the Galaxy Profile by clicking the buttons below.**

- **Spiral Galaxy**
  - Clockwise
  - Anti-clockwise
  - Edge on/Unclear
- **Elliptical Galaxy**
- **Star / Don't Know**

---

<sup>1</sup>Archived at <http://zoo1.galaxyzoo.org>.

<sup>2</sup>Available at <http://www.zooniverse.org>.

- **Merger**

The collected data were reduced in order to produce a catalogue, but we do not cover the reduction in detail given that GZ1 is not used directly in this thesis — see [Lintott et al. \(2008\)](#) for a full description of the release. However, the main steps involved removing obvious bogus classifications, such as those where the user had clearly used an automated mechanism, and then combining the three options for spiral galaxies into one classification of ‘Spiral Galaxy’.

The results from GZ1 were used to inform the processes of Galaxy Zoo 2<sup>1</sup> (GZ2; [Willett et al., 2013](#)), which asked users much more detailed questions about the morphology. This allowed more in depth analysis to be conducted.

GZ2 was first launched in 2009 following the success of GZ1, and consisted of a subset of galaxies identified in GZ1. Since GZ2 asked more questions about the large-scale structures within galaxies, a good resolution was required.

To facilitate this, a number of cuts were applied to the SDSS data. To be in the GZ2 sample, a galaxy must have: an  $r$ -band Petrosian half-light magnitude  $\text{petro\_m}_r \leq 17.0$ , a redshift (where spectroscopically known) of  $0.0005 \leq z \leq 0.25$ , and a radius containing 90% of the  $r$ -band Petrosian aperture flux of  $\text{petro\_R}_{90,r} > 3''$ . Sources with flags (as dictated by the SDSS pipeline) of SATURATED, BRIGHT, or BLENDED were also removed unless they were also flagged as NODEBLEND. This resulted in 245,609 galaxies in what was termed the ‘original’ sample. A smaller, ‘extra’ sample was later added to the web-interface, consisting of 28,174 galaxies with both CHILD and BLENDED flags.

A further sample was added to GZ2, that of the Stripe 82 sample. These were galaxies from the SGC (unlike DR7, which is limited to galaxies from the NGC), and were selected with the same criteria as above, although the  $r$ -band Petrosian magnitude was allowed to extend to 17.77 (due to the longer observation times of Stripe 82). However the primary sample for GZ2 includes only those Stripe 82 galaxies with the previous magnitude cut of 17.0. [Willett et al. \(2013\)](#) confirmed that introducing these as three separate samples (‘original’, ‘extra’ and ‘Stripe 82’) did not introduce any biases, and so could act as one cohesive dataset.

---

<sup>1</sup>Archived at <http://zoo2.galaxyzoo.org>.

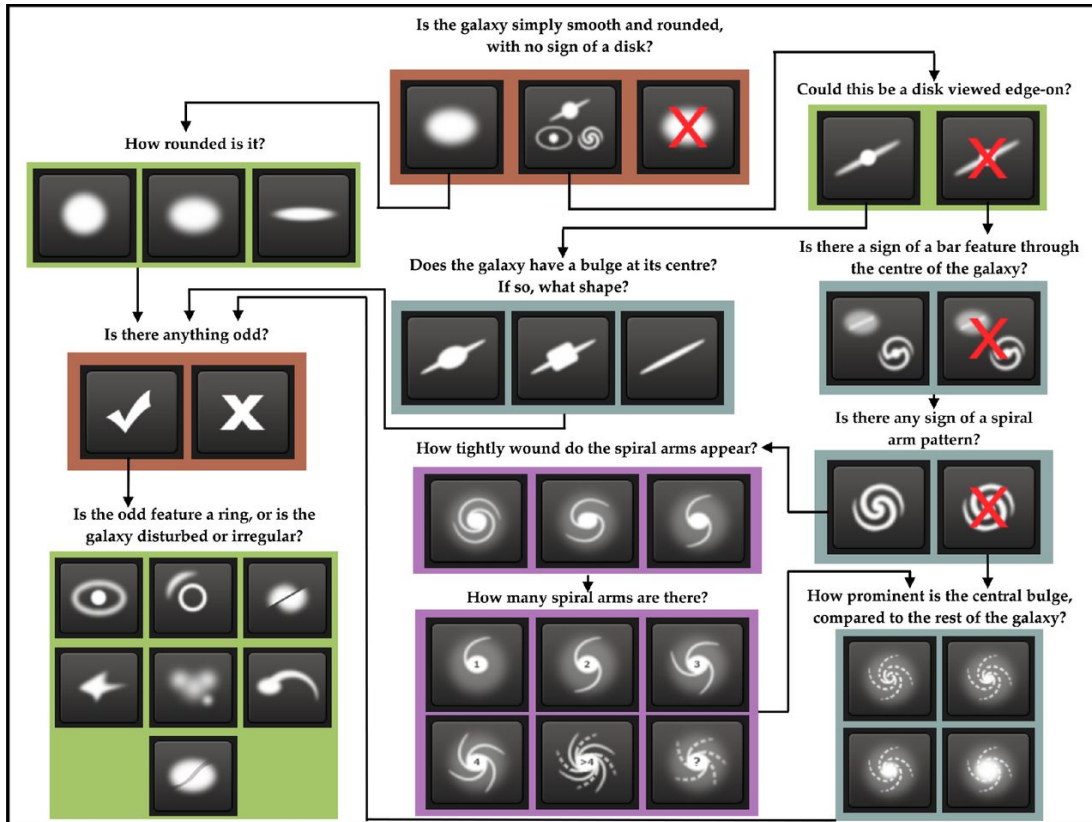


**Figure 1.3:** The question tree used in Galaxy Zoo 2 (Willett et al., 2013), and the icons used to demonstrate the question. Volunteers start at the top, centre question, and work their way through the flowchart. The colours represent the tier of question. Red boxes are questions answered for every galaxy, green boxes require one previous relevant answer, blue boxes two and purple boxes three. This setup shows clearly that not every volunteer answers every question about a galaxy.

On the completion of GZ2, 304,122 galaxies had been classified by 83,943 volunteers, making 16,340,298 classifications.

To obtain the more detailed results that those of GZ1, GZ2 asked volunteers a number of questions via the use of the question tree (Figure 1.3). This means that instead of just identifying whether a source is elliptical, spiral, merging or an artefact, a much more detailed classification was made, including details of whether or not a galaxy is barred, whether it contains a central bulge, how tightly wound the spiral arms are and how many, bulge prominence and shape, and how rounded a galaxy is, as well as identifying any ‘odd’ features.

Given the nature of galaxy structure, not every volunteer answered every question for a particular galaxy. For example, if a volunteer identified a featured, edge-on galaxy, they would not be asked about bar presence, since it is not possible to confidently determine bar presence in an edge-on galaxy. This means raw vote fractions cannot necessarily be used to determine how likely it is that a galaxy has a certain feature.

Consider a scenario where we have a particular galaxy where we require morphology identification. 25 people have classified this galaxy, but with various responses. 20 people have responded to Q1, “*Is the galaxy simply smooth and rounded, with no sign of a disk?*” with “*smooth and rounded*”, and five people have responded “*features or disk*”. These five people then all answer “*no*” to their Q2, “*Could this be a disk viewed edge-on?*”. Four out of these five volunteers answer “*yes*” to their Q3, “*Is there a sign of a bar feature through the centre of the galaxy?*”.

Of the 20 that answered “*smooth and rounded*”, 10 answer their Q2, “*How rounded is it?*” as “*completely round*”, 7 answer “*in between*”, and 3 answer “*cigar shaped*”.

This gives raw vote fractions of  $p_{\text{bar}} = 0.8$ ,  $p_{\text{completely-round}} = 0.5$ ,  $p_{\text{in-between}} = 0.35$ , and  $p_{\text{cigar-shaped}} = 0.15$ . By examining the raw fractions, we would come to the incorrect conclusion that the galaxy is barred. In reality, out of the 25 volunteers, the highest number of people voted for “*smooth and rounded; completely round*”, even though this option had a lower raw vote fraction than “*features or disk; bar*”. This means that the data reduction needed to take a number of factors into account that would not have needed consideration in GZ1.

Approximately 1% of galaxies had repeat classifications by the same user. These repeats were removed prior to analysis in order to prevent bias. This resulted in  $\lesssim 0.01\%$  of the sample having their classifications changed.

There were a number of unreliable classifiers, whose results essentially equated to random assigning of classifications. To reduce their influence, a weighting system was applied to factor in the consistency of each user. A high consistency value indicated that the vote agrees with the majority across all galaxies they voted on. Votes by users with a low mean consistency were then down-weighted. It is worth noting that votes by users with a high mean consistency were not

up-weighted, leading to the vast majority ( $> 95\%$ ) of users being treated equally and having no weighting applied<sup>1</sup>.

Once the consistency had been calculated for each user, the new weights were used to recalculate the vote fractions, and this whole process was repeated again to ensure convergence.

The weighted vote fractions still suffer from bias that is dependent on redshift. Sources at higher redshifts are dimmer and smaller, meaning identifying finer features such as bars and bulges comes with higher uncertainty. This source of bias is not unique to GZ2, but is inherent to all astrophysical imaging classifications, not just visual. It will persist in classifications done via automated systems or small groups of experts, even if alternative schemes are used, such as Sérsic indices (Sérsic, 1968), or CAS (Concentration, Asymmetry, Smoothness; Conselice, 2003) metrics. Nevertheless, it must still be accounted for. GZ2 use the same process that was described in Bamford et al. (2009) and applied to GZ1.

This bias with redshift is partially due to the apparent magnitude limit of  $\text{petro-}m_r \leq 17.0$ , which means galaxies must have a brighter absolute magnitude at the far end of the redshift cut-off in order to make it into the sample. This then implies that these galaxies are more likely to be giant ellipticals, since these are brighter and have a more concentrated light profile than spirals (Kauffmann et al., 2003b). To get around this, Bamford et al. (2009) binned the data with respect to redshift,  $z$ , absolute  $r$ -band Petrosian magnitude,  $M_r$ , and physical Petrosian half-light radius,  $R_{50}$ . In the lowest redshift bin, they find the elliptical-to-spiral ratio for each  $(M_r, R_{50})$ , and use this as a baseline by which to normalise the remaining redshift bins.

In order to expand this method to GZ2, this method was done for every question. This results in the weighted, debiased vote fractions. For brevity's sake, when we refer to the GZ2 vote fractions throughout, we are referring to the weighted, debiased vote fractions.

---

<sup>1</sup>The high numbers of volunteers who participated fully in the classifications and without making bogus classifications has been used to conduct studies on motivations for volunteering. They get no reward for their time, and no penalty for not participating, or for making random selections, and yet the majority of volunteers undertake the exercise properly (Jordan Raddick et al., 2013).

Willett et al. (2013) noted that they did not debias for angular separation, in order that those who want to make use of GZ2 data can perform analysis on close pairs. However, they also note that from Casteels et al. (2013), this bias only substantially affects merger classifications, and can be ignored elsewhere.

There is generally good agreement in classifications between GZ2 and other classification catalogues, namely GZ1, the catalogue of Nair & Abraham (2010), EFIGI (Baillard et al., 2011), and the catalogue of Huertas-Company et al. (2011). GZ2 is less able to recover weakly barred galaxies (see Section 1.1.3.2) and inner rings, likely due to the structure of the question tree. Future iterations of Galaxy Zoo worked to address this, and we particularly make use of the distinction between strong and weak bars in Chapter 4. The bulge dominance parameter calculated from GZ2 (Masters et al., 2019) is in strong agreement with the Hubble T-type used in both Nair & Abraham (2010) and EFIGI, although when compared to Huertas-Company et al. (2011), the recovery of lenticular galaxies (S0 on the Hubble Sequence) requires more work.

Since the release of GZ2, there have been a number of other iterations of Galaxy Zoo, using different datasets with the same basic format. These include GZ:Hubble (Willett et al., 2017), GZ:CANDELS (Simmons et al., 2017a) and GZ:DECaLS (Walmsley et al., 2022). GZ:Hubble and GZ:CANDELS asked additional questions regarding clumpiness of the galaxy, and GZ:DECaLS asked additional questions about bar strength. In addition, the volunteer classifications of GZ:DECaLS are used to train deep learning models to perform classifications, discussed further below.

### 1.1.3.2 GZ DESI

The most recent iteration of Galaxy Zoo (at the time of writing) uses DESI-LS (GZD<sup>1</sup>; Walmsley et al., 2023a), however this does not use the same citizen science approach as previous versions. The quantity of data in DESI-LS makes even the speed of volunteer classification insufficient — at current classification rates this would take 200 years. Instead, a deep learning model (*Zoobot*) was trained on GZ: DECaLS data (Walmsley et al., 2022), as well as new volunteer

<sup>1</sup>Available at <https://zenodo.org/records/8360385>.

votes from DESI-LS DR8 to identify the morphology of DESI-LS in a way that mimics the volunteer classifications.

A sample was collated from DESI-LS plus DES (see Section 1.1.1.3) by selecting extended sources with an  $r$ -band magnitude  $m_r > 19.0$ , a surface brightness of  $\mu > 18$  mag arcsec<sup>-2</sup>, and images with at least 80% flux completeness in each band when images are downloaded from the DESI-LS cutout service, resulting in 8,689,370 galaxies.

Volunteer classifications are used to train the models to make morphology predictions on DESI-LS, primarily from the 7.5 million labels in GZ:DECaLS. A smaller set of volunteer classifications arise from DECaLS images released in DESI-LS, which were not part of GZ:DECaLS. These galaxies are typically at a higher redshift, smaller angular size, and fainter magnitude than those in GZ:DECaLS, and thus the models can be extended to these more challenging regimes.

The models output estimates of volunteer classifications for each question in the question tree, which is the same as that used for GZ:DECaLS (Figure 1.4). This is similar to that of GZ2, but asks additional questions about bar strength and level of disturbance in a system. The predictions of the models agree with the volunteer vote fractions to within 5–10%. Note that the primary GZD release only contains the automated votes, but Walmsley et al. (2023a) do also release the volunteer classifications in a separate table.

The authors highlight that since Walmsley et al. (2023a), there have been further data releases from DESI-LS, namely DR9 and DR10, and that their models could be seamlessly applied to these updated catalogues. The speed of classifications by GZ:DESI was significantly faster than downloading the images from the DESI-LS cutout service — hours versus weeks, and thus in future large scale surveys, such as those to be conducted by *Euclid* and the Vera C. Rubin Observatory, the limiting factor will be accessing the data rather than performing the classifications. However, great strides are currently being made in remote data access software (*e.g.*, O’Ryan et al., 2023).

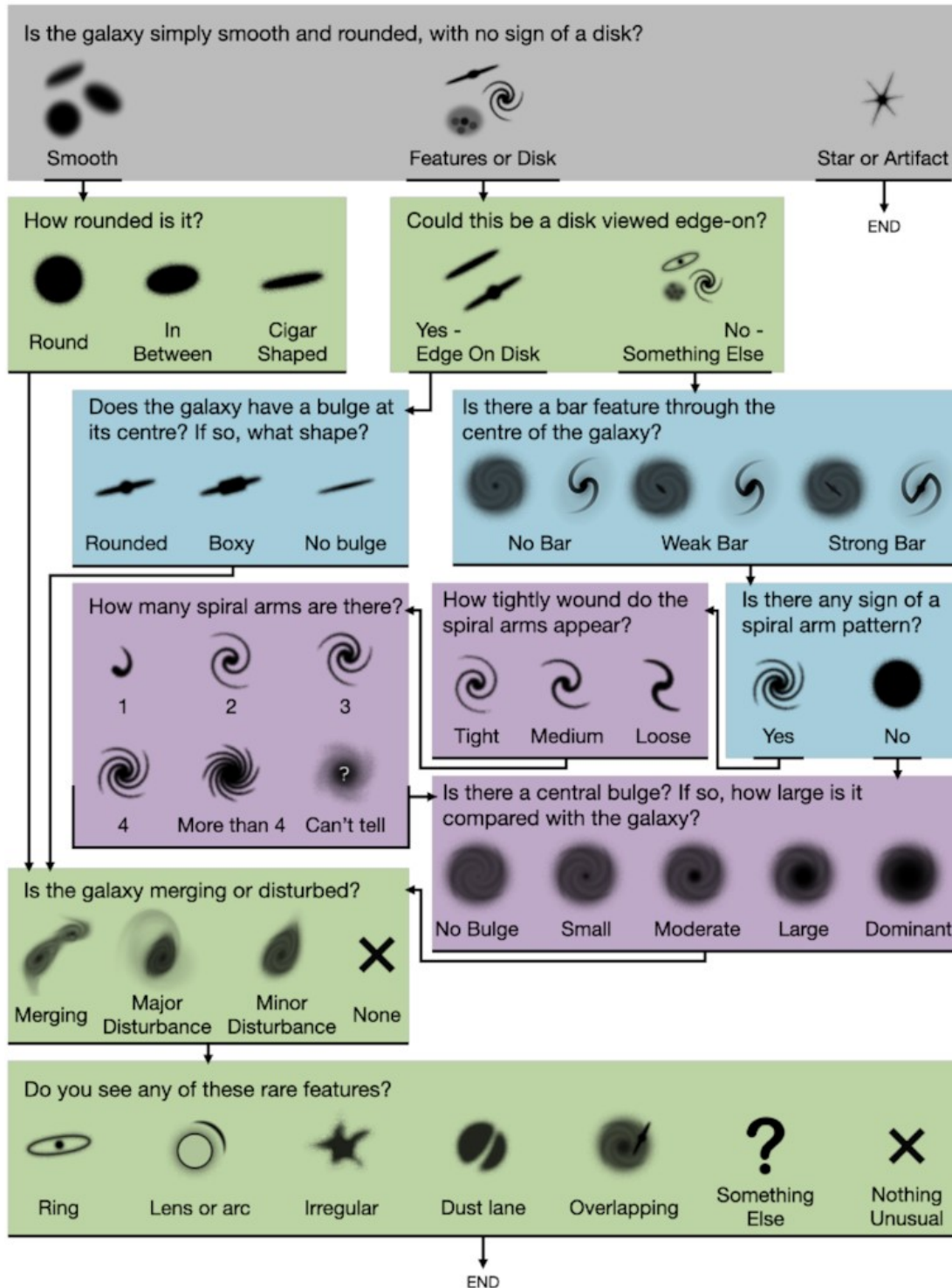


**Figure 1.4:** The question tree used in Galaxy Zoo DECaLS (Walmsley et al., 2022). Compared to the question tree used in GZ2 (Figure 1.3), this iteration asks about the strength of the bar rather than just the presence, and has five categories for bulge strength instead of four. Grey boxes represent questions asked for all galaxies, green boxes requires one previous answer, blue requires two and purple requires three.

### 1.1.3.3 AGN Contamination

It is worth noting that the presence of a bright AGN can influence the morphology determination. Since the AGN can appear as a bright, central point source, this can mimic a small bulge component, particularly when the images that the classification are based on has a large PSF (see Section 3.2.3.3 for one way that this is dealt with when conducting scientific analysis). This influence is present in both parametric fitting (*e.g.*, Simmons & Urry, 2008) and visual classification (*e.g.*, Simmons et al., 2013).

Given that machine-learning algorithms are trained on classifications that have already been made, such as *Zoobot* being trained on volunteer votes from GZ: DECaLS, any biases that are present in the training data will also be present in the final classifications of the morphologies.

## 1.2 Active Galactic Nuclei

### 1.2.1 AGN structure

AGN are observed in a number of different classes, notably Type 1 and Type 2. Whilst both of these are highly luminous point-like sources in the centre of galaxies, they have different spectra. Type 1 AGN are characterised by the presence of both broad and narrow emission lines, whereas in Type 2 AGN, only narrow emission lines are seen. The theory of AGN Unification (*e.g.*, Antonucci, 1993; Urry & Padovani, 1995) provides one possible albeit incomplete, explanation for this difference in broad emission line presence. Due to the structure of AGN, their observed properties are dependent on the viewing angle, in particular whether the line-of-sight to the black hole passes through a sufficient quantity of dust to block the broad emission lines.

The current, broadly accepted structure of an AGN is shown in Figure 1.5a, and depicts a SMBH surrounded by an accretion disk, which is further surrounded by an obscuring dusty torus. The dichotomy between Type 1 and Type 2 exists due to whether or not we are viewing the AGN through the torus. Type 1 AGN are unobscured by the torus, meaning that the broad-line region (BLR) can be

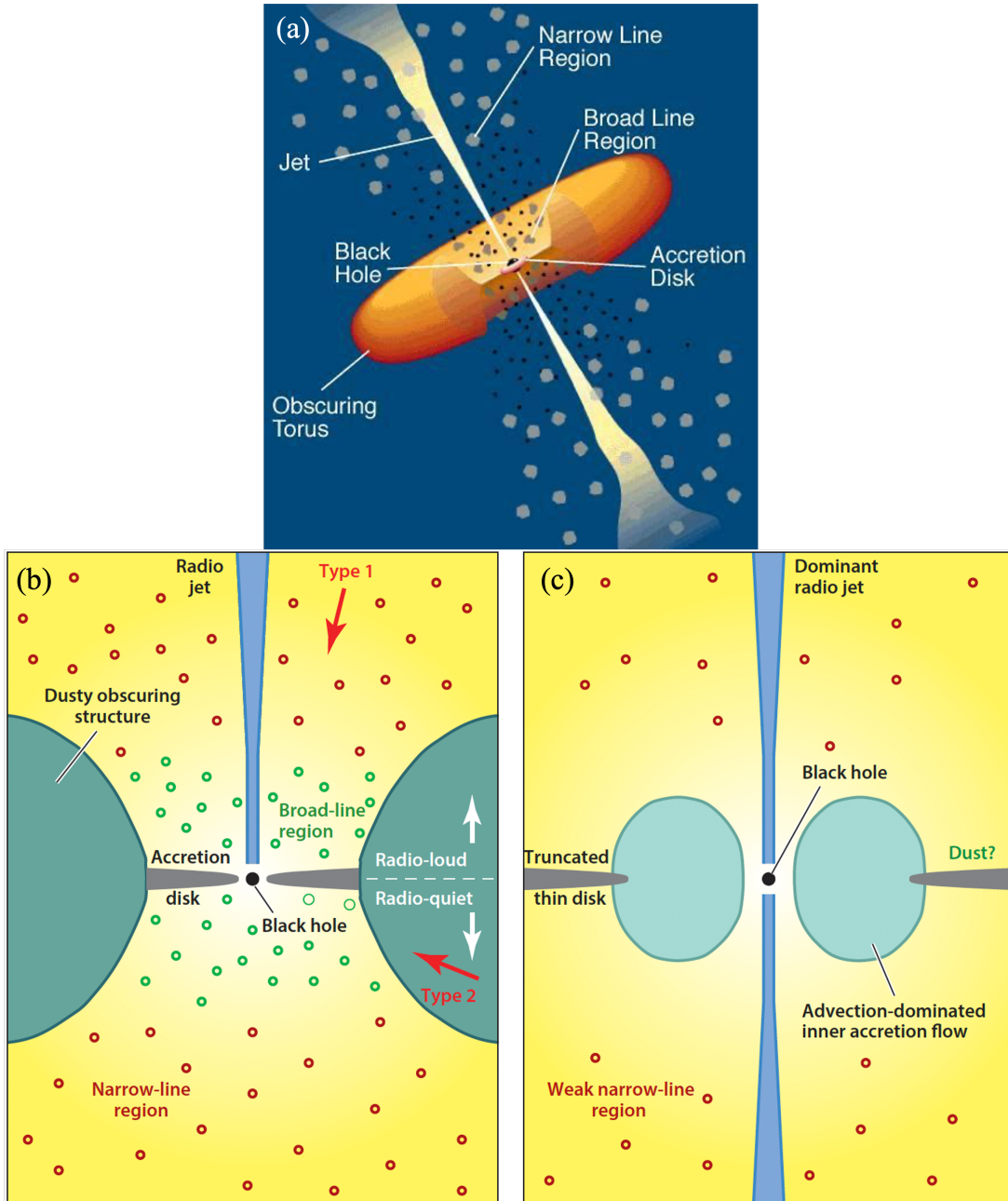


**Figure 1.5:** Physical structures comprising an active galactic nucleus. Panel (a) taken from [Urry & Padovani \(1995\)](#), Panels (b), (c) taken from [Heckman & Best \(2014\)](#). Panel (a) shows the structure of an AGN under the theory of unification, which suggests that all the observed differences between AGN categories are purely down the viewing angle. Panels (b), (c) contain the same key elements, but with different relative strengths. Panel (b) shows a radiative-mode AGN (with a jet in the upper half, and without in the lower), and Panel (c) shows a jet-mode AGN.

observed. Type 2 AGN are viewed through the torus, meaning that much of the light emitted is obscured by the dust, including the entire BLR. Given that only the narrow-line region (NLR) is visible in Type 2, we see only narrow emission lines in their spectra. If the line-of-sight is directly down the radio jet, the AGN becomes known as a blazar, and is characterised by a radio-loud spectrum with very few emission or absorption features.

Heckman & Best (2014) take this a step further, and propose that there are two intrinsic types of AGN — radiative-mode, and jet-mode — also shown in Figure 1.5b,c. Radiative-mode AGN emit most of their energy budget in the form of electromagnetic (EM) radiation. The relatively low-energy jets of these AGN can either be present or not, resulting in a radio-loud and a radio-quiet population, depending on whether we are observing AGN with or without a jet. Conversely, jet-mode AGN emit less EM radiation, instead inputting more of their energy budget as kinetic energy in more prominent jets that are double sided. These collimated jets bulk transport kinetic energy (*i.e.*, material). There is much debate in the literature about whether radiative- and jet-mode AGN are distinct objects, or different phases through which an AGN may evolve (see Heckman & Best, 2014, for a review).

Low-Ionisation Nuclear Emission Line Regions (LINERs) were first identified as a separate class by Heckman (1980). Their optical spectra are dominated by (as the name suggests) low-ionisation species such as [OI] and [OII]. They have a much lower luminosity than Type 1 or 2 AGN, but with similar linewidths as those seen from NLRs. LINERs are not well understood — it is likely that the emission in the lowest luminosity LINERs is driven by star formation, and in the highest luminosity LINERs, by low-luminosity AGN (Heckman & Best, 2014; Coldwell et al., 2018, private communication T. Heckman, P. Best).

### 1.2.2 AGN Identification

There are a number of methods through which AGN can be identified, using different parts of the EM spectrum, notably radio, X-ray, optical and infra-red (IR). This is due to their intense luminosity throughout the spectrum — a characteristic seen in few other celestial objects. Here, we discuss the primary method

used in this thesis to identify AGN (optical), and briefly touch on X-ray and IR methods, since these are used to compile AGN catalogues of which we also make use.

### 1.2.2.1 BPT Diagrams

Baldwin, Phillips & Terlevich (1981) noted that the activity types of extragalactic objects could be classified using optical emission line ratios. Their original work separated emission-line objects into normal HII regions, planetary nebulae, objects photoionised by a power-law continuum, and objects excited by shock-wave heating, using what has become known as a BPT diagram or in some cases, an emission-line diagram. Osterbrock & De Robertis (1985) and Veilleux & Osterbrock (1987) expanded this work to Seyfert galaxies.

In its modern form, the BPT diagram utilises line ratios of  $[\text{OIII}]/\text{H}\beta$ ,  $[\text{NII}]/\text{H}\alpha$ ,  $[\text{SII}]/\text{H}\alpha$ , and  $[\text{OI}]/\text{H}\alpha$ , with seven empirically and semi-analytically derived relationships, shown in Equations 1.3 to 1.9, to classify “AGN”, “star-forming galaxies” (SFGs), “LINERs”, and “composite galaxies”. These lines can separate out the different activity sources in galaxies due to AGN having a harder ionisation field (*i.e.*, emitted photons have a higher energy), and a higher temperature. This source of high energy and temperature is due to the accretion disk surrounding the SMBH, radiation from which heats up the diffuse gas in the narrow line region, resulting in the emission lines utilised in the BPT-diagrams. In star-forming galaxies, the energy source is due to young O and B stars, which photoionise the surrounding HII region, although they do so at a much softer ionisation field and cooler temperature than AGN, resulting in the difference in line ratios, making this method suitable for classification. The version used throughout this work is illustrated in Figure 1.6. Since line ratios are used, rather than absolute fluxes, this accounts for galaxies which have an overall lower luminosity (whether intrinsic or due to environmental reasons).

In order to be able to classify the activity of a source into one of the above types, there must first be enough emission to do so. To facilitate this, the measured signal-to-noise of at least some of the emission lines in Figure 1.6a ( $\text{H}\alpha$ ,  $\text{H}\beta$ ,  $[\text{OIII}]$  and  $[\text{NII}]$ ) must fall above a certain threshold, most commonly  $\text{S/N} \geq 3$ .

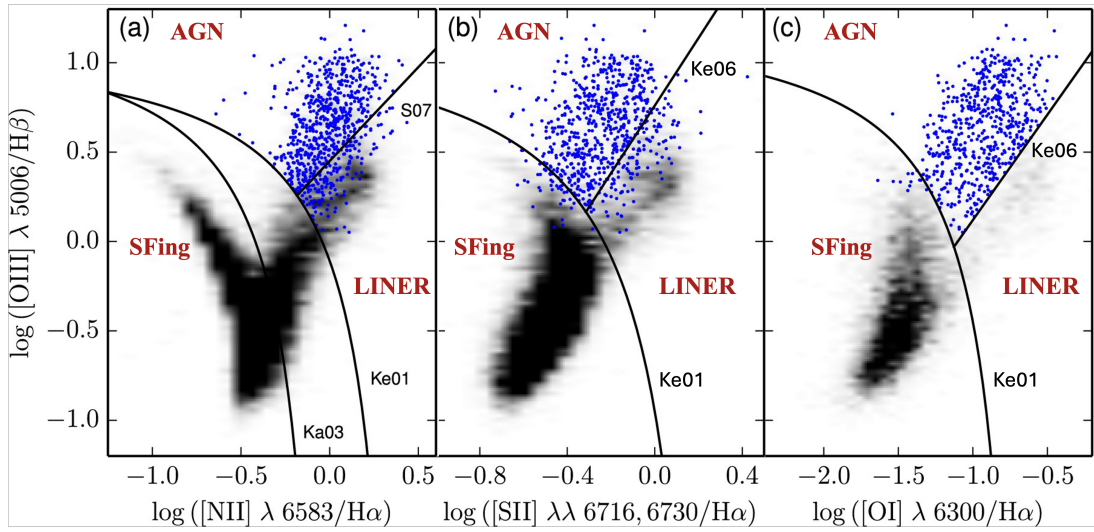


**Figure 1.6:** Example BPT diagrams, taken from [Galloway et al. \(2015\)](#). Panel (a) uses [NII], and is the preferred method to distinguish between star formation, and AGN/LINER as the main engine, or a mix of both. Panel (c) uses [OI], and once a source has been classified as either an AGN or a LINER, this is the panel used to separate these two. Panel (b) uses [SII] is used to distinguish between AGN and LINERs if there is insufficient [OI]. If there is insufficient [OI] and [SII] then Panel (a) is used to make this distinction. The galaxies classed as AGN are shown in these plots as blue circles, and the black region represents non-AGN galaxies, provided they have a signal-to-noise ratio of  $S/N \geq 3$  in [OIII],  $\text{H}\beta$ , [NII] and  $\text{H}\alpha$ . If this signal-to-noise requirement is not met, the location of the galaxy is not plotted and it is classed as undetermined.

If the source does not meet this initial requirement, it is classified as “Undetermined”. However, if this requirement *is* satisfied, then Figure 1.6a is used to classify it as an SFG if it falls below the Ka03 line (Kauffmann et al., 2003c), found through an empirical fit to be

$$\log\left(\frac{[\text{OIII}]}{\text{H}\beta}\right) = \frac{0.61}{\log\left(\frac{[\text{NII}]}{\text{H}\alpha}\right) - 0.05} + 1.30 \quad (1.3)$$

If it falls between the Ka03 line and the Ke01 line (Kewley et al., 2001), defined via semi-analytical models as

$$\log\left(\frac{[\text{OIII}]}{\text{H}\beta}\right) = \frac{0.61}{\log\left(\frac{[\text{NII}]}{\text{H}\alpha}\right) - 0.47} + 1.19 \quad (1.4)$$

then it is considered composite. If it falls above the Ke01 line, it is considered to be either an AGN or a LINER. Both of these lines are crucial if we want to select pure samples of SFGs or AGN.

Either [NII], [SII] or [OI] can be used to distinguish between an AGN and a LINER. [OI] is the most reliable emission line (Kewley et al., 2006), however as with the previous lines, it must have a signal-to-noise ratio of  $S/N \geq 3$ . If this is the case, Figure 1.6c is used to classify any source falling above the Ke01 line (Kewley et al., 2001), found through an empirical fit to be

$$\log\left(\frac{[\text{OIII}]}{\text{H}\beta}\right) = \frac{0.73}{\log\left(\frac{[\text{OI}]}{\text{H}\alpha}\right) - 0.59} + 1.33 \quad (1.5)$$

and below the Ke06 line (Kewley et al., 2006), also found empirically to be

$$\log\left(\frac{[\text{OIII}]}{\text{H}\beta}\right) = 1.18 \log\left(\frac{[\text{OI}]}{\text{H}\alpha}\right) + 1.30 \quad (1.6)$$

as a LINER, and any source falling above the Ke01 line and the Ke06 line as an AGN.

Where the signal-to-noise in [OI] is too low, [SII] is the next most reliable emission line. Thus, if  $S/N_{[\text{SII}]} \geq 3$  Figure 1.6b can be used and the previous

steps are repeated. Any source falling above the Ke01 line (Kewley et al., 2001), found empirically to be

$$\log\left(\frac{[\text{OIII}]}{\text{H}\beta}\right) = \frac{0.72}{\log\left(\frac{[\text{SII}]}{\text{H}\alpha}\right) - 0.32} + 1.30 \quad (1.7)$$

and below the Ke06 line (Kewley et al., 2006), found empirically to be

$$\log\left(\frac{[\text{OIII}]}{\text{H}\beta}\right) = 1.89 \log\left(\frac{[\text{SII}]}{\text{H}\alpha}\right) + 0.76 \quad (1.8)$$

is classified as a LINER, and any source falling above these Ke01 and Ke06 lines as an AGN.

If  $S/N_{[\text{SII}]}$  and  $S/N_{[\text{OI}]}$  are both insufficient, the S07 line (Schawinski et al., 2007) is used, found empirically to be

$$\log\left(\frac{[\text{OIII}]}{\text{H}\beta}\right) = 1.05 \log\left(\frac{[\text{NII}]}{\text{H}\alpha}\right) + 0.45 \quad (1.9)$$

All of the sources left will have  $S/N_{[\text{NII}]} \geq 3$ , else they would have been designated “Undetermined”. Any source above this line and the Ke01 line (Kewley et al., 2001), is classified as an AGN. Any source above this Ke01 line, but below the S07 line is classified as a LINER.

Dealing with a mix of detected and undetected lines is discussed in Chapter 4.

Whilst this method has high levels of reliability, using BPT diagrams to select samples of AGN can miss weaker AGN, or those in highly star-forming galaxies, where the star formation can overpower the emission lines from the AGN. If the AGN has a low accretion rate, then the accretion disk is less efficient at heating up the narrow-line region, meaning that the galaxy may not be classified as an AGN-host (*e.g.*, Trump et al., 2015; Jones et al., 2016; Agostino & Salim, 2019).

### 1.2.2.2 Infrared and X-Ray Identification

The dusty torus structure (shown in Figure 1.5) means that there is a high level of mid-IR emission in AGN, however this emission can also come from SFGs. This means that IR-detected AGN are biased against AGN hosts with high levels

of star formation (Brusa et al., 2009). The colour–colour criteria developed by Stern et al. (2005) relies on a source being detected in the four Infrared Array Camera (IRAC) bands, an instrument on the *Spitzer* telescope. These bands are  $3.6\ \mu\text{m}$ ,  $4.5\ \mu\text{m}$ ,  $5.8\ \mu\text{m}$  and  $8.0\ \mu\text{m}$ , and are combined to empirically define a selection region to identify IR-selected AGN.

$$\begin{aligned} ([5.8] - [8.0]) > 0.6 \wedge ([3.6] - [4.5]) > 0.2 \times ([5.8] - [8.0]) + 0.18 \\ \wedge ([3.6] - [4.5]) > 2.5 \times ([5.8] - [8.0]) - 3.5 \end{aligned} \quad (1.10)$$

Using X-rays to detect AGN produces fewer false positives than IR methods, since the AGN luminosity in the X-ray clearly outshines the light from stars, although X-rays are highly attenuated by dense gas, such as that found around obscured AGN. This means the selection criteria for X-ray AGN is simply based on a luminosity cut from  $2 - 10\ \text{keV}$  (Mullaney et al., 2015)

$$L_{2-10\text{keV}} > 10^{42}\ \text{ergs s}^{-1} \quad (1.11)$$

This means that very deep X-ray surveys are needed to detect the most obscured AGN. However, in order to study the host galaxy, follow up data is required in other regimes of the EM spectrum, such as optical or infrared.

### 1.2.2.3 Radio Identification

Radio observations allowed for the discovery of “quasi-stellar radio sources” (now known as quasars) by Schmidt (1963), and subsequent work by Sandage (1965) showed a large population of quasars at high redshifts. These quasars were the highly luminous counterparts to the active nuclei found in more local galaxies (Seyfert, 1943). More recently, radio surveys have become crucial to find jet-mode (radio-loud) AGN, since these emit most of their energy in the form of radio jets (see Section 1.2.1). However, radiative-mode AGN (radio-quiet) can still be detected, since the dusty torus is optically thin to radio emission.

The detection of radio AGN, similarly to that of X-ray AGN, relies on detecting more emission than can be explained by star-formation alone. For example,

Deller & Middelberg (2014) collate their mJy Imaging VLBA Exploration at 20 cm survey (mJIVE-20), by exploiting the fact that very long baseline interferometry techniques' high resolution require a source to have a brightness temperature of  $> 10^6$  K, which is not achievable via star-formation, to ensure that their sources are AGN, with a very low contamination rate — 1.6% of detections.

### 1.2.3 BH–Galaxy Co-evolution

Galaxies and SMBH operate on vastly different scales. The black hole mass is a tiny fraction (generally around 0.1%) of the stellar mass of the galaxy, and the radii are even more disparate. For example, if we have a SMBH with a mass of  $10^8 M_{\odot}$ , then the Schwarzschild radius (Schwarzschild, 1916) would be  $r_s = 2GM_{\text{BH}}/c^2 \approx 2 \text{ AU}$ , where  $G = 6.67 \times 10^{-11} \text{ N m}^2 \text{ kg}^{-2}$  is the gravitational constant,  $M_{\text{BH}}$  is the SMBH mass, and  $c$  is the speed of light. Galaxies on the other hand, are tens, or even hundreds of thousands of light years in radius (*e.g.*, Goodwin et al., 1998). That there are galaxy properties which correlate with SMBH properties is a surprising result, and we delve further into these correlations below.

Broad evidence of co-evolution can be seen in Figure 15 of Madau & Dickinson (2014) (shown here in Figure 1.7), which summarises the cosmic BH accretion history and the cosmic star formation history from a number of other works to demonstrate that these two quantities trace each other, both peaking around  $z \sim 2$ .

A number of relationships exist that demonstrate co-evolution between the SMBH and the wider properties of the galaxy (see Kormendy & Ho, 2013, for a review). Many of these rely on co-evolution with specifically the galactic bulge (*e.g.*,  $M_{\text{BH}} - \sigma$ ,  $M_{\text{BH}} - L_{k,\text{bulge}}$ , where  $M_{\text{BH}}$  is the BH mass,  $\sigma$  is the velocity dispersion of the bulge, and  $L_{k,\text{bulge}}$  is the bulge luminosity in the  $k$ -band), and thus it was previously assumed that only mergers could trigger and fuel luminous AGN, since a bulge is an inevitable consequence of a merger. Thus if properties of the SMBH correlate exclusively with properties of the bulge and not the disk, it follows that mergers likely trigger the AGN as they form the bulge. (see Section 1.1.2.1).

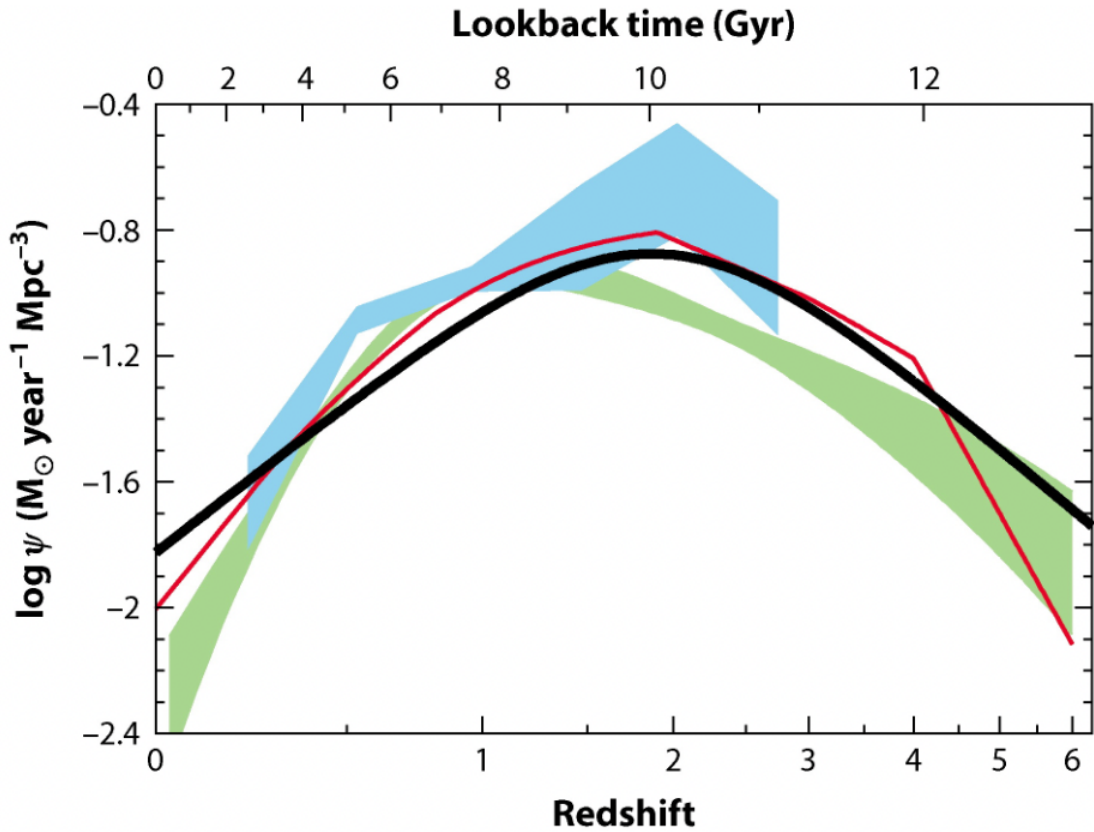


**Figure 1.7:** Taken from [Madau & Dickinson \(2014\)](#). The cosmic star formation history (SFH) is shown as the thick black line. The thin red line ([Shankar et al., 2009](#)) and the green shaded region ([Aird et al., 2010](#)) show the X-ray derived black hole accretion history (BHAR), and the blue shaded region ([Delvecchio et al., 2014](#)) shows the infrared BHAR. The BHAR curves have been scaled up by 3,300 for ease of comparison with SFH. Both accretion histories peak around  $z \sim 2$ , and fall off to either side in a very similar manner. This tracing indicates that the two are linked via some mechanism.

Yet in more recent years, populations of AGN have been found in bulgeless disk galaxies by a number of studies (*e.g.*, [Schawinski et al., 2011, 2012](#); [Simmons et al., 2012, 2013](#)). In these systems, we also see evidence of co-evolution, notably via that of the  $M_{\text{BH}} - M_*$  relationship ([Cisternas et al., 2011](#)), where  $M_*$  is the stellar mass of the galaxy. Given that a bulge is an inevitable consequence of a major or minor merger, bulgeless galaxies have been major-merger-free since around  $z \sim 2$  ([Martig et al., 2012](#)), corresponding to a lookback time of  $\sim 10^{10}$  yr. Given that AGN lifetimes are significantly shorter than this (SMBH may be in the AGN phase for  $\sim 10^5$  yr; [Schawinski et al., 2015](#)), if we observe an AGN at low redshifts in a bulgeless galaxy, we know it has not been triggered by a merger. [Martin et al. \(2018\)](#) showed, using the Horizon-AGN simulation, that as much as 65% of BH growth has occurred in the absence of major mergers since  $z \approx 3$ , encompassing the peak of both BH accretion and star formation. Subsequently, [McAlpine et al. \(2020\)](#) used the Evolution and Assembly of GaLaxies and their Environments (EAGLE) simulation to demonstrate that the contribution of non-merger processes to BH growth could be as high as 85%. The question then is: what does trigger the AGN? And what facilitates co-evolution?

### 1.2.3.1 Switch On and Fuelling

Mergers can, and do, trigger the switch on of AGN — some sub-populations of AGN such as radio-loud, red quasars are predominantly hosted in mergers ([Urrutia et al., 2008](#); [Glikman et al., 2015](#)). This is because during a merger, angular momentum is transferred from the rotation-supported disks to the dispersion-supported bulge. This means that material can be transported inwards to the SMBH, allowing for the rapid accretion to occur, triggering an AGN. As the merger is occurring, this transfer of material can also trigger bursts of star formation. Thus both the galaxy and the SMBH are affected, allowing co-evolution to be observed.

This is only part of the whole picture. As mentioned in Section 1.2.3, not all AGN are observed in galaxies that have been through mergers — there must be some non-merger driven process. This process must transfer material to the accretion disk of the SMBH, a radius of  $\approx 10$  pc. If we look at the average

accretion rates of AGN and their outflows (see Section 1.2.3.2), we then have a minimum amount of mass that must be transferred to this central  $\approx 10$  pc. For example, Smethurst et al. (2019) calculated for a subsample of 10 AGN (taken from the sample collated in Simmons et al., 2017b) a mean outflow rate of  $0.95 \pm 0.14 M_{\odot} \text{ yr}^{-1}$ , and using the Simmons et al. (2017b) accretion rates, a mean accretion rate of  $0.054 \pm 0.039 M_{\odot} \text{ yr}^{-1}$ . This means that this sample of systems would have to have an mean inflow rate of  $1.01 \pm 0.14 M_{\odot} \text{ yr}^{-1}$ , provided by the host galaxy.

A number of different secular processes have been shown via simulations to be capable of providing this level of inflow: large-scale galactic bars (Sakamoto, 1996; Maciejewski et al., 2002; Regan & Teuben, 2004; Lin et al., 2013), spiral arms (Maciejewski, 2004; Davies et al., 2009; Schnorr-Müller et al., 2014; Slater et al., 2019) and smooth accretion of cold gas (Kereš et al., 2005; Sancisi et al., 2008).

Yet these features have to have relatively long lifetimes in order to fuel an AGN over an extended period of time. AGN have been shown to be active for  $\sim 10^5$  yr (Schawinski et al., 2015), with outflows lasting from  $\sim 10^5$  yr to  $\sim 10^9$  yr (Smethurst et al., 2019, 2021), so the inflow mechanism must have a comparable lifetime. Bars, spiral arms, and smooth accretion have all been shown to be long-lived processes, relative to AGN lifetimes. Thus, in theory, any of them (or a combination thereof) could be responsible for AGN switch on and fuelling.

### 1.2.3.2 Feedback

Current theories of a  $\Lambda$ CDM Universe generally hold up well to observations, yet they predict a higher number of massive galaxies than we observe (*e.g.*, Read & Trentham, 2005). AGN feedback can affect the star formation in a galaxy, causing quenching and ceasing galaxy growth (see Fabian, 2012, for a review). However, it has also been theorised to be positive, enhancing galaxy growth (*e.g.*, Ishibashi & Fabian, 2012; Silk, 2013). This positive feedback could occur if, as the outflow is moving through the interstellar medium, it compresses gas at the front of the outflow, triggering bursts of star formation due to the increased density.

The negative feedback is thought to occur in two different modes. “Quasar”, or radiative, mode occurs when the black hole is accreting at or near the Eddington Limit. The accreting black hole drives powerful outflows, as evidenced by the blueshifted emission and absorption lines in their spectra. “Kinetic”, or jet, mode is also known as maintenance mode, and is more likely to occur in more massive galaxies where the black hole has a low Eddington ratio (Fabian, 2012). The powerful radio jets originating from the AGN can transport copious amounts of heated material. Work using Horizon-AGN and SIMBA has indicated that the feedback mode can be dependent on the fuelling mechanism. Merger-free growth leads to black holes having higher spin, since the constant angular momentum vector of the accreting material causes the black hole to spin up, as opposed to the chaotic motion of merger-driven accretion leading to spinning down of the SMBH (Berti & Volonteri, 2008; Dotti et al., 2013; Dubois et al., 2014; Bustamante & Springel, 2019; Beckmann et al., 2024). This means that merger-free growth is more likely to result in jet mode feedback due to the spin of the black hole being higher and more aligned with the host galaxy (Davé et al., 2019; Beckmann et al., 2024; Smethurst et al., 2024). However given that SMBH spins are challenging to observe directly, requiring high resolution X-ray observations, this has not yet been observed on a large scale.

We have introduced the concept of galaxies and AGN in this Chapter, and explained the gaps in research that require further investigation to work towards a complete understanding of the underlying physics governing co-evolution. Chapters 3 and 4 describe our work using observations of AGN in disk-dominated galaxies to investigate the nature of the bar-AGN correlation. Chapter 3 in particular uses spectroscopy we obtained from Lick Observatory, which requires substantial data reduction prior to analysis, and this technical work is detailed in full below, in Chapter 2.

# Chapter 2

## Reduction of the Shane/Kast Data

### Abstract

We describe the data reduction and preliminary analysis conducted on a sample of AGN-host galaxies. These galaxies were selected for a proposal in order to investigate the merger-free co-evolution of galaxies and black holes (PI: B.D. Simmons). The initial proposal's key goals included separation of AGN flux from that of the host galaxy, measurement of accurate black hole masses, characterisation of host galaxy stellar properties, and measure stellar velocity dispersions.

The sample consists of luminous, Type 1 AGN that were observed in SDSS (using Galaxy Zoo 2) to have no classical bulge component, and little-to-no pseudobulge component. This allows for the extremes of merger-free black hole growth to be investigated.

### 2.1 Introduction

In order to investigate SMBH growth in the merger-free regime, we require a sample of AGN hosted in disk-dominated galaxies with little-to-no bulge com-

ponent. The sample used here was first compiled in [Simmons et al. \(2017b\)](#), and we summarise the sample selection here.

The initial sample of AGN is selected using the W2R sample ([Edelson & Malkan, 2012](#)), which were identified via a multi-wavelength approach using the Wide-Field Infrared Survey Explorer (*WISE*; [Wright et al., 2010](#)), Two Micron All-Sky Survey (2MASS; [Skrutskie et al., 2006](#)) and the *ROSAT* All-Sky Survey (RASS; [Voges et al., 1999](#)). This photometric, all-sky selection combines both infrared and X-Ray selection to identify 4,316 unobscured AGN ([Edelson & Malkan, 2012](#)). The W2R sample exploits the fact that unobscured, Type 1 AGN exhibit a power law in the near- to mid- IR regime of their SED. They are also highly luminous in the X-ray regime, and thus by combining IR (from *WISE*/2MASS) and X-ray (from RASS), a sample of Type 1 AGN can be collated with a  $\gtrsim 95\%$  confidence limit. Full details can be found in [Edelson & Malkan \(2012\)](#), but in brief, a parameter is constructed from the *W1*, *W2* and *W3* bands in *WISE* (centred at  $3.4\ \mu\text{m}$ ,  $4.6\ \mu\text{m}$  and  $12\ \mu\text{m}$  respectively) and the *H* and *K* bands in 2MASS (centred at  $1.65\ \mu\text{m}$  and  $2.16\ \mu\text{m}$  respectively) in order to select IR-luminous sources. A second parameter is then constructed from the distance to the nearest source in RASS. The combination of these two parameters ensures brightness in both IR and X-ray wavelengths. [Simmons et al. \(2017b\)](#) use the Sloan Digital Sky Survey (SDSS; [York et al., 2000](#)) to select from the AGN sample a set of galaxies that are dominated by the presence of a disk. Using SDSS Data Release 8 (DR8; [Aihara et al., 2011](#)), there are 1,844 sources within 3 arcsec of a source in the W2R sample. A single expert classifier (BDS) used the SDSS colour images to perform a morphological selection, and found that there were 137 galaxies lacking visual evidence of a bulge component, but containing features commonly found in disks (spiral arms, bars etc.). Around a third of these galaxies have SDSS fibre spectra focused on the nuclei of each source. However, in order to reliably determine SFRs in these Type 1 AGN with very strong emission lines, we require off-nuclear spectra.

This sample of 137, spatially-resolved, unambiguously disk-dominated, AGN-host galaxies formed the basis for the observing proposal to investigate SMBH–galaxy co-evolution in the absence of major mergers. However, due to limited telescope time, data observations were only requested for 89 of these galaxies,

based up the time of year, location of the telescope, and prioritisation of those galaxies for which SDSS fibre spectra were unavailable. Additionally, time was requested for 31 inactive, disk-dominated comparison galaxies.

Not all of the 120 galaxies for which time was requested were used in Chapter 3, since a comparison sample of inactive galaxies was obtained using SDSS fibre spectrum data available in the MPA-JHU catalogue. 33 of the active galaxies were omitted from Chapter 3 due to not being successfully observed, or due to bad spectra (for example, spectra where there was no discernable signal at any wavelength, spectra where the level of cosmic ray contamination was too great to successfully remove).

The sample was observed using the Kast Double Spectrograph on the Shane Telescope at Lick Observatory, California, USA. The Shane Telescope uses a 3 m mirror with a 3-foci design, shown in Figure 2.1, along with a diagram of the Kast Double Spectrograph. This spectrograph has been in use since 1992, at the Cassegrain focus, and consists of two charge-coupled devices (CCDs), referred to hereafter as the blue and red CCDs. The blue CCD has a wavelength range of good performance of 3,000 Å to 7,000 Å, and the red CCD has a range of 4,000 Å to 11,000 Å.

Observations were conducted over 25 nights from October 2016 to November 2018 (PI: B.D. Simmons), although on 3 nights there were no useful observations taken due to poor weather. On the remaining 22 nights, the weather was generally clear with some light cloud cover. The goal was to obtain a signal-to-noise ratio of  $S/N \gtrsim 10$  for each galaxy at a minimum of two position angles (preferably orthogonal to each other), however due to weather conditions, 95 of the 120 were observed at two or more angles, and 25 at one angle. Most observations were taken with a slit width of either 1.5", 2" or 3", although in a handful of cases the slit width was as low as 0.5". This variation in slit width was to ensure the entire FWHM of the AGN was within the slit in order to not waste flux. The exposure time for each source varied, but was generally between 500 seconds and 2000 seconds, in order to obtain a signal-to-noise ratio of  $S/N \gtrsim 10$ . The standard configuration of the spectrograph was used: dichroic d57; blue grating 600/4310, red grating 600/7500. The observations, including SDSS DR7 galaxy ID, RA, Dec, position angles, and exposure times for this run are shown in Table

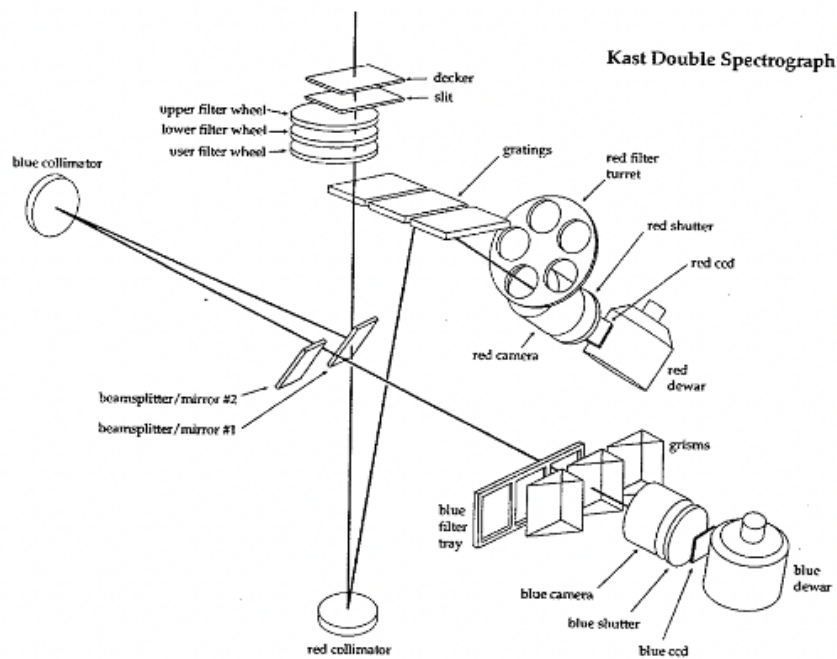
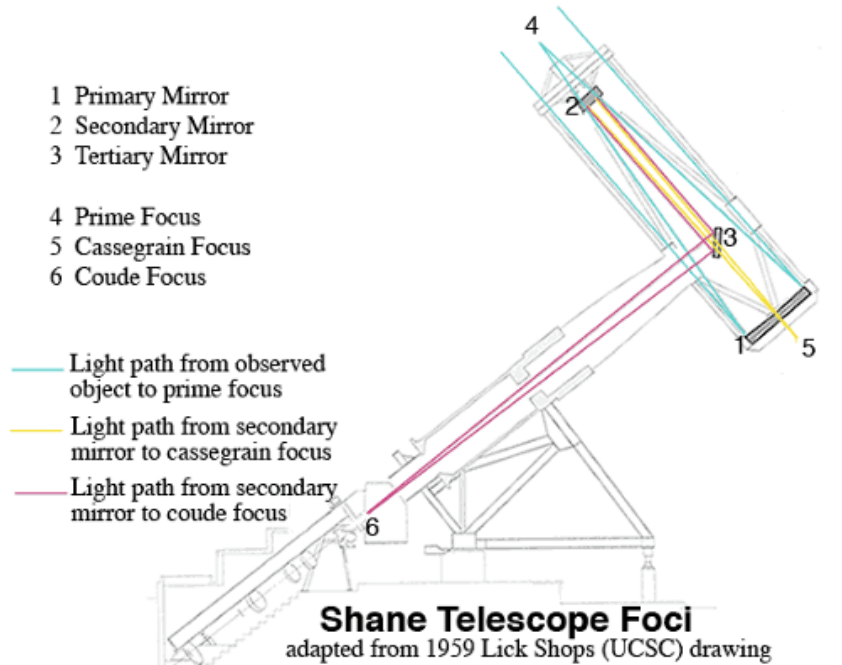


**Figure 2.1:** The path taken by incoming light through the Shane Telescope (top; [Lick-Observatory, 2021](#)) and the Kast Double Spectrograph (bottom; [Miller, 1994](#)). The spectrograph is mounted at the Cassegrain focus, not the Coude focus, so only the blue and yellow paths are utilised here.

**B.1**, with galaxies then used in Chapter 3 highlighted in bold. Some galaxies were not used due to their signal-to-noise ratio being insufficient, or the observations being unsuccessful. The standard stars, used for flux calibrations (Chapter 2.2.4) are shown in Table B.2.

In Section 2.2, we describe the steps taken to reduce the data (in brief: overscan subtraction, debiasing, flatfielding, wavelength calibration, background subtraction, flux calibration), and the fitting of the spectra is detailed in Section 2.3.

## 2.2 Reduction

The data reduction was done predominantly in IRAF (Tody, 1986, 1993), using packages designed specifically for working with longslit spectra, primarily `noao.twodspec.longslit` and `noao.twodspec.apextract`. In the following chapters, we discuss the steps taken to reduce the data. The analysis is discussed in Chapter 2.3.

### 2.2.1 Overscan, Biases and Flats

Every image taken with the Kast Double Spectrograph contains an overscan region, which is a part of the CCD that is not exposed to light. The python script provided by Lick Observatory takes the median of this overscan region for each image and subtracts it across the CCD. This can assist with the removal of small deviations in the bias level across the chip.

Once the overscan has been trimmed and subtracted, the images need debiasing. When imaging with a CCD, each pixel has a voltage applied to it as an offset. This means that when voltage is converted to counts, the counts are always non-negative. However, these excess counts caused by this offset then need subtracting in a process known as debiasing. For each night of observing, we took between 10 and 60 bias frames. This is an image with an exposure time of zero seconds with the mirror shutters closed, and allows us to measure the bias caused by the additional voltage across the chip. We combined the bias frames

into master bias images by taking the median value at each pixel for each CCD and subtracted them from the rest of the images.

The next stage is to counter for any differences across the CCDs in their reaction to light, known as flat-fielding. Dome flats are obtained by taking a short exposure of the inside of the dome with the Shane Telescope’s blue lamp. This provides a known spectrum of even illumination across the CCD. We took between 10 and 50 flats for each CCD at each slit width, ensuring the count number was roughly half that of the saturation level, thus ensuring that the dominant source of uncertainty is the Poisson uncertainty. The mean of the flats was taken for each CCD, resulting in a flat-field for the blue CCD and a flat-field for the red CCD.

We fit response functions to the flats in order that we could separate the SED of the flat from the pixel response, since only the pixel response is required to flat-field our science images. We used IRAF’s built in cubic spline function as our response function, as this gave better fits than the alternate options (Chebyshev function or Legendre function). This gave us the pixel response flats for each CCD *i.e.*, how sensitive each pixel is to light entering the telescope. The ‘science images’ (images of the sources and the standard stars) are then divided by the pixel response flats. It is worth noting here that each image must be flat-fielded using a dome flat taken with the same slit width. Thus, on nights where multiple slit widths were used, this process was done separately for each different slit width used throughout the night.

We removed cosmic rays in python using the `ccdproc` package `LACosmic`, leaving us with each science image having been through overscan subtraction, bias subtraction, flat-fielding, and cosmic ray removal.

### 2.2.2 CCD Calibration

On each night of observing, between 1 and 3 arc images were taken for each CCD. These are frames taken with one or more lamps switched on in the dome that emit a clear emission spectrum. Given that they sample different wavelength ranges, this was done separately for the red and blue CCDs. The lamps used for the blue CCD were He and Hg-Cd, and for the red CCD, Spare\_Ar, Hg-A and Ne, with an

exposure time that ensured none of the lines were saturated, generally between 2 and 60 seconds. The lines were then identified in `IRAF`, ensuring that a range of lines were identified across the whole of each CCD to optimise the calibration.

We then performed a spectrum trace using one of the standard stars observed on the night. We defined the aperture of the PSF of the standard star as a 1D dispersion plot, and then fit this across the CCD.

By then applying these two calibrations, the wavelength and the trace, to the science images, the CCDs were calibrated in both directions — wavelength and spatial. The wavelength calibration ensures an accurate reading of the wavelength, and the spatial calibration ensures an accurate positional measurement. Flux calibration was done later (see Chapter 2.2.4).

### 2.2.3 Background Subtraction

When observing, it is generally more efficient to take multiple shorter exposures, and combine the frames together, than to take one longer exposure. This is in case of problems, such as satellites, telescope or software malfunctions, stray alpha particles<sup>1</sup>, cosmic rays (if any were missed by the subtraction procedure above), or saturation of pixels. This means however, that the frames need combining in the reduction phase. We combined by taking the median at each pixel of the calibrated, flattened, overscan and bias subtracted images taken to produce one science image per CCD per angle per source.

The next stage of reduction was to remove the sky background. This is the light that is coming from across the sky, and is strongly dependent on conditions at the time of observing, such as light from the moon, light pollution from humans and humidity. We completed this step using `IRAF` for each individual science image. We fitted a polynomial to some selected regions of the background, and removed this from the image.

We then corrected for atmospheric extinction, which is the altering of the spectrum by the atmosphere due to light being absorbed and/or scattered out of

---

<sup>1</sup>The dewar window at the telescope contained a radioactive component, which emitted alpha particles directly onto the CCDs. A new one was ordered, so this only affected the October 2016 observations.

the line of sight. The more atmosphere the incoming light has to travel through, the more the spectrum is altered. This is highly dependent on the altitude of the observatory, as this determines through how much atmosphere the observation is being made. For the altitude of Lick, 1200 m, we used IRAF's built in `kpno` model.

### 2.2.4 Flux Calibration

Spectrophotometric standard stars are stars with accurately measured spectra. By comparing the known values of the stellar spectrum to the output across the CCD, the CCD is calibrated in the flux dimension. It is more accurate to match each galaxy source image to a standard star taken very close throughout the night, both in RA and Dec, and in time. This means that the observed spectrum takes into account conditions that will match the source observation as closely as possible. Effects like turbulence may not be the same across the sky, hence the reason for an RA and Dec that are similar to the source. These effects may change throughout the night, hence the reason for similarly timed observations. For this reason, many standard star frames were taken throughout the night at regular intervals, listed in Table B.2.

The first step of this process was to extract a 1D spectrum from each standard star, using the built in IRAF tasks. We defined the aperture, subtracted the background, and mapped how the spectrum fluctuates over the CCD.

After extracting the spectra of each star (one for the blue CCD, one for the red), we defined the calibration regions. These are regions of a spectrum that we then compared to the known values (stored within IRAF's libraries).

Finally, we modelled the sensitivity of the detector by fitting a sensitivity polynomial function across the calibration regions, using the built in IRAF task `sensfunc`. This takes the previously defined calibration regions, and compares them to the known values. The order of the polynomial varied, but was generally around order 7. The sensitivity function allows us to model how the known, and the newly observed standard star spectra differ, in order that this can be taken into account for the science images. The sensitivity function was applied

to our science images to flux calibrate them, leaving us with flux, wavelength and spatially calibrated, 2D science images.

### 2.2.5 Extraction of 1D Spectra

For the work described in Chapter 3.2, we needed to extract a spectrum of the galaxy, and a spectrum of the AGN, per science image. To extract the AGN spectrum, we defined an aperture such that it covered the brightest region (typically the central 5 pixels, shown between the teal lines in Figure 2.2) and extracted this. We visually checked with SDSS images (or HST where available) that the brightest region was due to the AGN, and not an artefact, or a bright clump. We PSF-corrected the AGN, and this is covered below.

To extract the galaxy spectrum, we used the relevant standard star to find the PSF of the instrument at that time, assuming the PSF could be modelled with a Gaussian distribution. The parameter,  $\sigma$ , was then found using DS9, where  $1\sigma$  either side of the centre encloses 68% of the flux of the PSF,  $2\sigma$  encloses 95%, and  $3\sigma$  encloses 99.7%. We defined the aperture of the galaxy spectrum such that it started  $3\sigma$  away from the centre of the AGN peak, and ended at the edge of the galaxy, with the assistance of SDSS images (shown between the yellow dashed lines in Figure 2.2, and converting pixels on SDSS to pixels on Kast. This therefore enclosed 0.15% of the AGN flux, since it is only one half of the Gaussian. This was useful later when the AGN flux was subtracted from the galaxy flux (see Section 2.3.2). We ensured we were doing this on the same side of the slit for both the red and the blue CCD. If after doing this, there was no discernable flux in the galaxy spectrum, we expanded our aperture down to  $2\sigma$  away from the centre of the AGN peak, taking care to note where this happened in preparation for subtracting AGN flux from the the galaxy flux.

Once the spectra had been extracted, we combined the red and the blue CCD spectra into one cohesive spectrum, taking the mean at any point of overlap. This resulted in one AGN spectrum and one galaxy spectrum per angle per source.

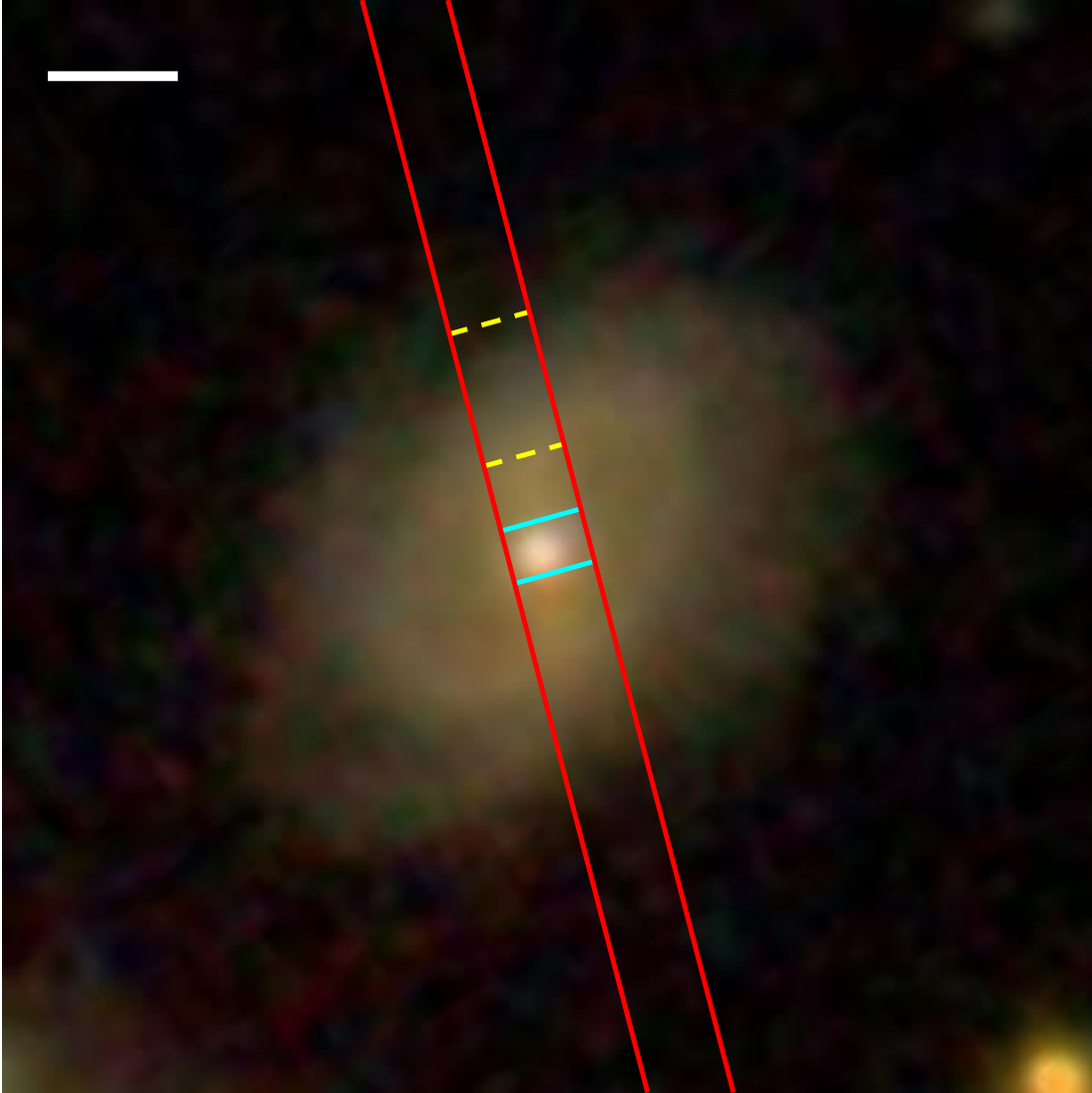


**Figure 2.2:** SDSS postage stamp of J081324.00+542236.9, overlain with the observed region, a slit of length 145 arcsec, shown as a red rectangle. The teal lines denote the 1D spectrum extracted from the central 5 arcsec of the slit, corresponding to the central spectrum shown in Figure 3.1. The yellow lines denote the 1D spectrum extracted over the galaxy disk and is also shown in Figure 3.3. The scale bar shown in the top left corner corresponds to 10 arcsec.

## 2.3 Analysis of the Spectra

### 2.3.1 Redshift Determination

Some of our sources already had redshift measurements from SDSS spectra, but for the remainder, this requires calculation. We did this using the [OIII] $\lambda$ 5007 Å line where available, resorting to the H $\alpha$  $\lambda$ 6563 Å line if needed (approximately a third of sources). We fitted a Gaussian to the emission line, and took the peak to be the observed wavelength,  $\lambda_{\text{obs}}$ . This was converted to a redshift using

$$z = \frac{\lambda_{\text{obs}} - \lambda_{\text{emit}}}{\lambda_{\text{emit}}} \quad (2.1)$$

where  $z$  is the redshift and  $\lambda_{\text{emit}}$  is the emitted wavelength. We preferentially used [OIII] $\lambda$ 5007 Å, since H $\alpha$  $\lambda$ 6563 Å is part of a blended emission complex including [NII] $\lambda$  $\lambda$ 6548 Å, 6583 Å, making identification of the H $\alpha$  peak more uncertain.

### 2.3.2 Fitting the spectra and accounting for AGN flux leakage

We fitted both the AGN and the galaxy 1D spectra using python, including packages such as `scipy` (Virtanen et al., 2020) and `astropy` (Astropy Collaboration et al., 2013, 2018) — packages designed specifically for working with data and astronomical data. Given that we were only primarily concerned with the H $\alpha$  flux, we focussed on obtaining good fits to the H $\alpha$ /[NII] complex, located around 6563 Å in the rest-frame spectra. We attempted a number of different fitting methods (fitting just a small window versus fitting the whole spectrum simultaneously, fitting Gaussian versus Lorentz curves, adding broad components versus only using narrow). In the majority of cases, we could fit the entire spectrum using Gaussian functions, incorporating broad emission lines into the AGN spectra, although for around a third of the sources, the signal-to-noise throughout the rest of the spectrum was insufficient, and we only attempted to fit the H $\alpha$ /[NII] region. Some example fits are shown in Figure 2.3.

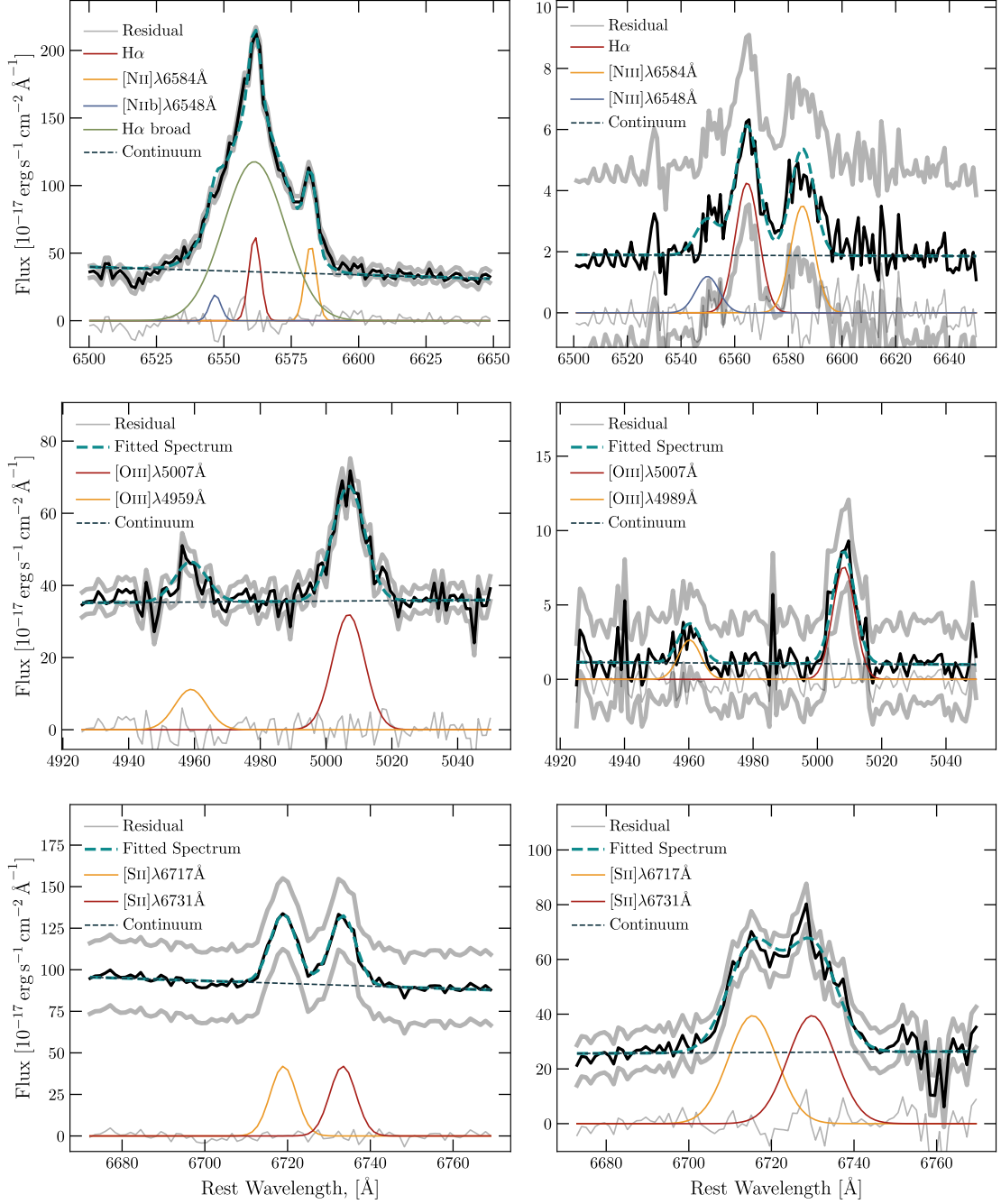


**Figure 2.3:** Example fits to AGN spectra on the left and galaxy spectra on the right. The region being fitted is indicated in the legend of each, and the fit is shown in the dashed teal line in each plot. Note that these are taken from different sources as opposed to being selected from the same source.

Given that the instrument has a non-negligible PSF, it would be highly unlikely that no flux from the AGN had ‘leaked’ into the galaxy spectrum. Thus, we subtracted any AGN flux. As we described in Chapter 2.2.5, we know how much AGN contamination there is. This made it very simple to calculate 0.15% of the AGN flux (where the extraction of the galaxy spectrum began  $3\sigma$  away) or 2.5% of the AGN flux (where the extraction of the galaxy spectrum began  $2\sigma$  away) and subtract this from the galaxy spectrum. Upon doing this, in some cases the resultant galaxy spectrum contained no signal, and thus for analysis we had to resort to using upper limits on the flux. As explained in detail in Chapter 3.3.2.1, this turned out to be insufficient for analysis.

Where we had multiple slit angles over the same source, these were treated like individual spectra during the fitting process. Once the fits had been used to calculate the total  $H\alpha$  flux coming from the galaxy, we took the mean of all different angles for each source to obtain our final flux value. Where one of the slit angles was able to be precisely fitted, but for another we could only obtain upper limits on  $H\alpha$ , we disregarded the values obtained from the upper limit. Where all of the slit angles resulted in spectra for which we could only obtain an upper limit, we adopted a conservative approach, and took the highest upper limit for each source.

Following the method of data reduction and AGN separation outlined above, we obtained  $H\alpha$  fluxes for 34 galaxies hosting AGN, and  $H\alpha$  flux upper limits for a further 22 galaxies hosting AGN. The parameters of these galaxies are laid out in Chapter 3, Table 3.1, where they are utilised to investigate the link between AGN and large-scale galactic bars.

## Chapter 3

# The most luminous, merger-free AGN show only marginal correlation with bar presence

### Abstract

The role of large-scale bars in the fuelling of active galactic nuclei (AGN) is still debated, even as evidence mounts that black hole growth in the absence of galaxy mergers cumulatively dominates and may substantially influence disk (*i.e.*, merger-free) galaxy evolution. We investigate whether large-scale galactic bars are a good candidate for merger-free AGN fuelling. Specifically, we combine slit spectroscopy and *Hubble Space Telescope* imagery to characterise star formation rates (SFRs) and stellar masses of the unambiguously disk-dominated host galaxies of a sample of luminous, Type 1 AGN with  $0.02 < z < 0.24$ . After carefully correcting for AGN signal, we find no clear difference in SFR between AGN hosts and a stellar mass-matched sample of galaxies lacking an AGN ( $0.013 < z < 0.19$ ), although this could be due to small sample size ( $n_{\text{AGN}} = 34$ ). We correct for SFR and stellar mass to minimise selection biases, and compare the bar fraction in the two samples. We find that AGN are marginally ( $\sim 1.7\sigma$ ) more likely to host a

bar than inactive galaxies, with AGN hosts having a bar fraction,  $f_{\text{bar}} = 0.59^{+0.08}_{-0.09}$  and inactive galaxies having a bar fraction,  $f_{\text{bar}} = 0.44^{+0.08}_{-0.09}$ . However, we find no further differences between SFR- and mass-matched AGN and inactive samples. While bars *could* potentially trigger AGN activity, they appear to have no further, unique effect on a galaxy’s stellar mass or SFR.

### 3.1 Introduction

There are still many fundamental open questions about the interplay between galaxies and the supermassive black holes (SMBHs) they host. For example, whilst major galaxy mergers were thought to dominate black hole–galaxy co-evolution in previous decades (*e.g.*, [Kormendy & Ho, 2013](#)), more recent results have made clear that merger-free (sometimes called ‘secular’) processes are at least as important to the overall growth and evolution of black holes and galaxies as mergers, with their black hole–galaxy properties showing the same correlations as those undergoing merger-driven growth (*e.g.*, [Simmons et al., 2017b](#)), as described in more detail below.

From the theoretical perspective, multiple cosmological simulations find that a dominant majority of black hole growth occurs as a result of merger-free processes (at least 65%, possibly more than 85%, depending on the simulation; [Martin et al., 2018](#); [McAlpine et al., 2020](#)). Observational works have long been accumulating evidence for the merger-free black hole growth pathway ([Greene et al., 2010](#); [Jiang et al., 2011](#); [Cisternas et al., 2011](#); [Schawinski et al., 2011](#); [Kocevski et al., 2012](#); [Simmons et al., 2011, 2012, 2013](#); [Smethurst et al., 2021](#)), where often merger-free growth is isolated via the study of strongly disk-dominated galaxies (which have not had a significant merger since  $z \sim 2$ ; [Martig et al., 2012](#)).

Given the diversity of evidence for substantial merger-free black hole growth at a range of redshifts, there must be a significant mechanism of fuelling AGN in the absence of major mergers. In these secularly built, disk-dominated galaxies, gas must still be transported to the central regions in order for an AGN to be present. [Smethurst et al. \(2019\)](#) calculate the necessary inflow rate (*i.e.*, the minimum gas mass that must be provided by any means to the central SMBH) for

their sample of AGN in disk-dominated galaxies, and show that bars (Shlosman et al., 1989, 1990; Knapen et al., 1995; Sakamoto et al., 1999; Maciejewski et al., 2002; Regan & Teuben, 2004; Lin et al., 2013), spiral arms (Maciejewski, 2004; Davies et al., 2009; Schnorr-Müller et al., 2014), and the smooth accretion of cold gas (Kereš et al., 2005; Sancisi et al., 2008) can each match the inflow rate required to sustain an AGN. These are all morphological features with a long lifespan (Miller & Smith, 1979; Sparke & Sellwood, 1987; Donner & Thomasson, 1994; D’Onghia et al., 2013; Hunt et al., 2018), orders of magnitude longer than the  $\sim 10^5$  yr phases within the lifetime of an AGN (Schawinski et al., 2015), so if these features are able to periodically feed the SMBH (Schawinski et al., 2015) over their lifetimes, then the mass of the SMBH can grow to the masses observed in the present. In other words, the secular, calm processes seen in disk-dominated galaxies are more than capable of fuelling AGN (Smethurst et al., 2019).

Large-scale galactic bars, in particular, are a common feature in the local Universe, with Masters et al. (2011) estimating that around  $29.4 \pm 0.5\%$  of disk galaxies at redshift  $0.01 < z < 0.06$  host a large-scale, strong galactic bar when observed in optical wavelengths. Barazza et al. (2008) examine bar fraction in the  $r$ -band specifically, and report a bar fraction of 48% to 52%, however in infrared imaging, a bar fraction as high as 70% has been observed (Mulchaey & Regan, 1997; Knapen et al., 2000; Eskridge et al., 2000). Theoretical studies of AGN fuelling in disk galaxies show that bars are a viable method of transporting matter to a central SMBH (Friedli & Benz, 1993; Athanassoula, 1992, 2003; Ann & Thakur, 2005).

Despite bars being relatively common in disk galaxies and theoretically able to power a luminous AGN, observing such a connection has proven difficult. Many studies find no correlation between bars and AGN (Martini et al., 2003; Lee et al., 2012; Cheung et al., 2015; Goulding et al., 2017), whereas studies such as Knapen et al. (2000), Laine et al. (2002), Laurikainen et al. (2004) and Oh et al. (2012) show there is an increase in the number of AGN-host galaxies containing bars of around 20%. Galloway et al. (2015) note that there is a higher probability of an AGN-host galaxy possessing a strong bar than a galaxy without an AGN, but find no link between bars and the quantity or efficiency of AGN fuelling, indicating that whilst the presence of a strong bar may trigger the ‘switch on’ of the AGN,

the bar then drives accretion in a way that is indistinguishable from the secular processes that would be fuelling the AGN in the bar's absence.

Several factors likely contribute to the difficulty of observing a connection between AGN and bars. AGN are more likely to reside in galaxies with a higher stellar mass,  $M_*$  (Kauffmann et al., 2003c; Aird et al., 2012), and a correlation between bars and stellar mass has been observed, although the nature of this correlation is debated, potentially with bars being more likely to reside in galaxies with a higher stellar mass (*e.g.*, Skibba et al., 2012), although a study conducted in Erwin (2018) highlights that this may be a selection effect, and shows that bar presence may peak at  $\log(M_*/M_\odot) = 9.7$  and decrease either side of this value. Bars are also more likely to reside in redder galaxies (*i.e.*, less star-forming) (Masters et al., 2011, 2012; Skibba et al., 2012; Oh et al., 2012; Cheung et al., 2013; Kruk et al., 2018; Geron et al., 2021), but in some cases, enhancement of star formation rate (SFR) in a circumnuclear ring at the centre has been observed (Hawarden et al., 1986). Controlling for these confounding variables in order to understand how bars, star formation, and black hole growth may affect each other requires large samples and careful measurements.

There is another crucial caveat in determining any link between bars and AGN which causes significant problems: both features have drastically different typical lifetimes. SMBH tend to only be in the AGN phase for around  $10^5$  yr (Schawinski et al., 2015), whereas bars are long-lived features (Sellwood, 2014), with simulations showing bars that form at  $z \sim 1.3$  can maintain their strength down to  $z \sim 0$  (Kraljic et al., 2012). This corresponds to a lookback time of 8.9 Gyr, meaning that bars can live at least 100,000 times as long as an AGN phase. This means that when a barred galaxy is observed, we may not observe AGN activity because the AGN has since faded. Since bars tend to facilitate the development of pseudobulges over time via the buckling of stellar orbits (see Combes 2009 for a review), observing galaxies with no or very small bulges may aid in mitigating this issue, as then any bars observed would be younger, and have less chance of outliving an AGN at the time of observation.

There is also very little consensus on the link between AGN and SFR (*e.g.*, Mulcahey et al., 2022). Additionally, it is a challenge to measure SFRs in galaxies hosting luminous AGN. Star formation and AGN appear to share a common fuel

source (Silverman et al., 2009); thus if there is more of this fuel source, we would expect to see an increase in AGN and in SFR appearing together. This has been observed (*e.g.*, Mullaney et al., 2012; Aird et al., 2019). However, AGN feedback has also been shown to be capable of affecting the star formation in the host galaxy. For example, positive feedback can occur when an outflow compresses the molecular clouds or the interstellar medium in its path, thus increasing SFR (Ishibashi & Fabian, 2012; Schaye et al., 2015). Negative feedback can quench star formation via heating the molecular gas and interstellar medium (*e.g.*, Ciotti et al., 2010). See Fabian (2012) for a review on AGN feedback and star formation.

In this work, we examine AGN in unambiguously disk-dominated (‘bulgeless’) galaxies in order to isolate SMBH growth in the merger-free regime. As mentioned above, these disk-dominated galaxies indicate a merger-free history since at least  $z \sim 2$ , due to mergers resulting in a central bulge (Martig et al., 2012). Previous studies have shown that these AGN exist at a range of black hole masses and luminosities, (Satyapal et al., 2009; Simmons et al., 2013; Bizocchi et al., 2014; Satyapal et al., 2016). Simmons, Smethurst & Lintott (2017b) compiled a sample of relatively nearby ( $z < 0.25$ ) unobscured, luminous AGN residing in disk-dominated systems. Despite having long-term evolutionary histories free of significant mergers, these systems lie on SMBH–galaxy co-evolution relations which were originally observed in elliptical galaxies with a history of major mergers (Häring & Rix, 2004). This unique sample of merger-free quasars is the parent sample for the data used in this work. There has not yet been a detailed study of bars and AGN in these systems in the same way that there has been in the general galaxy population.

We use spectra taken from the Shane Telescope at Lick Observatory to examine the SFRs in merger-free galaxies hosting luminous AGN. We also investigate whether, after controlling for parameters such as SFR and  $M_*$ , a correlation can be observed between the presence of a bar and the presence of an AGN. We discuss data collection, comparison samples and fitting procedures in Chapter 3.2, and we determine stellar properties of our sample in Chapter 3.3. We discuss SFR in Chapter 3.4, and then examine the bar fractions in Chapter 3.5, before concluding in Chapter 3.6.

Throughout this paper, the term ‘active galaxy’ refers to a galaxy that hosts an AGN, and the term ‘inactive galaxy’ refers to a galaxy that does not host an AGN. These two terms do not refer to the star formation in the galaxy. We use WMAP9 cosmology (Hinshaw et al., 2013), where we assume a flat universe,  $H_0 = 69.3 \text{ km s}^{-1} \text{ Mpc}^{-1}$  and  $\Omega_m = 0.287$ .

## 3.2 Sample and Observations

This study uses multiple samples and data sources. In the subsections below, we describe our main sample of AGN-host galaxies, as well as our comparison sample of inactive disk galaxies. We further describe the data reduction, spectral fitting, and morphological fitting procedures used for each of these samples.

### 3.2.1 AGN-host Sample

Longslit spectroscopic data was taken from the Kast Spectrograph on the Shane Telescope at Lick Observatory over 18 nights in the period 2016 October to 2018 November for 56 unambiguously disk-dominated galaxies hosting AGN, in order to work towards spectroscopic completion of the parent sample — see Chapter 2.1 for a full description of the sample. Despite the 18 nights on sky, we were unable to obtain full spectroscopic completion of the sample, and 4 of these 137 sources have neither SDSS fibre spectra nor Lick longslit spectra. 21 of the sources have both longslit and fibre spectra. Throughout this work, this sample of 56 sources shall be referred to as AGNDISKS, and SDSS images of these sources are shown in Appendix C.1.

### 3.2.2 Inactive Sample

In order to investigate bar-driven fuelling of AGN, it is necessary to compare the AGN-host sample to a resolution-matched and morphology-matched sample of galaxies which lack AGN activity signatures but are otherwise similar. This allows us to separate out any properties that may appear to be a result of bar presence, but are actually a result of AGN presence, as well as provide a baseline

comparison for how a bar can affect a galaxy in the absence of an AGN. Typically, when selecting comparison samples, stellar mass is also matched, and whilst we do perform this matching later on in Chapter 3.4, we first want to see how the stellar mass (along with the star formation rate) varies between AGNDISKS and the inactive galaxies.

We used Galaxy Zoo 2 (GZ2; Willett et al., 2013) to first identify a sample of disk-dominated galaxies. Volunteers are shown an image from SDSS, and asked via the question tree shown in Willett et al. (2013) to classify the central galaxy in the image. The first question asked is “*Is the galaxy smooth and rounded, with no sign of a disk?*”, and for this work, we require that the vote fraction for those who answered that the galaxy is featured be  $p_{\text{features-or-disk}} \geq 0.35$ , following the suggestion in Galloway et al. (2015) based on expert visual inspection. This leads the volunteers who answered “*No*” (*i.e.*, the galaxy is featured) to the question “*Could this be a disk viewed edge-on?*”. We require a sample of face-on disks so that we can identify a bar if one is present. In an edge-on disk, the bar is often hidden by the geometry of the galaxy. We require that the vote fraction of volunteers classing the disk as not-edge-on be  $p_{\text{not-edge-on}} \geq 0.6$ , again following the suggestion in Galloway et al. (2015). This makes up our inactive disk sample.

To establish the lack of AGN, we use the fluxes from OSSY (Oh et al., 2011) to divide the sample into AGN hosts, star-forming galaxies, composite sources, and LINERs. To build the inactive sample, we exclusively use sources that fall into the star-forming category. This is to ensure purity of the sample. We exclude any source where the emission lines [OIII], [NII],  $H\alpha$ , and  $H\beta$  have a signal-to-noise ratio,  $S/N < 3$ . We use the guidance in Kauffmann et al. (2003c), where they show that a source is star-forming if it falls below the line shown in Equation 1.3.

We impose a limit on the resolution rather than the redshift, since the bars are identified visually. We need to ensure the resolution distribution of active galaxies covers the same range as our sample of inactive galaxies. This is particularly important given that the inactive galaxies have their bar presence determined through SDSS images (via GZ2 volunteers), but only around half of the active galaxies use SDSS for bar identification — the rest use *HST* images, which have a far better resolution and thus can push to higher redshift before the classification of bar presence is marred by significant doubt — see Chapter 3.2.4 for a more

detailed description of identifying bars. For AGN hosts with *HST* images, we determine what their equivalent redshift would be if they were observed solely with SDSS to obtain the same resolution in arcseconds per pixel. We use these equivalent redshifts to determine that the maximum redshift of our inactive sample should be  $z \leq 0.187$ . Ensuring this resolution matching is completed negates any issues that arise when identifying bars at different resolutions. After removing all inactive disks with  $z > 0.187$ , we are left with our comparison parent sample of 26,899 galaxies, which we refer to below as INACDISKS.

### 3.2.3 Data Reduction and Fitting

#### 3.2.3.1 Lick Data Reduction

The data were reduced according to the standard pipeline. The full data reduction is detailed in Section 2.2, but we briefly summarise here.

We used the Image Reduction and Analysis Facility (IRAF; Tody, 1986, 1993) to reduce the longslit AGNDISKS spectra, and its packages designed specifically for longslit data reduction, NOAO.TWODSPEC.LONGSLIT, and NOAO.TWODSPEC.APEXTRACT. The Kast spectrograph has a red CCD and a blue CCD, and these were reduced separately. The instrument settings for all runs were: dichroic d57; blue grating 600/4310, red grating 600/7500. The slit width ranged from 2–3 arcsec, with a wider slit used for nights with particularly poor seeing. The overscan regions were subtracted, and the images were bias-subtracted and flat-fielded. There were a number of images, particularly in the red side of the detector, which were contaminated with cosmic rays, and for spectra taken in October 2016, stray alpha particles from a slightly radioactive instrument component that was later replaced. These artefacts were removed, and the images were calibrated for wavelength, then stacked according to the object and position angle. The background noise was subtracted from each combined image, and the images were extinction corrected. Standard stars, from which data was taken regularly throughout the night, were used to calibrate the flux at each wavelength. The standard stars used were: BD332642, BD284211, BD262606, Feige 34, Feige 110, G191B2B, G193-74, G24-9, GD248, HD157881, HD183143, HD19445, HD84937, HZ4. We use

these standard stars to determine the point spread function (PSF) of the sources observed at that time. Since the standard stars are point sources, but have a Gaussian flux profile when observed, we can take the PSF to be the full-width-half-maximum (FWHM) of the flux of the star when plotted as a 2D spectrum.

Using longslit spectra means we can extract spectra at many points across the observed region, and we do this to obtain a spectrum of the central AGN in each source as well as an off-nuclear spectrum of the galaxy. The required 1D spectra were extracted; the 5 pixels around the central AGN to form the AGN spectrum, and the galaxy from either  $2\sigma$  or  $3\sigma$  of the PSF out to the edge of the disk to form the galaxy spectrum. Following reduction and extraction, the blue and red CCD outputs were merged to give two full spectra per position angle per object — one of the galaxy and one of the AGN. Since the two sides of the detector each have a different spectral resolution, it is necessary to interpolate the region where the CCDs overlap. We aperture correct the AGN spectra to account for cases where the width of the slit is small compared to the PSF of the AGN. We assume that the central spectrum is dominated by AGN flux. This is due to our sample being selected so as to be the most luminous AGN. The slit and extraction regions are demonstrated in Figure 2.2 for galaxy J081324.00+542236.9. We show the resultant spectra of J081324.00+542236.9 in Figure 3.1, including an AGN spectrum, a galaxy spectrum and a variance spectrum.

### 3.2.3.2 Spectral Fitting

To fit the spectra, we used `Scipy` (Virtanen et al., 2020), to fit a Gaussian function to each emission line, along with a linear fit for the continuum emission near the line. The focus was on obtaining robust  $H\alpha$  and  $[OIII]$  fits. For regions such as the  $H\alpha/[NII]$  complex, several Gaussian functions were used to disentangle overlapping emission lines, as shown in Figure 3.2.

Where the signal-to-noise ratio was too low and we could not obtain accurate  $H\alpha$  fits of the sources, we determined the upper limit of  $H\alpha$  flux by assuming all the flux in the region where a detectable  $H\alpha$  emission line would have been is due to  $H\alpha$  and integrating the spectrum in this range to give a conservative upper limit.

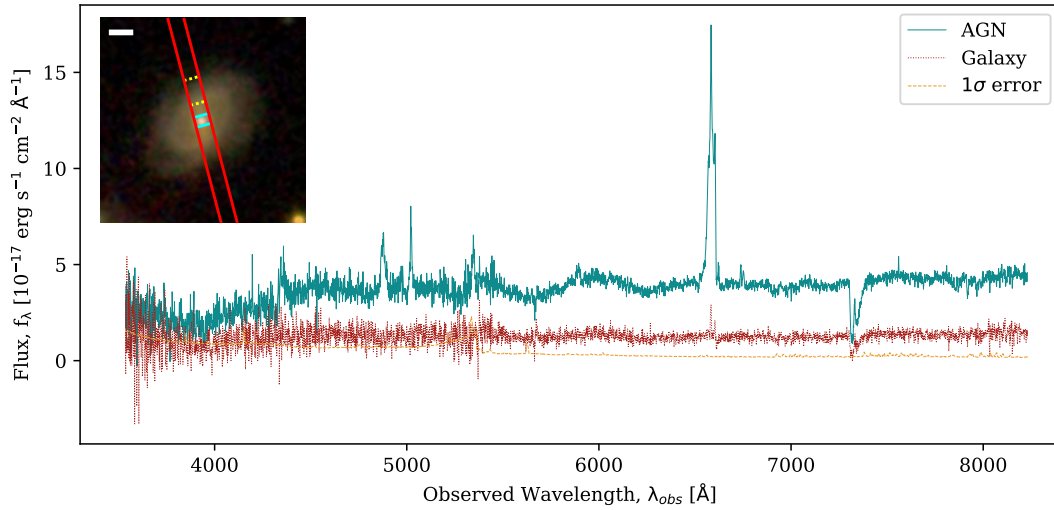


**Figure 3.1:** Full example spectra of J081324.00+542236.9 with AGN (solid teal line) and galaxy spectra (dotted red line) shown, and variance in the galaxy spectrum (dashed orange line). The thumbnail in the top left corner shows the galaxy from which these spectra were taken, and the red lines on the thumbnail represent the part of the image observed by the slit. The spectrum shown in red dashes is the spectrum taken over the galaxy, excluding a significant amount of the flux from the AGN. This corresponds to the section of the slit enclosed in neon yellow dashed lines. The spectrum shown in solid blue is the spectrum taken over the central five pixels of the source, which is dominated by the flux from the AGN. This corresponds to the section of the slit encased in solid neon blue. The  $H\alpha/[NII]$  is easily detected in both spectra, with an additional broad  $H\alpha$  component in the AGN spectrum. The  $[OIII]$  and  $H\beta$  emission lines are not apparent in the galaxy spectrum, but can be clearly seen in the AGN spectrum.

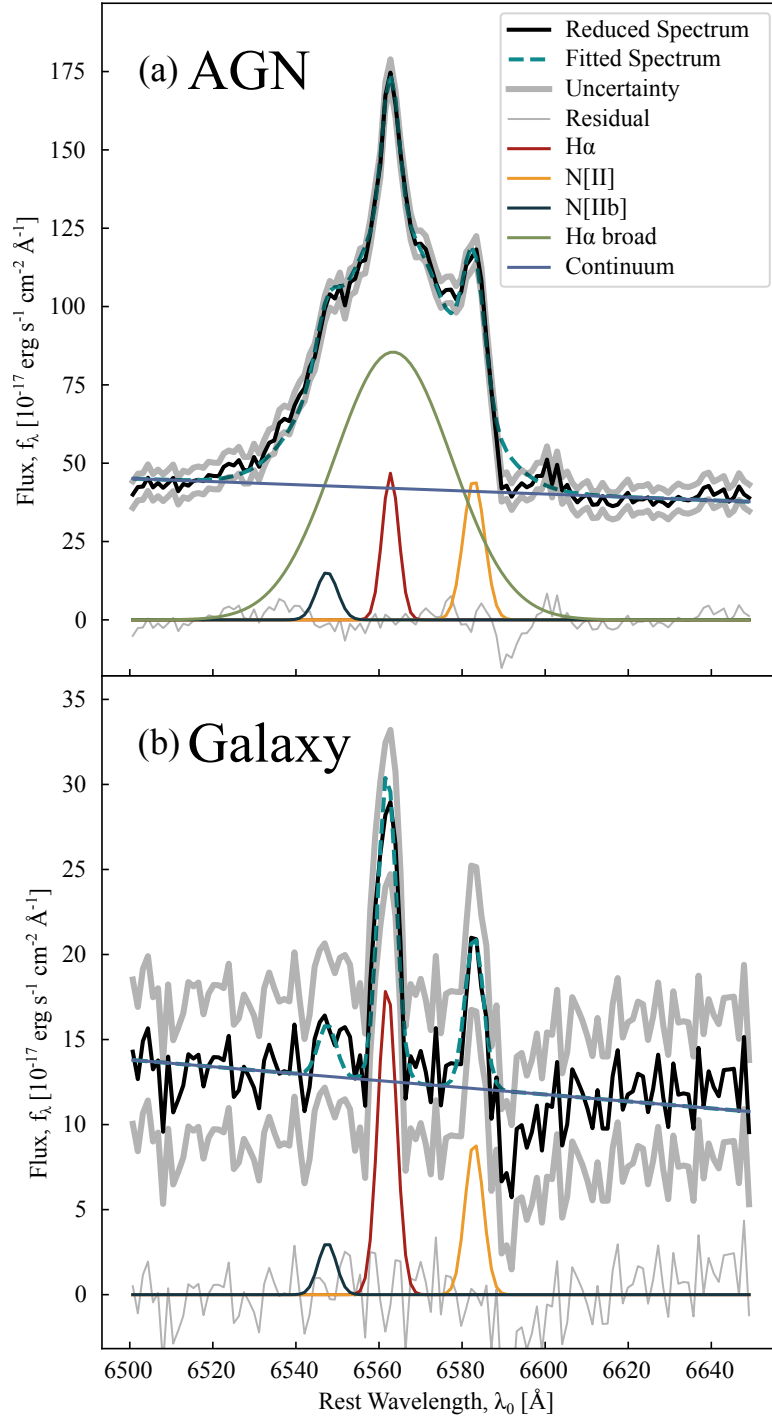


**Figure 3.2:** Fitted spectra, with Panel (a) showing the spectrum across the centre of the source including the AGN, and Panel (b) showing the spectrum across the galaxy. The reduced spectrum is shown in black solid lines, and the fitted spectrum is shown in dashed turquoise, with the uncertainty in grey thick lines and the residual in grey thin lines. The components making up the fit are also shown, with the continuum in blue H $\alpha$  in red, [NII] in yellow, [NIIb] in dark blue, and broad H $\alpha$  in green (only present in the AGN spectrum). The AGN spectrum primarily differs from the galaxy spectrum by the addition of this broad H $\alpha$  component.

The spectra taken over the centre of the system differ greatly to those taken of the galaxy. This is due to the presence of the AGN, which can add considerable flux and cause broadening. Thus, for all the AGN spectra, we require an extra Gaussian component for  $H\alpha$  with a higher velocity dispersion than the corresponding narrow component. This broad  $H\alpha$  component was also present in some of the off-nuclear spectra, and so was included in the fitting process since the AGN contaminant requires fitting before its successful removal. The differences in the galaxy and AGN spectra can be seen in Figure 3.2, with the AGN spectrum shown in Figure 3.2a and the galaxy spectrum shown in Figure 3.2b. Note that Type 1 AGN, as seen here, have both a broad and a narrow line component. Whilst every endeavour has been made to fully subtract the narrow line component, there may be a spatially extended narrow-line region, which has not been considered when removing AGN flux from the galaxy spectra. However, this is likely to be a negligible contribution to the flux in the galaxy spectrum (Smethurst et al., 2019).

Redshifts were calculated using spectral emission lines. We used the  $[OIII]5007\text{\AA}$  emission line as the reference wavelength where possible, however if for reasons such as low signal-to-noise the  $[OIII]5007\text{\AA}$  observed wavelength was unreliable, we used the  $H\alpha 6563\text{\AA}$  emission line.

After fitting the galaxy spectra, the AGN contaminant was subtracted. We observe that the Shane/Kast PSF is Gaussian by examination of standard star spectra. Thus where we extracted the galaxy spectrum from  $2\sigma$  away from the AGN to the edge of the disk, we subtract 2.5% of the AGN emission from the galaxy emission (since it is only one side of the PSF in the slit). Where instead we start at  $3\sigma$ , we subtract 0.015% of the AGN emission. This gives us a final AGN-host galaxy sample of 56 galaxies, 22 of which have upper limits constraining their  $H\alpha$  fluxes. This sample, which we refer to below as AGNDISKS, has median redshift  $z_{\text{med}} = 0.0857$ .

### 3.2.3.3 *HST* Data Reduction and Photometric Fitting

A subset of the AGN-host galaxies selected via the method described above and analysed here were also observed with the *Hubble Space Telescope* (*HST*) Ad-

vanced Camera for Surveys (ACS) as part of a snapshot programme (HST-GO-14606, PI: B. Simmons). Given that it was a snapshot programme, we prioritised those galaxies whose morphology was less clear in SDSS photometry, in order that confident morphologies could be obtained for all of AGNDISKS as well as accurate decomposition of AGN and host galaxy, which we cover in more detail below. Each of the 43 systems in AGNDISKS with *HST* imaging was observed in a single broadband optical filter, chosen to minimise the contribution of bright AGN emission depending on the redshift of the source (*i.e.*, to avoid either [OIII]/H $\beta$  or H $\alpha$  typically this choice resulted in selecting the *F814W* filter).

Each source was observed with 2 short exposures to ensure an unsaturated nuclear PSF, and 2 long exposures to reach an acceptable depth in the extended galaxy. A typical exposure time on source was approximately 40 minutes, with ACS/WFC subarrays chosen to minimise readout time whilst still imaging substantial sky background. The data was reduced using the standard reduction pipeline<sup>1</sup>, including CCD charge diffusion correction and cosmic ray removal using LACosmic (van Dokkum, 2001). The long exposures were combined into a final science exposure. For the purposes of photometric fitting (described below), image fluxes of the reduced images are in counts.

The availability of *HST* imaging for part of AGNDISKS facilitates more accurate structural decomposition of these sources than was originally possible using SDSS images. The full details of AGN host structural decomposition of the *HST* images will be presented in a separate work (M. Fahey et al, in preparation). Briefly, we used the two-dimensional parametric image fitting program GALFIT (Peng et al., 2002, 2010) to simultaneously model the unresolved nucleus and extended galaxy for each of the sources in AGNDISKS that has *HST* imagery. Each image was background-subtracted, and the sky model fixed to zero. We constructed an empirical PSF in each band using background-subtracted images of isolated stars drawn from every observation in the *HST* snapshot programme described above.

---

<sup>1</sup>At the time of data reduction, some manual steps were required as a result of using subarrays, but these configurations have since been incorporated into the standard imaging reduction pipeline.

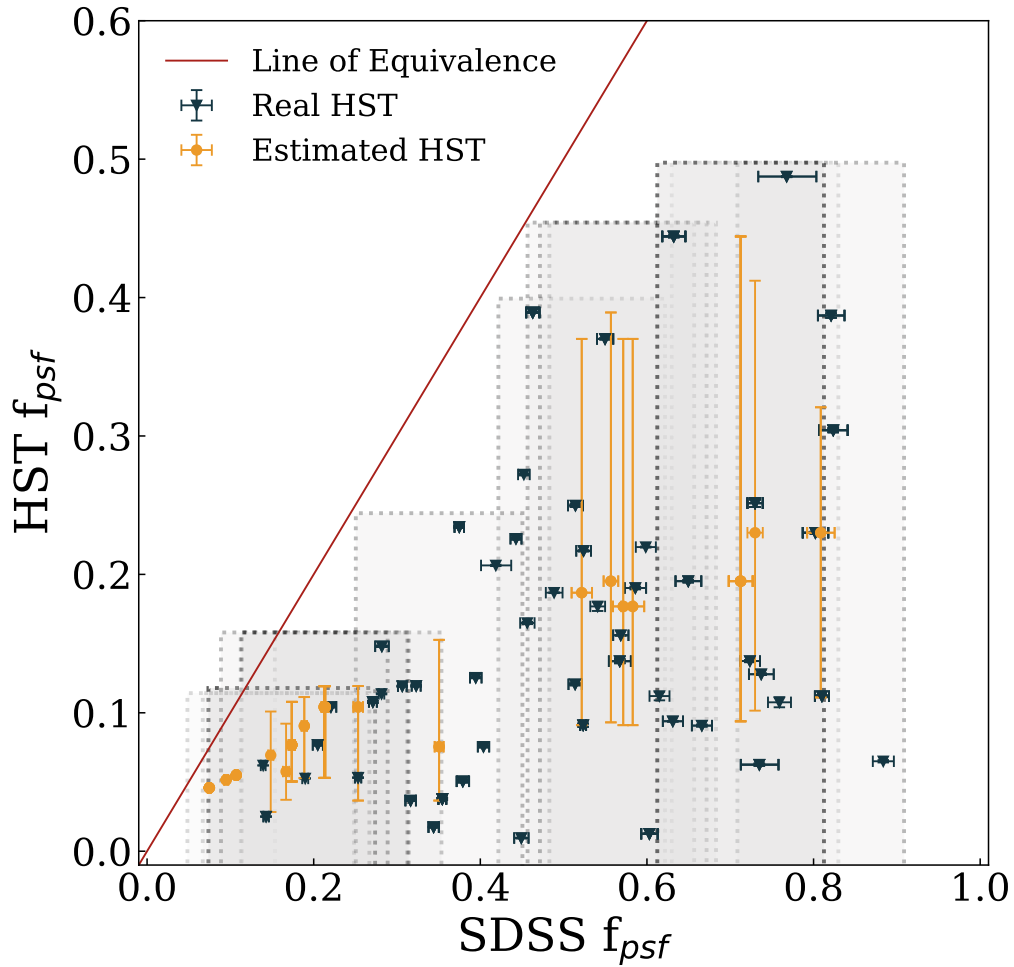


**Figure 3.3:** The fraction of the flux contained within the PSF for both *HST* and SDSS, with the sources observed with *HST* in dark blue, and those for which we are lacking *HST* data shown in orange. In light grey, we show the bins from which  $f_{\text{psf,HST}}$  is estimated where we do not have *HST* data. We take a bin surrounding the  $f_{\text{psf,SDSS}}$  point, of width 0.2. Using the median  $f_{\text{psf,HST}}$  values from the points within that bin, we determine the equivalent  $f_{\text{psf,HST}}$ . Thus there is one light grey bin for every source lacking *HST* data. The large error bars on the estimated  $f_{\text{psf,HST}}$  points are due to the large scatter. The fact that every point is either on or below the line of equivalence demonstrates that SDSS overestimates  $f_{\text{psf}}$ , and hence we need *HST* data.

We estimated initial guesses for fit parameters, using IRAF and SAOImage DS9 (Joye & Mandel, 2003) to measure central source positions and galaxy effective radii, as well as galaxy position angles and axis ratios. Each source was initially fit in an iterative ‘batch’ mode, starting with a single Sérsic (1968) profile for the galaxy model and a PSF for the AGN model. The host Sérsic index is set to  $n = 2.5$  and allowed to vary. This value was chosen so as to avoid favouring either an exponential disk ( $n = 1$ ) or a deVaucouleurs bulge ( $n = 4$ ). Where present, we also fit and subtract nearby bright stars and extended companion galaxies, and mask fainter compact sources from the fit. Subsequent batch-fitting iterations of each source involve additional galaxy components, including a compact Sérsic component to model a potential pseudo- or classical bulge.

Following the completion of batch fitting, we followed up each source to refine the fit. Where justified by inspection of fit residuals and reduced  $\chi^2_\nu$ , we refined the original fits and/or added additional components, including bars and spiral arms. In a few cases where the AGN emission saturated the detector in the long *HST* exposures, we determined the AGN-to-galaxy luminosity ratio using fits to the short-exposure images, fixing this AGN magnitude and masking out the saturated pixels in subsequent fits to the galaxy in the long-exposure images. The overall goal of the fits to each source was to neither over- nor under-subtract the galaxy’s central region. In addition, great care was taken to ensure the chosen galaxy best fit contains physically realistic component parameters.

The final photometric fits were used to determine the fraction of the total flux of the source coming from the AGN,  $f_{\text{psf}}$ . This was done by assuming that the PSF component measured from the *HST* images,  $f_{\text{psf,HST}}$ , is wholly due to the AGN point source in the centre of the system. For systems where *HST* imagery is available,  $f_{\text{psf}}$  is then calculated by dividing the fitted PSF by the sum of fluxes from all components. Throughout this paper, when referring to the galaxy flux, this is the the total flux multiplied by  $(1 - f_{\text{psf}})$ .

As mentioned above, *HST* images are not available for the entire AGNDISKS sample, and thus those sources lacking *HST* data require us to estimate their individual values of  $f_{\text{psf}}$ . All sources in AGNDISKS have an estimate of  $f_{\text{psf}}$  from SDSS. We calculate this value,  $f_{\text{psf,SDSS}}$ , for all sources in AGNDISKS using the psfMag and cModelMag SDSS photometric values to determine the PSF and total

source flux, respectively. As discussed in [Simmons et al. \(2017b\)](#),  $f_{\text{psf,SDSS}}$  is over-estimated for these systems given their bright nuclear emission and the resolution of SDSS compared to the size of the galaxies. Given that *HST* has a factor of  $\sim 8$  better resolution, we expect the *HST*-derived values of  $f_{\text{psf}}$  to be far more accurate. Figure 3.3 shows the values of  $f_{\text{psf}}$  from both SDSS and *HST* for each system with available *HST* images. The  $f_{\text{psf,SDSS}}$  is higher than  $f_{\text{psf,HST}}$  for *every* system, confirming the predictions of [Simmons et al. \(2017b\)](#). Additionally, the 43 systems in AGNDISKS with measurements from both SDSS and *HST* allow us to determine a relation between the lower-resolution and higher-resolution measures, which we apply to the remaining systems without *HST* data. Specifically, we determine a running median of the ratio between *HST* and SDSS PSF flux fractions, using a sampling width of 0.2 in SDSS PSF flux fraction. We extrapolate this median, assuming a linear increase, for the 6 data points outside the range of values observed in the subset of AGNDISKS with both *HST* and SDSS measurements. For each source lacking an *HST* image, we assume the *HST*  $f_{\text{psf}}$  is equal to the SDSS PSF fraction times the median ratio, with an uncertainty determined by sampling the scatter in the distribution at that value. The estimated values of  $f_{\text{psf}}$  and their uncertainties are shown in Figure 3.3.

### 3.2.4 Bar presence

There are several methods used to classify bars, most commonly via ellipse fitting (*e.g.*, [Regan & Elmegreen, 1997](#)), and visually (*e.g.*, [Nair & Abraham, 2010](#)). The method used is unlikely to affect final counts, as demonstrated in [Sheth et al. \(2008\)](#), who used both methods to classify their sample of over 2,000 face-on, spiral galaxies into strongly barred, intermediate barred and non-barred. They found that the two methods agreed in 85% of cases, and in a further 10% of cases, only disagreed by one class. A further method of bar classification is using GZ2, which classifies a galaxy’s bar status in the same style as the identification of disks (Chapter 3.2.2). Once a volunteer has established that the source is a disk that is not edge-on, they are asked “*Is there a sign of a bar feature through the centre of the galaxy?*”. GZ2 has been shown in multiple studies (*e.g.*, [Masters et al., 2011](#); [Simmons et al., 2014](#)) to robustly identify bars. [Melvin et al. \(2014\)](#) used Galaxy

Zoo Hubble (GZH), which follows the same question tree as GZ2, to investigate bar fraction with redshift, and their results are in strong agreement with [Sheth et al. \(2008\)](#). This shows that the three methods — ellipse fitting, visual, and Galaxy Zoo — can all be used in conjunction with each other to obtain robust classifications of bar status. Many previous GZ2 bar studies focus on strong bars, and thus use a relatively high threshold for bar selection (*e.g.*,  $p_{\text{bar}} \geq 0.5$ , where  $p_{\text{bar}}$  is *Zoobot*'s prediction of the fraction of volunteers that would label the galaxy as barred). [Willett et al. \(2013\)](#) show that the optimal GZ2 vote fraction for including both strong and weak bars in an analysis of population bar fractions is  $p_{\text{bar}} \geq 0.3$ — using the well established cut-off of  $p_{\text{bar}} \geq 0.5$  results in a sample of galaxies only with strong bars, rather than strong or weak bars, since more volunteers tend to label weakly barred galaxies as “unbarred” rather than “barred”.

For AGNDISKS, visual identification of a bar was performed by a single expert classifier (ILG) using the *HST* images for the 43 sources that have such data available. The same classifier then repeated this visual identification for the 23 sources for which we are lacking *HST* data using SDSS images of the galaxies. Only two galaxies in AGNDISKS had been classified in GZ2, thus we did not use GZ2 to identify bar presence. We note that due to the brightness of the AGN, we may have missed some smaller bars that would still be classed as galactic-scale, and acknowledge that this is an additional source of asymmetric uncertainty, and thus the true bar fraction for this sample may be higher than we show.

The bar status of all the galaxies in INACDISKS was determined using a GZ2 bar vote fraction threshold of  $p_{\text{bar}} \geq 0.3$ . A number of these were visually checked by ILG to ensure consistency with AGNDISKS. The results presented in Chapter [3.5](#) do not depend strongly on the vote fraction threshold.

### 3.2.5 Bulge Classification

We classify the galaxies in INACDISKS into those containing a bulge at the centre of their disk, and those that have a bulge prominence no greater than that in AGNDISKS, following the method outlined in [Masters et al. \(2019, Equation 3.1\)](#) to determine the bulge prominence,  $B_{\text{avg}}$  using GZ2. After deciding whether a

disk galaxy has a bar, volunteers are asked “*How prominent is the central bulge, compared with the rest of the galaxy?*” and presented with four options: “*No bulge*”, “*Just noticeable*”, “*Obvious*”, and “*Dominant*”.

$$B_{\text{avg}} = 0.2p_{\text{just noticeable}} + 0.8p_{\text{obvious}} + 1.0p_{\text{dominant}} \quad (3.1)$$

By visually inspecting whether a subsample of galaxies are visually bulgeless, we determine what value of  $B_{\text{avg}}$  we require so that the bulge prominence parameter agrees with visual observations. A useful condition for a disk galaxy that is not edge-on to be classified as having a bulge prominence in line with AGNDISKS is  $B_{\text{avg}} \leq 0.3$ .

### 3.3 Stellar properties of the samples

Given that we need to control for SFR and stellar mass,  $M_*$ , we first need to measure these parameters, and we describe this process below. Figure 3.4 shows the SFR– $M_*$  distribution of the parent inactive sample, INACDISKS (dark blue contours), and the complete disk-dominated, AGN-host sample, AGNDISKS (red crosses). The two samples, whilst they have significant overlap in their distributions, occupy very different parameter spaces. The process for obtaining  $M_*$  is described in the Chapter 3.3.1, and the process for obtaining SFR is described in Chapter 3.3.2.

#### 3.3.1 Stellar Mass

For the INACDISKS sample, we use the median stellar mass value reported in the MPA-JHU catalogue (Kauffmann et al., 2003a; Salim et al., 2007; Brinchmann et al., 2004) for each individual galaxy. This is possible since there are no bright AGN in the galaxies in INACDISKS, so there is no need to account for the flux coming from the AGN contaminating the galaxy flux. The minimum  $M_*$  is  $\log(M_*/M_\odot) = 7.20$  and the maximum  $M_*$  is  $\log(M_*/M_\odot) = 12.06$ . The median is  $\log(M_*/M_\odot) = 9.80$ .

It is important that stellar mass is calculated in as similar way as possible for both samples. [Kauffmann et al. \(2003a\)](#) used SDSS-derived spectral indices to determine stellar masses, correcting for a number of potential biases, including for the size and partial galaxy coverage of the spectral fibre aperture. They also found a tight relation between galaxy colour and mass-to-light ratio. The colour-based  $M/L$  determination directly uses the integrated light of the whole galaxy. In addition to being generally useful for galaxies where no spectrum is available, this method is likely to be more robust to contamination from luminous AGN than the method based on fibre spectra.

We estimate  $M_*$  for the AGNDISKS sample using the colour-dependent mass-to-light ratio determinations of [Baldry et al. \(2006, Figure 5\)](#). This method requires  $u - r$  colours for the host galaxies, disentangled from the bright AGN emission. We assume that our measured  $f_{\text{psf}}$  values (Chapter 3.2.3.3) are a better measure of AGN and host galaxy flux ratios than the SDSS `psfMag` in every band, and thus apply the factor of  $(1 - f_{\text{psf}})$  to the  $u$  and  $r$  band `cModelMag` to determine galaxy  $u$  and  $r$  magnitudes. The variation in  $f_{\text{psf}}$  between the  $u$  band and  $r$  band was tested and found to be negligible. Therefore, the calculated values for  $f_{\text{psf}}$ , which were originally calculated in the  $i$  band for similarity with *HST*, are used throughout. The colour-based mass-to-light ratios are adopted for the final stellar masses for INACDISKS as well as AGNDISKS. The minimum  $M_*$  for AGNDISKS is  $\log(M_*/M_\odot) = 9.93$  and the maximum  $M_*$  for AGNDISKS is  $\log(M_*/M_\odot) = 11.19$ . The median  $M_*$  for AGNDISKS is  $\log(M_*/M_\odot) = 10.71$ .

From Figure 3.3, we can see that had we used exclusively  $f_{\text{psf}}$  from SDSS, the values for  $M_*$  would tend to be underestimated, since the fraction of the total flux assigned to the AGN would be greater than the true value, leading to a lower flux being assigned to the galaxy. Following the equations in [Baldry et al. \(2006\)](#), this would lead to a lower  $M_*$ . Our improved PSF subtraction allows us to determine stellar masses for the AGN sample that more closely match the masses determined for the inactive sample. In Chapter 3.4 we also match the stellar mass distributions between AGNDISKS and INACDISKS.

### 3.3.2 Star Formation Rate

As with  $M_*$  it is important that the methods for calculating SFR in AGNDISKS and INACDISKS are as similar as possible, whilst acknowledging that only one sample has a source of flux of contamination in the form of an AGN.

We use the formula outlined in Kennicutt et al. (1994), succinctly expressed in solar units in Pflamm-Altenburg et al. (2007, Equation 3.2) to determine the SFR of individual galaxies in AGNDISKS, where  $L_{\text{H}\alpha}$  is the  $\text{H}\alpha$  luminosity.

$$\frac{\text{SFR}}{\text{M}_{\odot} \text{yr}^{-1}} = \frac{L_{\text{H}\alpha}}{1.26 \times 10^{41} \text{ erg s}^{-1}} \quad (3.2)$$

However, this only gives the SFR within the region observed with Lick (see Figure 2.2),  $\text{SFR}_{\text{obs}}$ , and requires extrapolation to the rest of the galaxy,  $\text{SFR}_{\text{gal}}$ . We do this via simplification of the method outlined in Brinchmann et al. (2004), which assumes that SFR directly correlates with the luminosity in the  $i$ -band. We determine the  $i$ -band luminosity in the observed region,  $L_{i,\text{obs}}$ , by convolving the spectrum with the  $i$ -band filter transmission curve (Rodrigo et al., 2012; Rodrigo & Solano, 2020). We use the SDSS `cModelMag` from the MPA-JHU catalogue to calculate the  $i$ -band luminosity of the galaxy,  $L_{i,\text{gal}}$  (via use of  $f_{\text{psf}}$ ), and scale up the SFR accordingly via:

$$\text{SFR}_{\text{gal}} = \frac{L_{i,\text{gal}}}{L_{i,\text{obs}}} \text{SFR}_{\text{obs}} \quad (3.3)$$

Using SDSS flux measurements from MPA-JHU, the inactive sample is consistent with a single value of  $0.3 \pm 0.1$  for the Balmer decrement, assuming a gas temperature of  $T = 10^4 \text{ K}$ , an electron density of  $n_e = 10^2 \text{ cm}^{-2}$ , Case B recombination (Osterbrock, 1989), and a reddening curve defined in Calzetti et al. (2000). We assume that this also applies to the star-forming regions of the AGN-host galaxies, and thus apply this Balmer decrement as shown in Domínguez et al. (2013).

There are 22 sources in AGNDISKS for which we were unable to obtain values of  $\text{H}\alpha$  flux in the galaxy, and can only constrain the upper limit. This is due to no discernible signal, even after carefully removing the AGN contamination from the galaxy using the wings of the PSF, as described in Chapter 3.2.3.2. Thus, for

galaxies that have an upper limit to their H $\alpha$  flux, they only have an upper limit for their SFR.

Since the sources in INACDISKS do not host a bright AGN contaminating the emission from the galaxy, we can directly use the values in MPA-JHU for total SFR (as opposed to the SFR exclusively in the central fibre), given as MEDIAN\_SFR, which also uses the method outlined in Brinchmann et al. (2004). The minimum SFR is  $\log(\text{SFR}/M_{\odot} \text{ yr}^{-1}) = -2.40$  and the maximum SFR is  $\log(\text{SFR}/M_{\odot} \text{ yr}^{-1}) = 1.93$ . The median is  $\log(\text{SFR}/M_{\odot} \text{ yr}^{-1}) = 0.026$ .

### 3.3.2.1 Dealing with upper limits

We identify whether the 22 galaxies with no detected H $\alpha$  emission are consistent within our S/N limits with being drawn from the subsample of 34 galaxies in AGNDISKS with H $\alpha$  detections. We use a bootstrapping method to randomly sample from within the upper limits of the non-detected SFRs. Specifically, we assume the true values of SFR are uniformly distributed between the upper limit calculated, and a lower end of  $\log(\text{SFR}/M_{\odot} \text{ yr}^{-1}) = -1.5$ , where  $-1.5$  was chosen as a small, non-zero number approximately equal to the lower end of SFRs in INACDISKS. A uniform distribution is a conservative estimate, since there is no reason to assume that the true value of the SFR is closer to the upper limit than to anywhere else in the range — we have no prior information about the distribution of SFRs. We also select a random sample from the sources with H $\alpha$  detections, where the SFR was randomly drawn from a normal distribution with a mean of  $\log(\text{SFR})$  and a standard deviation of the error in  $\log(\text{SFR})$ . We re-sampled from upper limit SFRs and values of SFR using this method 100,000 times, with replacement. For each sampling, we used a KS test (Kolmogorov, 1933) to identify the probability that the two samples were drawn from the same distribution. If the SFRs of the limited subsample are statistically indistinguishable from those in the measured subsample, we would expect the KS values to follow a Normal distribution. For example, we would expect approximately 95% of tests to have  $p > 0.05$ .

Instead, the distribution of KS values from the bootstrapping is highly skewed toward more statistically significant differences. Only 0.077% of the selections and

comparisons had  $p > 0.05$ . In other words, a  $> 2\sigma$  confidence that the two samples were statistically indistinguishable only occurred 77 times out of 100,000. If the subsample with limits was indistinguishable from that without, we would expect this to occur approximately 95,000 times. Therefore the sources with SFR limits do have significantly lower SFRs than the rest of the sample, but our inability to otherwise constrain them inhibits a clean comparison with the inactive sample. Thus, for comparisons using a tightly controlled sample, we remove the sources which have only upper limits on their SFR, instead of  $H\alpha$  detections.

There are a handful of cases where a source has an upper limit on SFR that is much higher than the detected sources, for example  $\log(\text{SFR}/M_{\odot}\text{yr}^{-1}) > 2$ . These sources fall outside of the bulk of SFRs from the inactive sample, shown in the blue contours in Figure 3.4. Particularly in these cases, the noise in the spectra of the host galaxies was simply too high (likely due to the AGN), that this resulted in the summation of all of the flux that could be due to  $H\alpha$  being unplausibly high. As the KS-tests above showed, these galaxies are removed from the sample for further analysis. However, these are good candidates for follow up with the aim of obtaining higher signal-to-noise ratios, to determine if the SFR is really that high, and the galaxy is experiencing a starburst. Multiple slit angles would allow us to ensure we are not just observing a clump of particularly high star formation, and that the part we are observing is representative of the galaxy as a whole.

This gives us an AGN-host galaxy sample used for comparison, which we call AGNDISKFIN, of median redshift 0.13, containing 34 galaxies, 20 of which host a large-scale galactic bar. The fraction of this sample hosting a bar is  $f_{\text{bar,AGN}} = 0.59^{+0.08}_{-0.09}$ , where uncertainties enclose the 68% confidence limits of the binomial fraction error (Cameron, 2011). The minimum SFR is  $\log(\text{SFR}/M_{\odot}\text{yr}^{-1}) = -1.16$  and the maximum SFR is  $\log(\text{SFR}/M_{\odot}\text{yr}^{-1}) = 2.08$ . The median is  $\log(\text{SFR}/M_{\odot}\text{yr}^{-1}) = 0.56$ .

With both  $M_*$  and SFR derived from AGN-subtracted galaxy fluxes, we can examine further the star-forming properties of the sample below. We show a full table of the values in Table 3.1.

Table 3.1: The data for the AGN-host galaxies used in Chapter 3. The “Object ID” column is the J2000 number, the RA and Dec are measured in decimal degrees. The “Barred?” column is True if the galaxy is barred, and False if there is no visible bar. “HST?” indicates whether the galaxy was imaged as part of the HST snapshot program, HST-GO-14606. If the row is in italics, this is where we were only able to obtain an upper limit on the star formation rate.

Object ID	RA/°	Dec/°	Redshift	$\log(M_*/M_\odot)$	$\log(\text{SFR}/M_\odot\text{yr}^{-1})$	Barred?	HST?
<i>J000011.72+052317.5</i>	<i>0.049</i>	<i>5.388</i>	<i>0.040478</i>	<i><math>9.861 \pm 0.07</math></i>	$\leq -0.5$	<i>False</i>	<i>False</i>
J000220.23−033744.8	0.584	−3.629	0.188978	$11.194 \pm 0.011$	$1.410 \pm 0.06$	True	True
J000628.97+373229.2	1.621	37.541	0.066581	$10.582 \pm 0.004$	$0.318 \pm 0.04$	True	True
<i>J001701.79+080445.1</i>	<i>4.257</i>	<i>8.079</i>	<i>0.085658</i>	<i><math>10.436 \pm 0.007</math></i>	$\leq 1.499$	<i>False</i>	<i>True</i>
J002337.17+044222.4	5.905	4.706	0.082088	$10.742 \pm 0.008$	$0.188 \pm 0.08$	False	True
J003432.51+391836.0	8.635	39.310	0.138319	$10.363 \pm 0.012$	$0.371 \pm 0.06$	True	True
<i>J003511.48−004917.9</i>	<i>8.798</i>	<i>−0.822</i>	<i>0.186125</i>	<i><math>11.113 \pm 0.009</math></i>	$\leq 2.099$	<i>False</i>	<i>True</i>
J004719.39+144212.5	11.831	14.704	0.038990	$11.075 \pm 0.002$	$0.946 \pm 0.07$	True	False
J005607.67+254804.7	14.032	25.801	0.150256	$10.729 \pm 0.009$	$0.616 \pm 0.11$	True	True
<i>J005829.77+263914.7</i>	<i>14.624</i>	<i>26.654</i>	<i>0.172217</i>	<i><math>10.784 \pm 0.04</math></i>	$\leq 1.844$	<i>False</i>	<i>True</i>
J010707.80+440348.2	16.783	44.063	0.197483	$10.997 \pm 0.008$	$0.888 \pm 0.07$	False	True
J015503.00−050834.2	28.763	−5.143	0.131353	$11.077 \pm 0.004$	$0.540 \pm 0.08$	False	True
<i>J015546.37+071904.0</i>	<i>28.943</i>	<i>7.318</i>	<i>0.068464</i>	<i><math>10.467 \pm 0.006</math></i>	$\leq 1.537$	<i>False</i>	<i>True</i>
<i>J015555.33+040620.2</i>	<i>28.981</i>	<i>4.106</i>	<i>0.136427</i>	<i><math>10.773 \pm 0.04</math></i>	$\leq 12.133$	<i>False</i>	<i>False</i>

Continued on next page

Table 3.1: The data for the AGN-host galaxies used in Chapter 3. The “Object ID” column is the J2000 number, the RA and Dec are measured in decimal degrees. The “Barred?” column is True if the galaxy is barred, and False if there is no visible bar. “HST?” indicates whether the galaxy was imaged as part of the HST snapshot program, HST-GO-14606. If the row is in italics, this is where we were only able to obtain an upper limit on the star formation rate. (Continued)

Object ID	RA/°	Dec/°	Redshift	$\log(M_*/M_\odot)$	$\log(\text{SFR}/M_\odot\text{yr}^{-1})$	Barred?	HST?
J021028.42–110019.4	32.618	–11.005	0.176211	$10.681 \pm 0.016$	$0.793 \pm 0.11$	False	True
J021355.14–055121.3	33.478	–5.856	0.142918	$10.800 \pm 0.004$	$0.622 \pm 0.11$	True	True
<i>J023827.41+015427.7</i>	<i>39.614</i>	<i>1.908</i>	<i>0.024572</i>	<i><math>10.890 \pm 0.004</math></i>	<i><math>\leq 1.59</math></i>	<i>True</i>	<i>False</i>
J032548.59+135338.5	51.452	13.894	0.147422	$11.088 \pm 0.016$	$2.082 \pm 0.03$	False	True
<i>J044720.72–050814.0</i>	<i>71.836</i>	<i>–5.137</i>	<i>0.044416</i>	<i><math>10.851 \pm 0.014</math></i>	<i><math>\leq 1.683</math></i>	<i>False</i>	<i>False</i>
J055537.61+632825.2	88.907	63.474	0.152509	$10.706 \pm 0.015$	$0.398 \pm 0.2$	True	True
J072217.53+303050.0	110.573	30.514	0.099879	$10.435 \pm 0.006$	$–0.536 \pm 1.3$	False	True
J073126.68+452217.5	112.861	45.372	0.092342	$10.586 \pm 0.005$	$1.265 \pm 0.03$	False	True
<i>J074232.78+494835.0</i>	<i>115.637</i>	<i>49.810</i>	<i>0.021914</i>	<i><math>10.806 \pm 0.03</math></i>	<i><math>\leq 1.404</math></i>	<i>True</i>	<i>False</i>
J080559.94+260602.4	121.500	26.101	0.136000	$10.370 \pm 0.009$	$–0.173 \pm 1.8$	True	True
J081324.00+542236.9	123.350	54.377	0.042304	$10.631 \pm 0.004$	$0.325 \pm 0.07$	True	True
J082549.55+471028.1	126.456	47.174	0.132652	$11.161 \pm 0.003$	$1.325 \pm 0.06$	True	True
J090954.61+564235.4	137.478	56.710	0.111313	$10.238 \pm 0.009$	$–0.118 \pm 0.3$	True	True
<i>J091826.00+161819.6</i>	<i>139.608</i>	<i>16.305</i>	<i>0.029645</i>	<i><math>10.417 \pm 0.2</math></i>	<i><math>\leq 0.609</math></i>	<i>False</i>	<i>False</i>

Continued on next page

Table 3.1: The data for the AGN-host galaxies used in Chapter 3. The “Object ID” column is the J2000 number, the RA and Dec are measured in decimal degrees. The “Barred?” column is True if the galaxy is barred, and False if there is no visible bar. “HST?” indicates whether the galaxy was imaged as part of the HST snapshot program, HST-GO-14606. If the row is in italics, this is where we were only able to obtain an upper limit on the star formation rate. (Continued)

Object ID	RA/°	Dec/°	Redshift	$\log(M_*/M_\odot)$	$\log(\text{SFR}/M_\odot\text{yr}^{-1})$	Barred?	HST?
J103438.59+393828.2	158.661	39.641	0.043175	$10.597 \pm 0.002$	$0.963 \pm 0.016$	True	True
<i>J115326.22+355653.7</i>	<i>178.359</i>	<i>35.948</i>	<i>0.067087</i>	<i><math>10.771 \pm 0.02</math></i>	<i><math>\leq 2.222</math></i>	<i>False</i>	<i>False</i>
J140604.82+580041.6	211.520	58.012	0.126000	$10.831 \pm 0.005$	$0.511 \pm 0.12$	True	True
<i>J141611.95+631128.2</i>	<i>214.050</i>	<i>63.191</i>	<i>0.077606</i>	<i><math>10.277 \pm 0.014</math></i>	<i><math>\leq 1.144</math></i>	<i>False</i>	<i>True</i>
<i>J154212.91+250503.0</i>	<i>235.554</i>	<i>25.084</i>	<i>0.187318</i>	<i><math>10.938 \pm 0.04</math></i>	<i><math>\leq 0.708</math></i>	<i>True</i>	<i>False</i>
<i>J192250.62+350147.4</i>	<i>239.790</i>	<i>35.030</i>	<i>0.031000</i>	<i><math>10.698 \pm 0.03</math></i>	<i><math>\leq 0.780</math></i>	<i>True</i>	<i>False</i>
<i>J160732.86+484620.1</i>	<i>241.887</i>	<i>48.772</i>	<i>0.149515</i>	<i><math>11.150 \pm 0.0012</math></i>	<i><math>\leq 2.021</math></i>	<i>False</i>	<i>True</i>
J160808.28+350150.7	242.028	42.683	0.084000	$10.976 \pm 0.003$	$1.132 \pm 0.07$	True	True
J161658.69+230755.4	244.245	23.132	0.100178	$10.685 \pm 0.009$	$1.319 \pm 0.05$	True	True
<i>J162723.13+573512.4</i>	<i>246.846</i>	<i>57.587</i>	<i>0.066561</i>	<i><math>10.381 \pm 0.004</math></i>	<i><math>\leq 0.933</math></i>	<i>False</i>	<i>True</i>
J170534.94+334011.7	256.396	33.670	0.126461	$10.866 \pm 0.009$	$0.281 \pm 0.17$	True	True
J171601.93+311213.9	259.008	31.204	0.110886	$10.652 \pm 0.006$	$1.575 \pm 0.06$	False	True
J174209.25+510105.6	265.539	51.018	0.064349	$10.446 \pm 0.007$	$0.985 \pm 0.13$	True	True
J174815.32+582335.2	267.064	58.393	0.054150	$10.205 \pm 0.004$	$-1.160 \pm 1.2$	False	True

Continued on next page

Table 3.1: The data for the AGN-host galaxies used in Chapter 3. The “Object ID” column is the J2000 number, the RA and Dec are measured in decimal degrees. The “Barred?” column is True if the galaxy is barred, and False if there is no visible bar. “HST?” indicates whether the galaxy was imaged as part of the HST snapshot program, HST-GO-14606. If the row is in italics, this is where we were only able to obtain an upper limit on the star formation rate. (Continued)

Object ID	RA/°	Dec/°	Redshift	$\log(M_*/M_\odot)$	$\log(\text{SFR}/M_\odot\text{yr}^{-1})$	Barred?	HST?
J192250.75–055259.1	290.711	–5.883	0.162897	$10.576 \pm 0.010$	$0.233 \pm 0.11$	False	True
<i>J200830.89+002133.5</i>	<i>302.129</i>	<i>0.359</i>	<i>0.059790</i>	<i><math>9.850 \pm 0.06</math></i>	<i><math>\leq 1.299</math></i>	<i>True</i>	<i>False</i>
J203439.25+143411.5	308.664	14.570	0.124753	$10.812 \pm 0.004$	$0.560 \pm 0.07$	False	True
<i>J221542.29–003609.6</i>	<i>333.926</i>	<i>–0.603</i>	<i>0.099657</i>	<i><math>10.719 \pm 0.005</math></i>	<i><math>\leq 1.889</math></i>	<i>False</i>	<i>True</i>
<i>J223019.64+163112.6</i>	<i>337.582</i>	<i>16.520</i>	<i>0.084290</i>	<i><math>10.082 \pm 0.12</math></i>	<i><math>\leq 0.375</math></i>	<i>False</i>	<i>False</i>
J223954.42+272433.4	339.977	27.409	0.064653	$9.926 \pm 0.009$	$–0.610 \pm 0.4$	False	True
J224458.18–182249.2	341.242	–18.380	0.198280	$10.667 \pm 0.014$	$0.439 \pm 0.3$	False	True
<i>J225801.93–021944.8</i>	<i>344.508</i>	<i>–2.329</i>	<i>0.080105</i>	<i><math>11.148 \pm 0.003</math></i>	<i><math>\leq 1.046</math></i>	<i>False</i>	<i>False</i>
J230443.59+121210.2	346.182	12.203	0.133684	$10.836 \pm 0.013$	$0.349 \pm 0.12$	True	True
<i>J230851.26–181055.5</i>	<i>347.214</i>	<i>–18.182</i>	<i>0.129787</i>	<i><math>10.874 \pm 0.004</math></i>	<i><math>\leq 1.875</math></i>	<i>True</i>	<i>True</i>
J235258.03+032017.8	358.242	3.338	0.086038	$10.767 \pm 0.004$	$0.849 \pm 0.07$	True	True
J235632.92–040400.1	359.137	–4.067	0.229062	$10.723 \pm 0.010$	$1.100 \pm 0.09$	False	True
J235827.82+205758.6	359.616	20.966	0.057648	$10.823 \pm 0.005$	$0.824 \pm 0.08$	True	True
<i>J235845.59+323115.3</i>	<i>359.690</i>	<i>32.521</i>	<i>0.238091</i>	<i><math>10.961 \pm 0.013</math></i>	<i><math>\leq 2.348</math></i>	<i>True</i>	<i>True</i>

### 3.4 Star Formation in Merger-Free AGN hosts

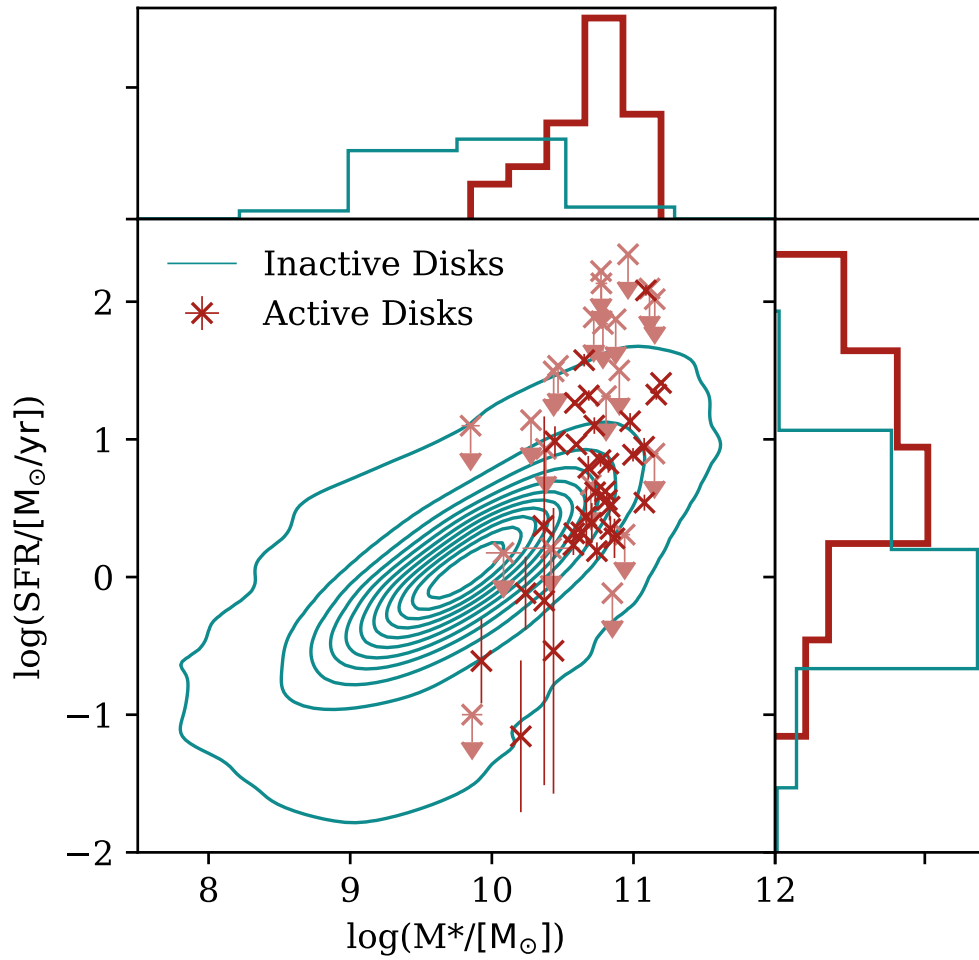
In order to examine SFRs in both the AGN-host and inactive galaxy samples, we must first control for differences in stellar mass. Figure 3.4 shows that whilst there is considerable overlap in the two samples in their stellar mass distributions, the distributions remain noticeably different — for active galaxies the distribution is narrower than for inactive galaxies, with the average active galaxy’s  $M_*$  lying above the median  $M_*$  of inactive galaxies. This pattern remains upon the removal of the galaxies with only upper limits on their star formation rate.

The difference in  $M_*$  between the two samples is most likely due to selection effects rather than an intrinsic difference. AGNDISKS is selected as a sample to host only the most luminous AGN. If we assume that the sample is not as a whole exceeding the Eddington limit, this means that there is a lower limit on black hole mass,  $M_{\text{BH}}$ . It is broadly understood that there is some form of co-evolution between galaxies and SMBHs (*e.g.*, Kormendy & Ho, 2013), even if we continue as a field to debate the details. Thus a lower limit on  $M_{\text{BH}}$  implies a lower limit on  $M_*$ , and the sample is therefore self-limiting regarding  $M_*$  (for a deeper exploration of this selection bias, see Aird et al., 2012).

The other way that AGNDISKS self-limits in  $M_*$  is that the sample is selected to consist of strongly disk-dominated galaxies. The galaxies were identified using SDSS, where the PSF width may be a substantial fraction of a galaxy’s extent. If a low-mass disk-dominated galaxy hosted a very luminous AGN, the AGN would outshine the galaxy and the disk would be difficult or impossible to identify in SDSS imagery at the redshifts of this sample. Such a galaxy would not be included in AGNDISKS. Therefore there is a lower limit on disk radius, which implies a lower limit on  $M_*$ .

These two selection effects mean we have very few AGN hosted in galaxies with  $M_* < 10^{10} M_\odot$  in our sample, and hence we must select galaxies from INACDISKS which have the same  $M_*$  distribution before comparing SFRs between the samples.

We control for  $M_*$  by weighting the inactive sample in six bins of equal width. This  $M_*$ -matched subset of inactive disk galaxies is hereafter called the INACDISKMATCH sample, and its  $M_*$  distribution is shown in the upper plot of



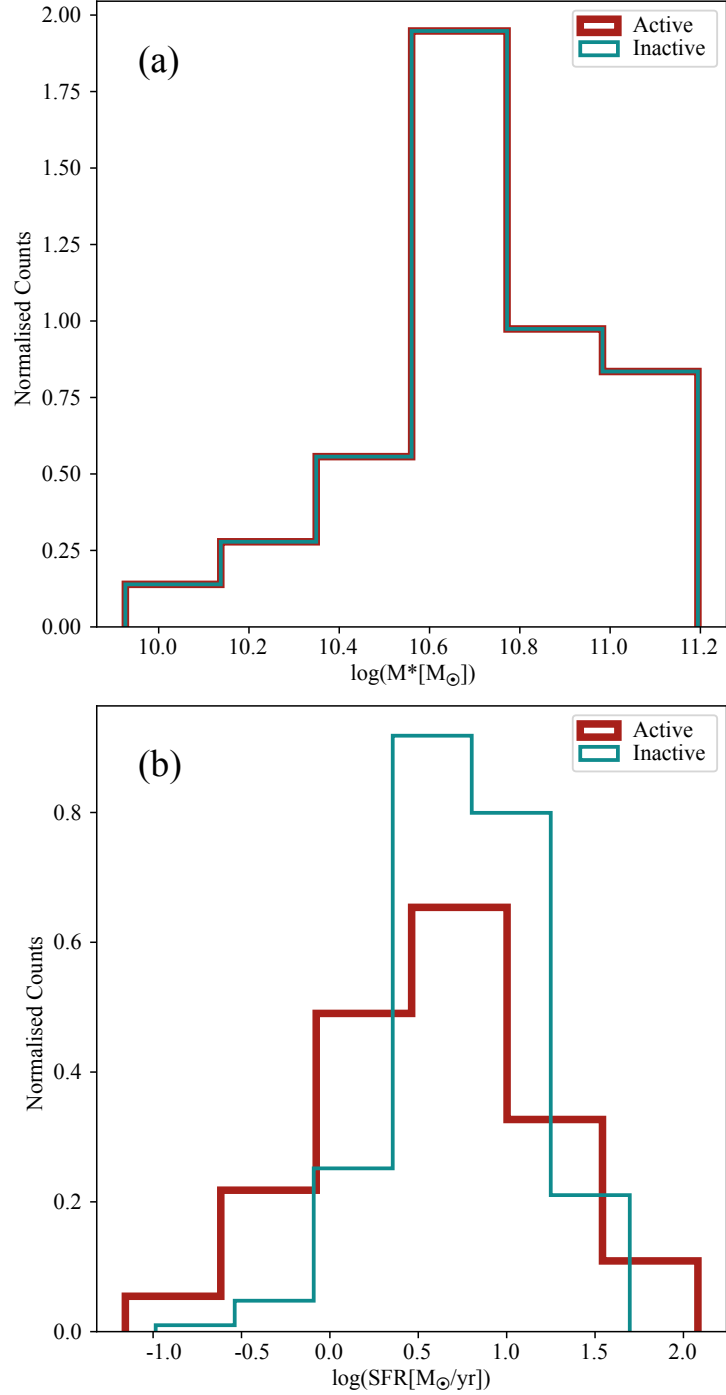
**Figure 3.4:** SFR against  $M_*$ , for both the active sample, AGNDISKS (red crosses) and the inactive disk-dominated sample, INACDISKS (teal contours). Upper limits for SFR in the active sample are shown as arrows and in a slighter paler red than those with values. Normalised histograms are shown on the top and right axes, with the thick red line corresponding to AGNDISKS and the thin blue line to INACDISKS. the values for individual galaxies are shown in Table 3.1.

Figure 3.5, for comparison with AGNDISKFIN. After performing a KS test on AGNDISKFIN’s and INACDISKS’s  $M_*$  to confirm their similarity, we obtain a  $p$ -value of  $p_{mass} = 1.000$ , which demonstrates that AGNDISKFIN and INACDISKMATCH are consistent with being drawn from the same parent sample.<sup>1</sup> The distribution of SFRs for the  $M_*$ -matched AGNDISKFIN and INACDISKMATCH samples are shown in the lower plot of Figure 3.5. The slight visual differences between the distributions do not appear to be statistically significant (from a KS-test,  $p_{SFR} = 0.368$ , a significance of  $0.9\sigma$ ). Thus we cannot rule out the null hypothesis that the SFRs of these disk-dominated galaxies hosting luminous Type 1 AGN are drawn from the same parent population as a sample of disk-dominated galaxies *not* hosting AGN. Our qualitative results do not change if we instead draw  $M_*$ -matched sub-samples instead of weighting the respective distributions.

While a lack of statistically significant differences in the SFRs of these sub-samples may be due to our relatively small sample sizes, we might expect such a result even with a larger sample, due to the complex physical processes at play. For example, AGN outflows may both quench and enhance star formation in a host galaxy (see Harrison 2017 for a review). A high fraction of our AGN-host sample shows signs of outflows (Smethurst et al., 2019, 2021), and these galaxies do not congregate in a specific region of SFR– $M_*$  space (Figure 3.4), consistent with expectations. Differing timescales also complicate interpretation of our results: the duration over which an AGN is active in a galaxy may be considerably shorter than the effects of AGN-driven quenching (Schawinski et al., 2015), which would further dilute differences between SFR in the AGN-host and inactive disk galaxy population. Better constraints on population differences between disk-dominated AGN-host and inactive galaxies will require a larger sample, ideally with spatially-resolved spectral information to more robustly trace the effect of AGN feedback.

---

<sup>1</sup>All reported  $p$ -values for KS tests between weighted distributions are estimated using sample weights instead of raw object counts.



**Figure 3.5:** Distribution of  $M_*$  (top) and SFR (bottom) after controlling for  $M_*$ , with AGN-host galaxies shown in thick red lines and inactive galaxies shown in thin blue lines. The  $M_*$  distribution demonstrates that we have successfully controlled for  $M_*$ , and has a  $p$ -value from a KS test of 1.000, showing the samples are consistent with being drawn from the same parent sample. The SFR histogram also shows the similarity between the two samples after controlling for  $M_*$ , and with a  $p$ -value of 0.368, the SFRs are consistent with being drawn from the same parent sample.

### 3.5 Bar Fractions of AGN-host vs Inactive disks

In order to isolate the possible effect of large-scale, galactic bars, we first need to ensure that all other variables which are known to correlate with bar fraction are negated via careful weighting in  $M_*$  and SFR to obtain a comparison sample.

We use the star-forming sequence shown in Figure 3.4 to ensure that both the active and inactive samples are consistent with each other in their  $M_*$  and SFR, an additional control compared to Chapter 3.4, where we only control for  $M_*$ . As with  $M_*$ , there is significant overlap in SFR between the two samples. Whilst the SFR for active galaxies seems to cover approximately the same range as that for inactive galaxies, when we only control for  $M_*$  the samples still differ enough in SFR that we need to control for SFR in order to analyse the bar fraction. The medians of the active and inactive sample respectively are  $\log(\text{SFR}_{\text{AGN}}/\text{M}_{\odot}\text{yr}^{-1}) = 0.59$  and  $\log(\text{SFR}_{\text{inactive}}/\text{M}_{\odot}\text{yr}^{-1}) = 0.72$ , and the ranges are  $-1.16 \leq \log(\text{SFR}_{\text{AGN}}/\text{M}_{\odot}\text{yr}^{-1}) \leq 2.18$  and  $-0.62 \leq \log(\text{SFR}_{\text{inactive}}/\text{M}_{\odot}\text{yr}^{-1}) \leq 1.69$ . Given that the two samples have different distributions, it is vital that we control for SFR as well as  $M_*$ , in order to truly isolate the effect of the bar.

We divide the  $M_*$  and SFR each into six bins, and assign weights to each galaxy in INACDISKS, such that the weighted sample (which we hereafter call INACDISKMATCH) has  $M_*$  and SFR distributions matching those of AGNDISKFIN. This gives a weighted bar fraction for INACDISKMATCH of  $f_{\text{bar,Inac}} = 0.44^{+0.08}_{-0.09}$ , where uncertainties arise from the binomial fraction error (Cameron, 2011).

We show the distributions of the control samples, split by active/inactive and by barred/non-barred, with  $M_*$  in the upper plot of Figure 3.6, and SFR in the lower plot. As expected, the distributions cover a much more similar range than in Figure 3.4. We confirm via KS tests on AGNDISKFIN and INACDISKMATCH that their  $M_*$  and SFR distributions are consistent with being drawn from the same parent sample.

We also use KS tests to compare both the SFR and the  $M_*$  for different subsets of the comparison samples — active galaxies, inactive galaxies, barred galaxies and non-barred galaxies. Table 3.2 shows the  $p$ -values that result from

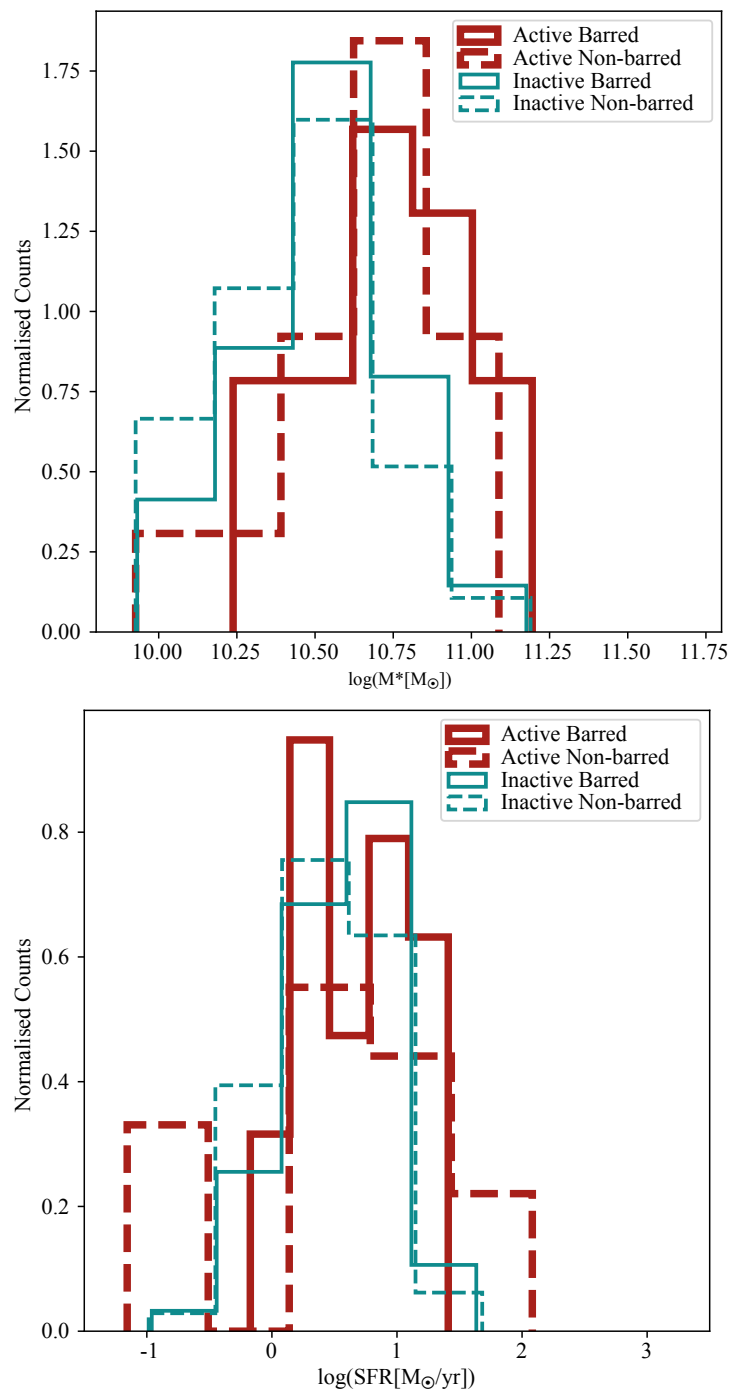


**Figure 3.6:** Distributions of  $M_*$  (top panel) and SFR (bottom panel), after controlling for both of these parameters, split by active (red, thick line) and inactive (thin blue line) galaxies, and by barred (solid line) and non-barred (dashed) lines. The results of KS tests between each pair of samples are shown in Table 3.2, but all the samples are consistent with being drawn from the same parent sample in both  $M_*$  and SFR.

**Table 3.2:** KS test  $p$ -values from the comparisons described in Chapters 3.4 and 3.5. These values are all indicative of statistically indistinguishable samples. Bold values indicate where we intentionally control for the samples to be statistically indistinguishable.

Samples being compared	$p_{\text{mass}}$	$p_{\text{SFR}}$
Controlling only for stellar mass		
AGNDISKFIN (34), INACDISKMATCH (34)	<b>1.000</b>	0.368
AGN Bar (20), AGN Non-bar (14)	0.814	0.648
Inac Bar (15), Inac Non-bar (19)	1.000	1.000
AGN Bar (20), Inac Bar (15)	1.000	0.554
AGN Non-bar (14), Inac Non-bar (19)	1.000	0.710
Controlling for stellar mass and SFR		
AGNDISKFIN (34), INACDISKMATCH (34)	<b>1.000</b>	<b>1.000</b>
AGN Bar (20), AGN Non-bar (14)	0.814	0.648
Inac Bar (15), Inac Non-bar (19)	1.000	0.977
AGN Bar (20), Inac Bar (15)	1.000	0.984
AGN Non-bar (14), Inac Non-bar (19)	0.999	0.955

the comparison samples in the first column. Values for the inactive subsamples are the weighted numbers.

Looking at the bar fractions ( $f_{\text{bar,AGN}} = 0.59_{-0.09}^{+0.08}$  for AGNDISKFIN and  $f_{\text{bar,Inac}} = 0.44_{-0.09}^{+0.08}$  for INACDISKMATCH), we can see that after controlling for the SFR and  $M_*$ , the sources in INACDISKMATCH are marginally less likely ( $\sim 1.7\sigma$ ) to host a bar than the sources in AGNDISKFIN, in agreement with studies such as [Alonso et al. \(2013\)](#) and [Galloway et al. \(2015\)](#). However it is worth noting that the samples used by [Galloway et al. \(2015\)](#) contain  $\sim 10^5$  galaxies and this work contains  $\sim 10^2$  galaxies, yet both studies obtain a similar level of significance in their results. This could potentially be due to the fact that we are looking at galaxies with little-to-no bulge component, so any bars we have are likely to be younger than in [Galloway et al. \(2015\)](#) where they make no distinction on bulge component, and thus we do not require such a large sample to obtain a similarly significant result. Our sample also considers only the highest luminosity AGN, whereas again, [Galloway et al. \(2015\)](#) impose no such limit on their sample.

We can use the  $p$ -values from the KS tests shown in the second section of Table

3.2 to test the null hypothesis that two samples are drawn from the same parent distribution. The first line, comparing AGNDISKFIN to INACDISKMATCH before controlling for SFR shows that overall the comparison samples are consistent with being drawn from the same parent sample. This is a simple check to confirm we have controlled for the various parameters correctly. From here, we divide each sample into barred and non-barred subsamples in order to draw comparisons.

For any  $M_*$ - and SFR-matched sub-samples we examine, we cannot rule out the null hypothesis that the two samples are drawn from the same parent distribution. Several potential insights emerge from this overall result. Firstly, within our samples, a bar does not necessarily have to be present to form an AGN, but if there is a bar there, then it has no unique further effect on the SFR and  $M_*$ . Given that our AGN sample has a mass range of  $9.93 \leq \log(M_*/M_\odot) \leq 11.19$ , and we selected our inactive sample to match, this is not a particularly surprising result. We have a small mass range due to our sample self-selecting for high-mass galaxies (see Section 3.4), and we select our inactive sample to match. Combined with our small sample size of 34 AGN, we would not expect a major difference in the stellar mass or SFR. However, this does also indicate that the combination of both a bar and an AGN will not necessarily drive a galaxy to a higher stellar mass than simply having a bar or an AGN. Further investigation into the gas content could shine a light on this result. It is worth noting that this does not contradict the current understanding that barred galaxies are generally observed more frequently in massive and redder systems than unbarred galaxies (Cameron et al., 2010; Masters et al., 2011; Skibba et al., 2012; Aird et al., 2012; Kruk et al., 2018; Géron et al., 2021). Secondly, the bar has no effect on SFR or  $M_*$  in this SFR– $M_*$  regime. Lastly, barred AGN-host galaxies are not a special subset of inactive barred galaxies, and this is mirrored by the comparison of active non-barred galaxies versus inactive non-barred galaxies, which also has  $p$ -values of SFR and  $M_*$  close to 1, *i.e.*, far short of any reasonable threshold for statistically significant differences. This is much the same as results from works in the last few decades (*e.g.*, Ho et al., 1997; Mulchaey & Regan, 1997; Knapen et al., 2000; Martini et al., 2003). We would note that our results do not qualitatively change if instead we only consider strong bars in both samples (*i.e.*, excluding

weak bars in the AGN-host sample and using a threshold of  $p_{\text{bar}} \geq 0.5$  for the inactive sample to select strong bars, as described in Chapter 3.2.4).

It is worth noting that whilst these results indicate solutions, our sample of AGN hosts being used to quantitatively compare is simply too small to draw conclusions with much statistical power. This is because these are the very brightest AGN in the most unambiguously disk-dominated host galaxies, rather than a sample taken over the entire AGN population in all merger-free hosts. A significant portion of our sample has only upper limits on their SFR, further constraining the sample size. Our analysis of those limits (Chapter 3.3.2.1) hints that higher signal-to-noise spectra permitting robust measurements of this subsample could provide further insight into our current results. Integral field spectroscopy for a large fraction of our sample would enable us to probe these galaxies in further detail, as would increasing the sample size by adding Vera Rubin Observatory’s LSST survey (Ivezić et al., 2019), or getting more galaxies with *Euclid* or Roman. Since we are looking at a rare phenomenon (luminous AGN), in a rare subset of galaxies (bulgeless or nearly so), it really is important that we have a large volume so as to control for confounding variables and achieve statistically robust sample numbers. It is also crucial to remember that not all AGN are this luminous, this is a particular subset of AGN, and it was collected in such a way so as to show the possibilities of extreme conditions, and further data on less luminous AGN is needed to draw conclusions over the entire population.

## 3.6 Conclusions

We have used a sample of unambiguously disk-dominated galaxies hosting luminous, Type 1 AGN in order to isolate SMBH growth through merger-free processes. We obtained longslit Lick spectroscopic data of the sample, and *HST* images of part of the sample. This allowed us to measure robust SFRs and stellar masses for 34 galaxies — the rest of the sample has only upper limits on their SFR. We compared this sample to a sample of inactive, disk-dominated galaxies with morphological classifications from Galaxy Zoo 2, and SFRs and  $M_*$  from

MPA-JHU. We performed KS tests on subsets of these samples, and we here summarise our findings:

- Galaxies hosting an AGN have a wider range of SFR than galaxies lacking an AGN, with the SFR peaking at a slightly higher value.
- After controlling for SFR and  $M_*$ , bars are marginally more likely to reside in AGN-host galaxies than galaxies not hosting AGN, ( $f_{\text{bar}} = 0.59_{-0.09}^{+0.08}$  for AGNDISKFIN and  $f_{\text{bar}} = 0.44_{-0.09}^{+0.08}$  for INACDISKMATCH) — there is a  $\sim 1.7\sigma$  difference.
- Despite the fact that bars are more likely to reside in massive galaxies, and AGN are more likely to reside in massive galaxies, having both a bar and an AGN is not associated with a further increase in a galaxy’s stellar mass beyond only having one of either a bar or an AGN.

Further work is needed to obtain higher resolution spectra for those galaxies where the flux from the disk is so overpowered by the flux of the AGN that we can only obtain upper limits of their SFR. This will allow for better separation of the AGN and the galaxy, which will result in a higher signal-to-noise ratio, and allow us to constrain SFRs further.

Upcoming surveys such as LSST and *Euclid* will facilitate breakthroughs in the field due to their increased resolution and sky coverage, which will allow us to obtain larger samples of merger-free AGN-host galaxies for improved statistical analysis. With today’s facilities and scientific ability, it is interesting to see that despite probing the extremes of black hole growth in the merger-free regime, for those galaxies where we can obtain SFR, they do not appear to be outliers compared to galaxies not hosting AGN.

# Chapter 4

## Galaxy Zoo DESI: large-scale bars as a secular mechanism for triggering AGN

### Abstract

Despite the evidence that supermassive black holes (SMBHs) co-evolve with their host galaxy, and that most of the growth of these SMBHs occurs via merger-free processes, the underlying mechanisms which drive this secular co-evolution are poorly understood. We investigate the role that both strong and weak large-scale galactic bars play in mediating this relationship. Using 72,940 disk galaxies in a volume-limited sample from Galaxy Zoo DESI, we analyse the active galactic nucleus (AGN) fraction in strongly barred, weakly barred, and unbarred galaxies up to  $z = 0.1$  over a range of stellar masses and colours. After controlling for stellar mass and colour, we find that the optically selected AGN fraction is  $31.6 \pm 0.9\%$  in strongly barred galaxies,  $23.3 \pm 0.8\%$  in weakly barred galaxies, and  $14.2 \pm 0.6\%$  in unbarred disk galaxies. These are highly statistically robust results, strengthening the tantalising results in earlier works. Strongly barred galaxies have a higher fraction of AGN than weakly barred galaxies, which in

turn have a higher fraction than unbarred galaxies. Thus, while bars are not required in order to grow a SMBH in a disk galaxy, large-scale galactic bars appear to facilitate AGN fuelling, and the presence of a strong bar makes a disk galaxy more than twice as likely to host an AGN than an unbarred galaxy at all galaxy stellar masses and colours.

## 4.1 Introduction

Supermassive black holes (SMBHs) reside in the centre of the majority of galaxies, gaining most of their mass during active phases, where the accretion systems are known as active galactic nuclei (AGN). Yet what triggers the “switch on” of an AGN is equivocal. This question is critical to understanding the interplay between AGN and their host galaxies, including the effectiveness of AGN feedback and SMBH–galaxy co-evolution (see *e.g.*, [Kormendy & Ho, 2013](#); [Heckman & Best, 2014](#), for a review).

Recent simulation studies have shown that the majority of SMBH growth occurs via secular (merger-free) mechanisms ([Martin et al., 2018](#); [McAlpine et al., 2020](#); [Smethurst et al., 2024](#)), meaning that mergers are not the primary drivers of the relationships known to exist between SMBHs and their host galaxies. Disk-dominated, bulgeless galaxies have had a history free from major mergers (1:10 mass ratio) since at least  $z \sim 2$  ([Martig et al., 2012](#)), and so by exclusively looking at a population of disk-dominated, bulgeless galaxies and the kiloparsec-scale structures within them (such as large-scale galactic bars), we can gain a better understanding of AGN triggering in the absence of major mergers. The bulge present in some disk-dominated galaxies could be merger-formed, but it could also be formed through a number of other mechanisms, including minor mergers, and potentially bars. By looking at a population of disk-dominated galaxies as a whole, we can investigate structures such as bars across the entire disk-dominated galaxy population.

Large-scale strong bars are observed at optical wavelengths in the Sloan Digital Sky Survey (SDSS; [York et al., 2000](#)) in  $29.4 \pm 0.5\%$  of disk galaxies at redshift  $0.01 < z < 0.06$  ([Masters et al., 2011](#)), and when using either a deeper optical

survey or one with better seeing, such as DECaLS, this increases to around 45% when combining galaxies with either weak or strong bars (Géron et al., 2021). This distinction between strong and weak bars is important, despite their being on a continuum, since work has shown that they may have different formation mechanisms (*e.g.*, Géron et al., 2023), although separating out strong and weak bars consistently poses a challenge. In general, a bar is classified as strong if it dominates the galaxy flux, and weak as containing a smaller fraction of the total flux (Nair & Abraham, 2010). These bars can cause transfers of a disk’s angular momentum, leading to gas being transported down to the central kiloparsec region (Friedli & Benz, 1993; Athanassoula, 2003), where it could be accreted onto a black hole. Thus, by tracing these kiloparsec-scale structures, we can gain insight into the dynamics within a galaxy that facilitate the transfer of angular momentum, and hence the fuelling which gives rise to the AGN characteristics that we observe.

Simulations have shown that it is physically possible for bars to provide the necessary inflow of gas to match the accretion rates we see in AGN (Sakamoto, 1996; Maciejewski et al., 2002; Regan & Teuben, 2004; Lin et al., 2013), and this is mirrored in observational work by Smethurst et al. (2021). Several other studies have pointed to either an increase in the bar fraction of AGN hosts compared to inactive galaxies, or an increase in AGN fraction in barred galaxies compared to unbarred (Knapen et al., 2000; Laine et al., 2002; Coelho & Gadotti, 2011; Oh et al., 2012; Galloway et al., 2015; Alonso et al., 2018; Silva-Lima et al., 2022; Garland et al., 2023). However, many of these previous studies have suffered from low statistical significance or sensitivity to methodology and selection effects.

There are also a number of studies finding no correlation (*e.g.*, Cheung et al., 2013; Goulding et al., 2017). Thus, in this work, we aim to revisit this correlation between large-scale bars and AGN, using Galaxy Zoo DESI (Walmsley et al., 2023a) to obtain robust morphologies from deeper imaging, and observed emission lines from SDSS MPA-JHU DR7<sup>1</sup> to determine the activity category of the systems in our sample.

Chapter 4.2 discusses our sample selection and classification. We present our results in Chapter 4.3, followed by our discussions and conclusions in Chapters

---

<sup>1</sup>Available at <https://www.mpa-garching.mpg.de/SDSS/DR7/>

4.4 and 4.5. Throughout this work, we consider AGN and LINERs (low-ionisation nuclear emission line regions) to be two distinct categories, rather than LINERs being a subset of AGN. We use WMAP9 cosmology (Hinshaw et al., 2013), incorporated via `Astropy`, where we assume a flat universe,  $H_0 = 69.3 \text{ km s}^{-1} \text{ Mpc}^{-1}$  and  $\Omega_m = 0.287$ .

## 4.2 Data Collation

In the subsections below, we describe the use of multiple surveys to obtain the data required for this study. We collate a sample of disk-dominated galaxies (divided into strongly barred, weakly barred and unbarred) which are either AGN hosts, star-forming, or undetermined.

### 4.2.1 Sample Selection

Galaxy Zoo DESI (GZD; Walmsley et al., 2023a) uses machine learning to identify the morphology of 8.7M galaxies in the DESI Legacy Imaging Surveys: DECaLS, MzLS and BASS, plus DES. Given the improved seeing on DESI compared to SDSS, we can push reliable morphology classifications to higher redshifts. Full details of the methodology can be found in the release paper, and we summarise briefly here.

Given the size of the DESI Legacy Imaging Surveys, it was not feasible to collect morphological classifications from volunteers alone (such as in Galaxy Zoo 2), as this would take around 200 years at current classification rates. Thus more efficient techniques are required. Walmsley et al. (2023a) trained deep learning models (Walmsley et al., 2023b) on 10M Galaxy Zoo volunteer votes over 401k galaxies from both GZ:DECaLS and the DESI Legacy Surveys to classify galaxy morphology based on this training data. Their models can typically predict what fraction of volunteers would give a particular answer to each question to within a mean vote fraction error of 10%. See Section 1.1.3.2 for a more detailed description of GZD.

We match GZD within a 3" radius to the MPA-JHU SDSS DR7 catalogue (to obtain stellar masses,  $M_*$ , colours and emission line fluxes; Kauffmann et al.,

2003c; Salim et al., 2007) and NYU-VAGC (New York University Value Added Galaxy Catalogue) (to obtain  $k$ -corrections; Blanton et al., 2005), resulting in 793,824 galaxies. Figure 4.1 shows absolute  $r$ -band magnitude,  $M_r$  versus redshift for the entire sample, as well as the volume-limited disk galaxy sample (described in Section 4.2.2).

### 4.2.2 Morphology Classification

In order to examine the secular growth, we select galaxies which have a substantial disk component using GZD. The first classification the model must perform is to select whether the galaxy is “smooth and featureless”, has “features or a disk”, or contains (or is) an “artefact”. To select disk galaxies, we require that the vote fraction for “features or disk” is  $f_{\text{smooth-or-featured.featured-or-disk}} \geq 0.27$ .

We also require that any disks must not be edge-on so that a bar can be identified if present, since in an edge-on galaxy, the bar can be obscured. GZD must categorise each featured galaxy as “edge-on” or “not edge-on”, and for our purposes, we require  $f_{\text{disk-edge-on.no}} \geq 0.68$ . Galloway et al. (2015) examine the relationship between inclination angle and observed bar fraction, and show (their Figure 2) that the exact threshold used for “not edge-on” does not have a significant effect. Our limits follow those used in G eron et al. (2021) and Walmsley et al. (2022).

To complete our sample, we require that the galaxy in the image does not appear to be merging with another galaxy. GZD classifies every image with a merger class of “merger”, “major disturbance”, “minor disturbance”, or “none”. We consider galaxies with any significant level of disturbance to be potential contaminants to a sample of disks undergoing secular evolution. Thus we create a parameter we refer to as merger prominence,  $\zeta_{\text{avg}}$ , analogous to the bulge prominence parameter in Masters et al. (2019). We define  $\zeta_{\text{avg}}$  as:

$$\begin{aligned} \zeta_{\text{avg}} = & 0.2 \times f_{\text{merging\_minor-disturbance}} \\ & + 0.8 \times f_{\text{merging\_major-disturbance}} \\ & + f_{\text{merging\_merger}} \end{aligned} \tag{4.1}$$

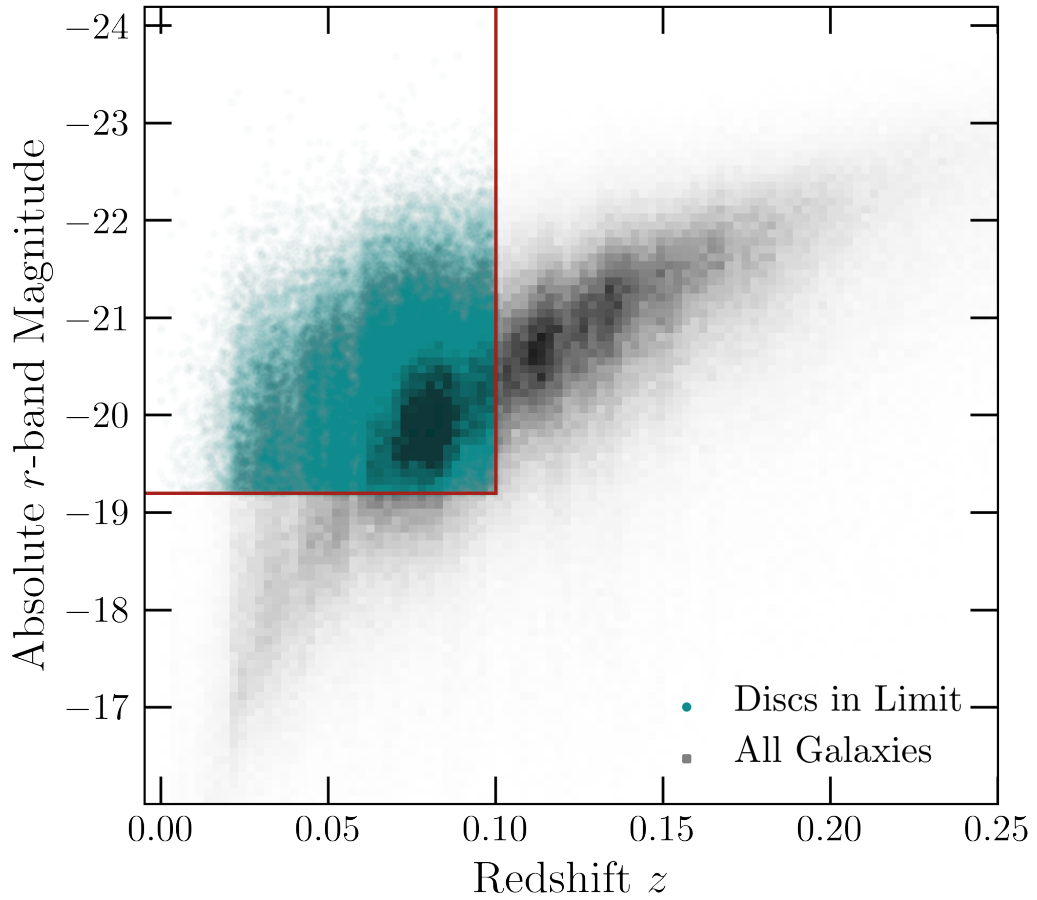


**Figure 4.1:** Absolute  $r$ -band magnitude against redshift, showing our volume limited sample. The grey-scale 2D histogram represents all galaxies in GZ DESI, and the teal points represent disk-dominated, not edge-on, merger-free galaxies within our volume limit. These teal points make up our full sample. The red lines at  $M_r = -19.2$  and  $z = 0.10$  delineate our redshift and  $r$ -band magnitude limits.

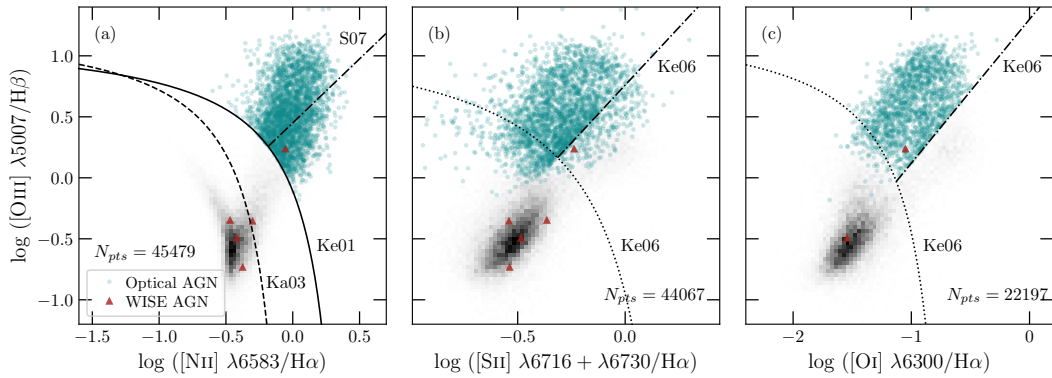


**Figure 4.2:** Classification of disk-dominated sources on a trio of emission line ratio diagrams (Baldwin et al., 1981; Veilleux & Osterbrock, 1987). The grey histogram represents anything classified as ‘star-forming’, ‘LINER’ or ‘composite’, the teal points represent optically classified AGN and the red triangles represent WISE-classified AGN. From Panel (a), we assume that any source falling below the Ka03 line (Kauffmann et al., 2003c) is purely star-forming. Anything above the Ke01 line (Kewley et al., 2001) is either an AGN or a LINER, and thus any source lying between those two lines is classified as composite. To distinguish between AGN and LINERs, we use Panels (c), then (b), then (a) in that order. This is because where a source has  $S/N > 3$  in [OI], then Panel (c) is the most reliable, and we consider any source lying above the Ke06 (Kewley et al., 2006) line to be an AGN, whereas a source below is a LINER. Where a source has  $S/N < 3$  in [OI],  $S/N > 3$  in [SII], we use Panel (b). Again, a source lying above the Ke06 line is classified as an AGN and below is a LINER. Where both [SII] and [OI] in a source have  $S/N < 3$ , we use [NII]. Any source lying above the S07 line (Schawinski et al., 2007) is classified an AGN, and below is a LINER.

We require our sample to contain only galaxies which are not merging, which we identify as  $\zeta_{\text{avg}} < 0.3$ . This value has been visually checked to be consistent with undisturbed galaxies.

In order to reduce selection effects, we select a volume-limited sample having  $z \leq 0.10$  and  $M_r \leq -19.2$ , as shown in Figure 4.1. The 48,871 galaxies that form our final, complete sample (*i.e.*, within the volume limit, disk-dominated, not edge-on, not merging) are shown in teal.

Within this volume-limited sample, we subsequently identify whether each of our galaxies has a bar, and the strength of that bar. GZD asks the models to distinguish between “strongly barred”, “weakly barred”, and “not barred”. We classify a galaxy as unbarred if  $f_{\text{strong-bar}} + f_{\text{weak-bar}} < 0.5$ . We then divide the barred galaxies into strong and weak bars in order to investigate the effect of bar strength on AGN presence. We define a barred galaxy as strongly barred if  $f_{\text{strong-bar}} \geq f_{\text{weak-bar}}$ , and weakly barred if  $f_{\text{strong-bar}} < f_{\text{weak-bar}}$ . These limits follow the criteria used successfully in Geron et al. (2021, 2023). This means that every galaxy in our volume-limited disk sample is categorised as unbarred (UBAR, 27,391 galaxies), strongly barred (SBAR, 7,069 galaxies) or weakly barred (WBAR, 14,411 galaxies).

As with any measurement, the GZD vote fractions do have errors associated with them. When the vote fractions are varied within their errors (assumed to be Gaussian) using a bootstrapping method iterated 1000 times with replacements, our results do not change.

### 4.2.3 Activity Classification

We use emission line ratio diagrams (Baldwin, Phillips & Terlevich, 1981; Veilleux & Osterbrock, 1987) to classify the galaxies in our sample as either: undetermined, uncertain, star-forming, composite, AGN, or LINER. We use the emission lines from MPA-JHU DR7 to place galaxies on the diagrams, and we show the distribution in Figure 4.2.

In order for a source to be classifiable according to this method, we require that the signal-to-noise ratio (S/N) in [OIII], H $\beta$ , [NII] and H $\alpha$  be  $S/N \geq 3$ , in order to ensure good quality emission lines. If a galaxy does not fulfil this

first requirement, it may still be classifiable depending on where the limits lie (*e.g.*, Brinchmann et al., 2004; Salim et al., 2007; Rosario et al., 2016), which we discuss below. If a source fulfils this requirement only in  $H\alpha$  it is classified as undetermined.

If a galaxy does fulfil all the S/N requirements, we use Figure 4.2a, to classify a galaxy as star-forming if it falls below the Ka03 line (Equation 1.3; Kauffmann et al., 2003c). If a galaxy falls between the Ka03 line and the Ke01 line (Equation 1.4; Kewley et al., 2001), then it is classified as composite, and the emission is likely due to a combination of star formation and AGN/LINER activity. If a galaxy falls above the Ke01 line, we classify it as either an AGN or a LINER (Low-Ionisation Nuclear Emission-line Region). We explain how these two objects are differentiated below.

If a source only fulfils the S/N criteria in  $H\alpha$ ,  $[OIII]$  and  $H\beta$ , this provides an upper limit on the  $H\alpha/[NII]$  ratio. Thus if this source falls below the Ka03 line, it is still classifiable as star-forming. Else, it is classified as uncertain. If a source only fulfils the S/N criteria in  $H\alpha$ ,  $[NII]$  and  $H\beta$ , this provides an upper limit on the  $[OIII]/H\beta$  ratio. Thus if this source falls below the Ka03 line, it is still classifiable as star-forming. Else, it is classified as uncertain. If a source only fulfils the S/N criteria in  $H\alpha$ ,  $[NII]$  and  $[OIII]$ , this provides a lower limit on the  $[OIII]/H\beta$  ratio. Thus if this source falls above the Ke01 line, it is still classifiable as either an AGN or a LINER. Else, it is classified as uncertain. If a source only fulfils the S/N criteria in  $H\alpha$  and  $H\beta$ , this provides a lower limit on the  $[NII]/H\alpha$  ratio, and an upper limit on the  $[OIII]/H\beta$  ratio. Thus if this is source below the Ke01 line, it is still classifiable as star-forming. Else, it is classified as uncertain.

There are three different emission lines we can use to distinguish AGN from LINERs —  $[SII]$ ,  $[OI]$  and  $[NII]$ . The most reliable line is  $[OI]$  (Kewley et al., 2006) and this should be used where possible, so if  $S/N_{[OI]} \geq 3$ , we can use Figure 4.2c, and classify any source falling below the Ke06 line (Equation 1.6; Kewley et al., 2006) as a LINER. This results in the hard cut-off line we see in Figure 4.2c that is not present in (a) or (b) for distinguishing between AGN and LINERs. Where  $S/N_{[OI]}$  is too low,  $[SII]$  is the next best emission line, and so if  $S/N_{[SII]} \geq 3$  we can use Figure 4.2b, and classify any source falling below the Ke06 line (Equation 1.8) as a LINER. Where both  $S/N_{[SII]}$  and  $S/N_{[OI]}$  are too low, we can resort to

Figure 4.2b, and use the S07 line (Equation 1.9; Schawinski et al., 2007), since a source must have  $S/N_{[\text{NII}]} \geq 3$  in order to be classified as either an AGN or a LINER at all. Anything both below this line and above the Ke01 line can be classified as an LINER.

This leaves our volume-limited disk sample with: 712 undetermined galaxies, 2,518 uncertain galaxies, 28,807 star-forming galaxies, 8,669 composite galaxies, 4,843 LINERs and 3,160 optically classified AGN. When the line fluxes ( $\text{H}\alpha$ ,  $\text{H}\beta$ ,  $[\text{OI}]$ ,  $[\text{OIII}]$ ,  $[\text{NII}]$  and  $[\text{SII}]$ ) are varied within their errors (assumed to be Gaussian) using a bootstrapping method iterated 1000 times with replacements, our results do not change.

Some AGN are not optically classifiable, and are instead observable primarily in the infrared regime.

In order to identify this IR-selected AGN, we use the Wide-Field Infrared Survey Explorer (*WISE*). Upon matching our volume-limited, disk-dominated sample, we find that, as expected, the majority of our sources are detected in *WISE* (48,538 matches). However, at the low redshift limit of our sample  $z \leq 0.1$ , *WISE* is particularly sensitive to star-formation. Thus, we use the WISE-AGN catalogue, which identifies AGN with a high confidence (see Assef et al., 2018, for full details, including the wavelength cuts). Matching to WISE-AGN is analogous to rejecting optical emission line composites. There are 5 WISE-AGN sources which appear in our volume-limited galaxy sample, 1 of which is already optically classified as an AGN using emission line ratio diagrams, so we reclassify an additional 4 galaxies as AGN, to give us a total of 3,164 AGN.

Examples of different bar strengths in star-forming, AGN-host, and undetermined galaxies are shown in Figure 4.3. For a complete breakdown of how many galaxies are in each morphology category, and in each activity category, see Table D.1 in Appendix D.1. Note that whilst the classification of LINERs, uncertain sources and composite galaxies is important, it is simply so they can be confidently removed from our sample for analysis. We do not explicitly make use of these galaxies, as they are possible contaminants in our otherwise pure sample of Seyferts.

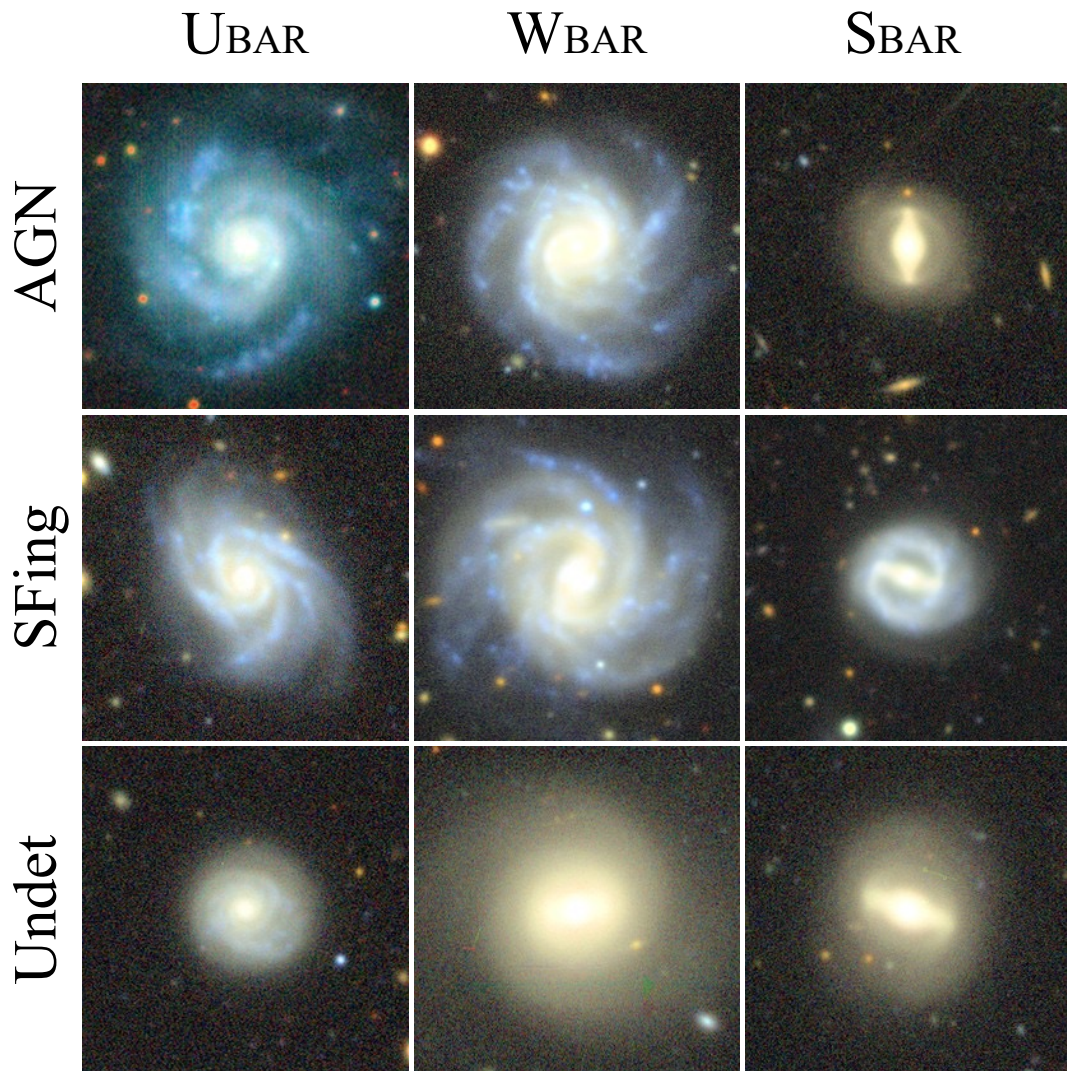


**Figure 4.3:** Examples of each morphology and activity classification. The left-hand column shows unbarred galaxies, the middle shows weakly barred, and the right-hand shows strongly barred galaxies. The top row shows AGN-host galaxies, the middle row shows star-forming galaxies, and the bottom row shows undetermined galaxies according to classification using emission line ratio diagrams. The undetermined galaxies are predominantly red spirals.

### 4.3 Results

We look at the variation in stellar mass ( $M_*$ ) and  $(g-r)_0$  colour, where the 0 indicates we have corrected the  $(g-r)$  colour for galactic absorption, between strongly barred (SBAR), weakly barred (WBAR) and unbarred galaxies (UBAR), and the results are shown in Figure 4.4. For visualisation purposes, we omit the results for WBAR since they lie between the two other samples (however this inclusive plot is shown in Figure D.1 in Appendix D.2). As expected, the star-forming galaxies are less massive and slightly bluer than the AGN hosts. The composite galaxies have overlap with both star-forming and AGN hosts, which confirms that their activity is due to a mixture of star formation and AGN activity. This is very similar to the undetermined galaxies, whose signal-to-noise is too low to classify their activity. The undetermined galaxies are predominantly a mix of quenching and fully quenched disk galaxies. There are also some small differences between the barred and unbarred samples, with bars tending to reside in more massive, redder disks, particularly in both the star-forming samples and the undetermined samples, in agreement with previous studies (*e.g.*, [Masters et al., 2011](#)).

For further analysis, we limit our sample to only star-forming, undetermined and AGN host galaxies to avoid any ambiguity from the LINER and composite samples.

We divide our sample of star-forming, undetermined and AGN host galaxies into our SBAR, WBAR and UBAR samples. Within these three samples, we divide the  $M_*$  and  $(g-r)_0$  each into 15 bins of equal width (over  $10.0 \leq \log(M_*/M_\odot) \leq 12.0$  and  $0.4 \leq (g-r)_0 \leq 2.0$ ), and assign weights to each galaxy such that the weighted distributions of  $M_*$  and  $(g-r)_0$  are matched between the SBAR, WBAR and UBAR subsamples. This conservative mass limit is because AGN are more easily observable in higher mass galaxies, and such a cut reduces this selection bias. We match to whichever sample is smaller in a particular bin. For example, if we have a mass-colour bin containing 13 strongly barred galaxies, 20 weakly barred and 30 unbarred, we match the weak and the unbarred to the strong, since there the smallest contributor is strongly barred galaxies. Changing the lower mass limit between  $10^{9.0} M_\odot$  and  $10^{10.5} M_\odot$  does not change our results.

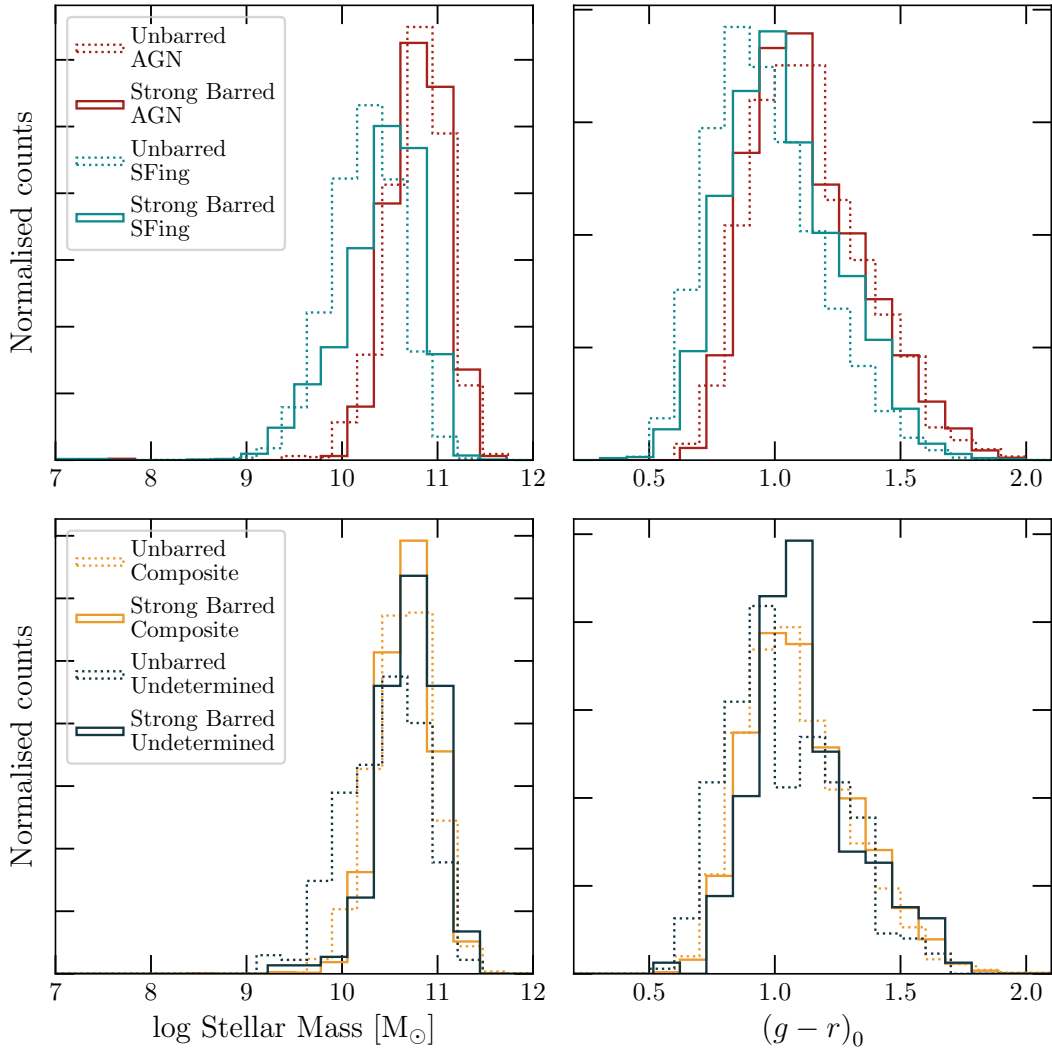


**Figure 4.4:** The distributions in  $M_*$  and  $(g-r)_0$  colour for a variety of subsamples, with strongly barred galaxies in solid lines, unbarred in dotted lines, AGN in red, star-forming in teal, composite in orange and undetermined in navy blue. Weakly barred galaxies are not shown for simplification, but lie between the strongly barred and unbarred samples.

**Table 4.1:** The percentage of each activity category within each bar classification, as shown in Figure 4.5.

	Strongly Barred	Weakly Barred	Unbarred
AGN	$31.6 \pm 0.9$	$23.3 \pm 0.8$	$14.2 \pm 0.6$
Star-forming	$63.6 \pm 0.9$	$73.6 \pm 0.8$	$83.9 \pm 0.6$
Undetermined	$3.1 \pm 0.3$	$4.7 \pm 0.4$	$1.9 \pm 0.2$

AGN presence is known to correlate with stellar mass and colour (Kauffmann et al., 2003c; Sánchez et al., 2004; Aird et al., 2012), and we want to reduce selection effects, and ensuring that the distributions are the same will aid this. We then determine the fraction in each bar category of AGN, star-forming and undetermined galaxies. The weighted results are shown in Figure 4.5, and Table 4.1. Errors arise from the binomial distribution (Cameron, 2011).

Given the small errors on each of these fractions within each bar category, it is highly unlikely that any of these subsamples are drawn from the same parent distribution. These initial results indicate that strongly barred disk galaxies are more likely to host AGN than weakly barred disk galaxies, which are more likely to host AGN than unbarred disk galaxies. However, given the ranges of  $M_*$  and  $(g-r)_0$ , we endeavour to examine these fractions as a function of both, whilst simultaneously examining how the AGN fractions may vary across  $M_*$ – $(g-r)_0$  space. Given that we cannot calculate the SFR of the AGN hosts, we cannot control for SFR, and thus we combine star-forming galaxies and undetermined galaxies into one category, which we refer to as ‘inactive’ galaxies.

### 4.3.1 AGN–bar correlation with stellar mass and colour

We divide our sample of AGN hosts and inactive galaxies into nine bins in  $M_*$  and nine bins in  $(g-r)_0$  colour. Within each bin, we calculate the AGN fraction in strongly barred galaxies,  $f_{\text{AGN,SBAR}}$ , and the AGN fraction in unbarred galaxies,  $f_{\text{AGN,UBAR}}$ . We then find the difference in these two fractions, and this is shown in Figure 4.6a. It can be assumed that there is one, real, intrinsic value for this difference, but when we sample it, we get some scatter. Thus, by sampling it multiple times by varying the binning, we should get an approximately Normal distribution that centres around the true value.

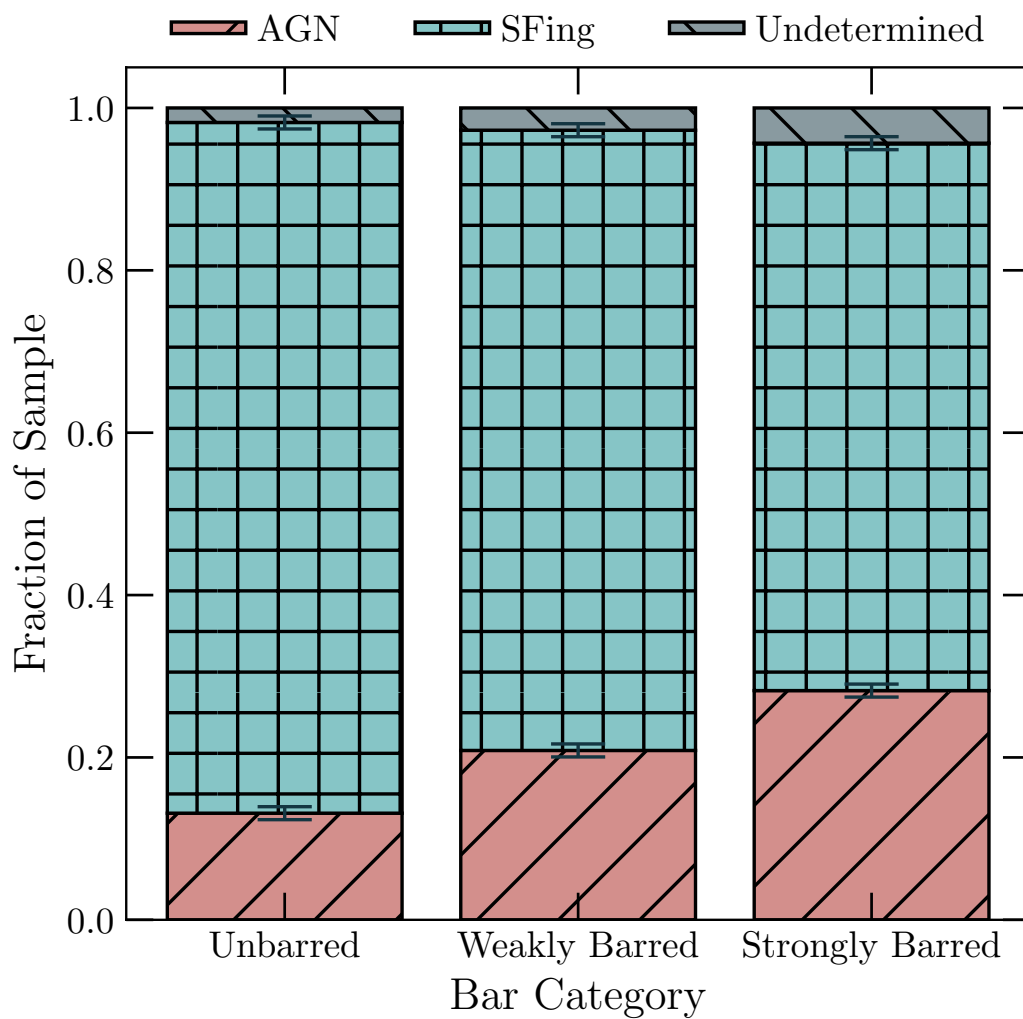


**Figure 4.5:** The distribution of activity classification within each bar category, as shown in Table 4.1 AGN fraction is shown as positive diagonal in red, star-forming (SFing) is shown as teal square hatching, and Undetermined is shown as navy blue negative diagonal. Whilst in all three bar categories, the AGN fraction is smaller than the inactive fraction, the strongly barred galaxies have a noticeably greater fraction of AGN than the weakly barred galaxies, which in turn have a greater AGN fraction than the unbarred galaxies.

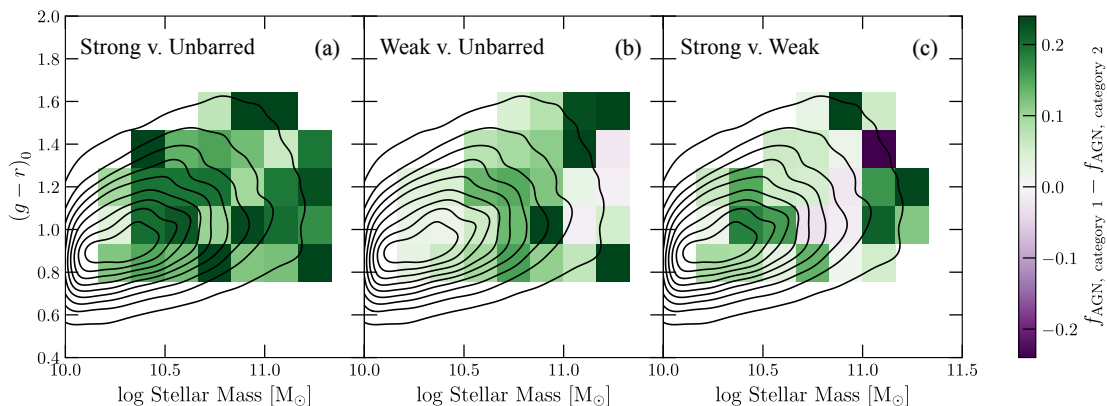


**Figure 4.6:** The difference between the AGN fraction in two bar categories for every combination of SBAR, WBAR and UBAR with  $M_*$  on the  $x$ -axis and  $(g-r)_0$  colour on the  $y$ -axis. In each case, the label along the top is written as ‘Category 1 v Category 2’. The black contours indicate the population of disk galaxies (AGN-host and inactive) within the volume limit. The 2D histogram indicates the distribution of AGN-host disk galaxies, where there are a minimum of 17 AGN in a bin. Where the bin is more green, this indicates that the fraction of Category 1 galaxies hosting AGN is greater than the fraction of Category 2 galaxies hosting AGN. Where the bin is more purple, the reverse is true.

The difference between the two fractions is shown as a colour bar, where green indicates that the fraction of strongly barred galaxies which host AGN is greater than the fraction of unbarred galaxies which host AGN. In order to reduce noise, we only show bins where there are at least 17 AGN in a bin. Varying the minimum AGN count per bin within reasonable values does not change our qualitative result. Every bin is green, with approximately  $f_{\text{AGN,SBAR}} - f_{\text{AGN,UBAR}} \approx 0.18$ . This is a small but significant increase in the number of AGN in strongly barred galaxies.

When we repeat this analysis for WBAR v UBAR our result is qualitatively similar, in that weakly barred galaxies appear more likely to host an AGN. But the signal is much less strong, indicating that any effect that weak bars have on AGN presence is less pronounced than for strong bars, which is also reflected in the lower fractions over the full  $M_*$ - $(g-r)_0$ -matched sample. This is plotted in Figure 4.6b. Overall the AGN fraction is still higher in weakly barred galaxies than in disk galaxies without bars.

We can directly compare SBAR and WBAR across the  $M_*$ - $(g-r)_0$  diagram

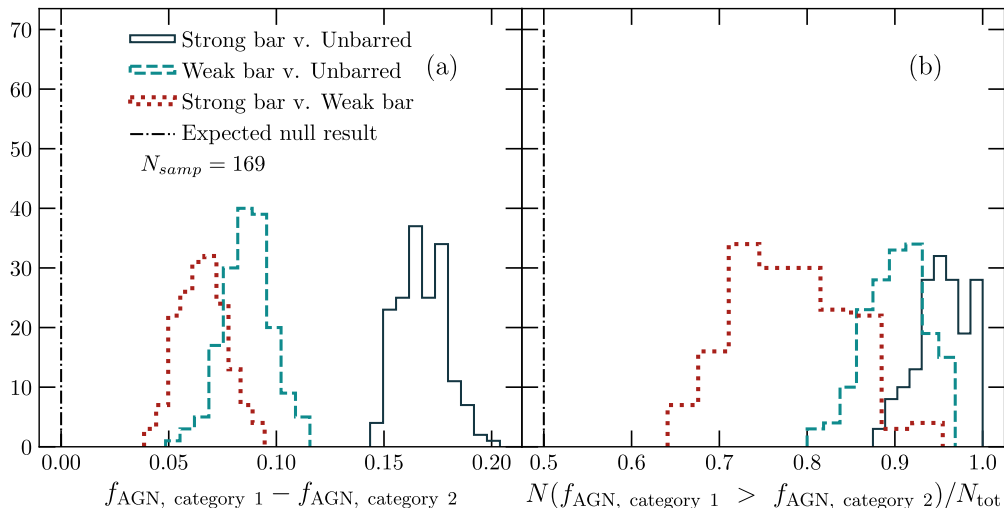


**Figure 4.7:** The distributions of the median difference between AGN fractions ( $f_{\text{AGN,category1}} - f_{\text{AGN,category2}}$ ) in Panel (a), and the distribution of the fraction of bins where Category 1 bars are greater than Category 2 in Panel (b), in a sample consisting of AGN-host galaxies and inactive galaxies. In each case, the legend is written as ‘Category 1 v Category 2’. The black dash-dotted lines indicate the expected mean of the distributions if bar presence did not affect AGN presence. The navy blue, solid lines represent SBAR v UBAR. The teal, dashed lines represent WBAR v UBAR. The red, dotted lines represent SBAR v WBAR. The further to the left of the expected null result the histograms lie, the greater the tendency for AGN to lie in Category 1 bar galaxies. The median difference between the AGN fractions is, in other words, the median value of the differences in the AGN fractions for a particular binning combination.  $N$  represents the number of bins where the AGN fraction in Category 1 is greater than the AGN fraction in Category 2, and  $N_{\text{tot}}$  represents the total number of bins.

as well (Figure 4.6c), and we find that the fraction of strongly barred galaxies hosting AGN is significantly greater than the fraction of weakly barred galaxies hosting AGN, although again this is less pronounced than in Figure 4.6a.

Given that any increase in AGN fraction is small, we check that this value is not overly dependent on binning, and we repeat these calculations for every  $M_*$  and  $(g-r)_0$  bin combination from 5 bins to 17 bins, for a total of 169 bin combinations. For each binning combination, we calculate the median difference in AGN fraction (*e.g.*,  $f_{\text{AGN,SBAR}} - f_{\text{AGN,UBAR}}$ ), and we plot these medians in Figure 4.7a. We assume that the different binning choices each sample the true value of

the difference in AGN fraction between subsamples, such that the distribution of values recovered from all binning choices represents the measured value and its uncertainty. This means that the histogram for each comparison does not consist of independent measurements, but rather is expected to peak around the true value of the difference in the AGN fraction.

If there was no difference in the likelihood of hosting an AGN between these three subsamples, we would expect the histograms to centre around 0 (*e.g.*,  $f_{\text{AGN,SBAR}} - f_{\text{AGN,UBAR}} = 0$ ). We always take the weaker bar category from the stronger bar category, so if the peak of the histograms is greater than 0, the stronger bar category is more likely to host an AGN than the weaker, and vice versa if the peak of the histogram is less than 0.

Figure 4.7a shows that the stronger bar category is more likely to host an AGN than the weaker bar category in every case: strongly barred galaxies are more likely to host an AGN than weakly barred galaxies, which are in turn more likely to host an AGN than unbarred galaxies. Yet this excess of AGN we see is very small. The difference in AGN fraction between strongly barred and unbarred galaxies is  $0.17 \pm 0.01$ , between strongly barred and weakly barred is  $0.07 \pm 0.01$ , and between weakly barred and unbarred is  $0.09 \pm 0.01$ .

A Shapiro-Wilk test (Shapiro & Wilk, 1965) shows that we cannot reject Normality for any of the distributions of the medians, with  $p$ -values in each case greater than  $p_{\text{SW}} > 0.21$  ( $< 1.3\sigma$ ). Given that these distributions are consistent with the Normal distribution, we can perform a simple T-test (Student, 1908) to quantify the significance of this excess of AGN. In each of these cases, the  $p$ -value resulting from a T-test is  $p_{\text{T}} \ll 1 \times 10^{-6}$  ( $\gg 5\sigma$ ), and thus we reject the hypothesis that the likelihood of each of these bar categories hosting an AGN are identical to each other. Furthermore, we can say that the galaxies in UBAR are less likely to host an AGN than the galaxies in SBAR or WBAR category to a  $5\sigma$  confidence.

For each binning combination, we also calculate the fraction of bins where the stronger bar category hosts a greater AGN fraction than the weaker bar category (*e.g.*,  $f_{\text{AGN,SBAR}} > f_{\text{AGN,UBAR}}$ ), and we plot these values in Figure 4.7b.

For example, if we have  $5 \times 5$  bins, and 20 bins have  $f_{\text{AGN,SBAR}} > f_{\text{AGN,UBAR}}$ , we would report a value of 0.8 for this bin combination. If there was no difference in

the likelihood of hosting an AGN between our three subsamples, we would expect the distributions to centre around 0.5 — half of the bins would show a greater fraction of AGN in one bar category than the other. This point is signified by a dash-dotted line.

Comparing SBAR and UBAR, the fraction of bins where SBAR has a greater AGN fraction is  $0.95 \pm 0.03$ . For SBAR vs WBAR this is  $0.78 \pm 0.06$ , and for WBAR vs UBAR, the fraction of bins where WBAR has a greater AGN fraction is  $0.90 \pm 0.04$ , where errors arise from the standard deviation.

Again, we perform a Shapiro-Wilk test for Normality. For the combination WBAR vs UBAR, we obtain a  $p$ -value of  $p_{\text{SW}} = 0.10$  ( $1.6\sigma$ ), and thus for this comparison, we can use a T-test to quantify the significance of the excess of bins containing a higher AGN fraction in the weakly barred category. The  $p$ -value resulting from this T-test is  $p_{\text{T}} \ll 1 \times 10^{-6}$  ( $\gg 5\sigma$ ).

Since we can reject Normality for SBAR vs UBAR, and SBAR vs WBAR, ( $p_{\text{SW}} \leq 0.03$ ), we must use the more conservative method of calculating the number of standard deviations between the mean and the null result of 0.5. For SBAR v UBAR, with a mean value of 0.95, and a standard deviation,  $\sigma_{\text{SD}}$ , of 0.03, we can say that the mean is  $15\sigma_{\text{SD}}$  away from 0.5, and therefore is not in agreement. For SBAR v WBAR, with a mean value of 0.78, and a standard deviation,  $\sigma_{\text{SD}}$ , of 0.06, we can say that the mean is  $13\sigma_{\text{SD}}$  away from 0.5, and therefore is not in agreement. Thus, in each case, the stronger bar category has an AGN fraction that is greater than the weaker bar category. This occurs across the  $M_*(g-r)_0$  regime, meaning that there is not one specific combination of  $M_*$  and colour driving this relationship, further justifying that our results are not sensitive to the choice of binning.

The trends between bar strength and AGN activity are likely a mix of relatively straightforward and more complex results. We discuss these further below.

## 4.4 Discussion

Our overall result, with AGN activity in both unbarred and barred disk galaxies, confirms that a large-scale bar is not *required* to feed an AGN in the secular-

evolution regime. There are multiple secular channels see Section 1.2.3.1 by which matter from the kiloparsec-scale disk can flow into the SMBH sphere of influence, according to both simulations (*e.g.*, Ciotti et al., 1991; Friedli & Benz, 1993; Sakamoto, 1996; Maciejewski et al., 2002; Regan & Teuben, 2004; Hopkins & Hernquist, 2006; Ciotti & Ostriker, 2012; Lin et al., 2013; Slater et al., 2019) and observations (*e.g.*, Davies et al., 2007; Smethurst et al., 2021). However, our primary result also shows clear evidence for an increase in AGN activity in both strongly and weakly barred systems, and we focus on discussing this result below.

As described in Section 4.3, we find that strong bars are clearly linked to a higher incidence of AGN activity, and that weak bars show a more subtle, but still positive, correlation. These results clarify the debate over the last few years regarding whether (and how much) bars are associated with AGN activity. They also highlight an emerging consensus regarding the link between bars and AGN. For example, our results agree with Silva-Lima et al. (2022), who counter for selection effects and find that barred galaxies have a higher accretion parameter than unbarred, and that AGN are found more commonly in galaxies with a bar. Since we are looking at incidence rather than luminosity or accretion, this study is particularly complementary. Given that recent studies have shown that strong and weak bars must be considered separately (Géron et al., 2023), this could also be responsible for some of the discrepancies seen in contradicting previous studies (*e.g.*, Cheung et al., 2013; Goulding et al., 2017; Zee et al., 2023), who find no correlation between bars and AGN.

Our findings are consistent with recent evidence that strong and weak bars have different formation mechanisms (*e.g.*, Géron et al., 2023): strong bars are triggered by global disk instabilities, whereas weak bars are formed through tidal interactions. These formation mechanisms could both be responsible for triggering an AGN. Thus, the AGN's presence may not be directly due to the bar, but rather to the same mechanisms that caused the bar to form. If the physical mechanisms are different for strong and weak bars, this leads to a different coincidence between AGN and the two different bar strengths. Tidal interactions may be more efficient at depleting gas from the centre of the galaxy than secular processes that do not lead to the development of a bar, such that by the time the

disk galaxy has evolved to a higher stellar mass, the AGN has been deprived of fuel and shut down, although the weak bar still remains in place.

We postulate that were a strong bar present in a galaxy, this bar is efficient at fuelling gas down to the central kiloparsec, where it can be accreted onto an AGN. If weak bars are less efficient at driving gas to the centre of the galaxy, this would explain why we see a much weaker correlation between weakly barred galaxies and AGN than strongly barred galaxies and AGN.

There is recent evidence from IllustrisTNG that an AGN could drive changes in a bar (Lokas, 2022). This is due to the AGN switching to kinetic-mode feedback, causing depletion of gas in the inner regions, leading to quenching and bar formation. However, given the physical scales that we are looking at, this seems unlikely to be occurring on a large scale in our sample, due to the differences in AGN and bar lifetimes.

It is important to assess the potential contribution to this result of any selection biases. As described in Section 4.2, we take various steps to minimise these biases, such as controlling for  $M_*$  and  $(g - r)_0$  colour, and using a volume limit to ensure completeness. We also consider the effects of the changing physical resolution across the sample. At higher redshifts, the minimum size of bar we can detect increases: we lose smaller bars at higher redshift. Weak bars tend to be shorter than strong bars, proportional to the size of the galaxy. This means we preferentially lose weaker bars as we increase in redshift, especially in lower mass galaxies. In a low mass galaxy, a weak bar may be missed, and that galaxy classified as unbarred.

We do not have individual bar lengths and widths for all the galaxies in this sample, and thus we cannot fully compensate for this potential source of selection bias at an individual galaxy level. However, one way to examine how strong this effect is likely to be in our sample is to remove the high redshift sources, because this will significantly reduce the overall difference between minimum resolved bar size between the lowest and highest redshifts of the subsample. We have thus examined the subset of our volume-limited sample with  $z < 0.05$  (12,251 disk galaxies), and the overall trends seen in Figure 4.6 still persist.

Further work could be done to investigate the inflow rates that each of these bar types could sustain, and combining this with the gas availability could show

why weak bars do not correlate with AGN presence as much as strong bars, as if they cannot provide as high an inflow rate as strong bars, they require more gas to trigger an AGN. High-resolution IFU data will allow us to measure star-formation rates of the AGN-host galaxies, and thus draw comparisons between AGN and non-AGN hosts, both in star-forming and quiescent galaxies. X-ray data will allow investigation of black hole accretion rates, and spectroscopy along the axis of the bar will allow bar inflow rates to be obtained.

This phenomenon will also be investigated at more distant redshifts (Margalef-Bentabol, 2023, Margalef-Bentabol et al., in prep.), along with how these AGN are fuelled as the bar fraction decreases out to higher redshifts. Facilities such as *Euclid* will provide us with greater sky coverage at better resolution than currently available, and so with an increase in data, we should be able to reduce noise in our samples.

## 4.5 Conclusions

We have investigated the influence of large-scale bars on the likelihood of AGN signals in a volume-limited sample of 48,871 disk galaxies by analysing data from the DESI catalogue, Galaxy Zoo DESI morphologies, and SDSS emission line strengths. We have taken care to control for differences in stellar mass and galaxy colour distributions between subsamples of strongly barred, weakly barred, and unbarred galaxies.

99.9% of our 3,164 AGN in disk galaxies are identified via optical emission line diagnostics, with a mere 4 AGN only detectable via WISE infrared colours within our volume limit. We divide galaxies without clear AGN activity into multiple categories based on the detection of emission lines in SDSS spectra, and focus our comparison with the AGN host galaxies on two inactive categories: 28,807 star-forming galaxies with detected nebular emission lines below the “composite” limit on an emission line ratio diagram, and 712 “undetermined” galaxies where nebular emission lines are not robustly detected in the central fibre spectra. These latter galaxies are, on visual inspection, predominantly red spirals, with a smaller fraction being disks that have red/quenched inner regions and bluer outer regions.

Our key findings can be summarised as follows:

- Strongly barred galaxies are more likely to host an AGN than weakly barred galaxies, which in turn are more likely to host an AGN than unbarred galaxies.
- This effect is very slight, with the percentage of AGN in each bar category being:  $f_{\text{AGN,SBAR}} = 31.6 \pm 0.9\%$ ,  $f_{\text{AGN,WBAR}} = 23.3 \pm 0.0\%$  and  $f_{\text{AGN,UBAR}} = 14.2 \pm 0.6\%$ .

The high levels of statistical significance achieved here even after controlling for the confounding effects of colour, stellar mass, and flux limits, have been facilitated by the advent of large sample sizes from the latest generation of extragalactic surveys and the highly accurate and detailed morphological identifications of strongly barred, weakly barred, and unbarred disk galaxies. In the near future, we expect to use data from surveys such as *Euclid* and LSST to extend these analyses to higher redshift and further refine our understanding of the interplay between various types of disk instabilities and growing supermassive black holes.

# Chapter 5

## Conclusions

The results presented in this thesis further our understanding of the link between large-scale galactic bars and AGN. We briefly recap the conclusions of each chapter above, before explaining where this work fits into the field as a whole, and what the next steps may entail.

In Chapter 3, we use a sample of unambiguously disk-dominated galaxies hosting luminous, Type 1 AGN. The parent sample of these galaxies were shown in Simmons et al. (2017b) to exhibit co-evolution according to the  $M_* - M_{\text{BH}}$  relationship. Thus we know that co-evolution is occurring, and we know that this is driven through secular processes due to the bulgelessness of the host galaxies.

We use longslit optical spectroscopy from the Kast Double Spectrograph on the Shane Telescope at Lick Observatory (with data reduction detailed in Chapter 2) to obtain accurate SFRs for 34 AGN host galaxies, and we use a combination of SDSS and HST imagery to obtain stellar masses from the MPA-JHU catalogue via a more accurate method than using SDSS alone. This allows us to use an inactive disk sample carefully controlled for stellar mass to show that the SFR of inactive galaxies is consistent with being drawn from the same parent sample as the SFR of our AGN-host sample ( $p_{\text{KS}} = 0.38$ ,  $\sigma = 0.9$ ).

After controlling for both SFR and stellar mass, we analyse the bar presence in each sample. The bar fraction in the AGN-host sample is  $f_{\text{bar}} = 0.59_{-0.09}^{+0.08}$ , and in the controlled inactive comparison sample is  $f_{\text{bar}} = 0.44_{-0.09}^{+0.08}$  — a  $\sim 1.7\sigma$  difference. The agreement to within  $2\sigma$  but not to within  $1\sigma$  is a strong indication

---

that the sample size is too small to draw meaningful statistical results. Many other studies, such as [Silva-Lima et al. \(2022\)](#) also struggle to discern a link due to high uncertainties when conducting this kind of investigation, and we need to make use of large datasets in order to tease out a result.

Chapter 4 uses GZ DESI (GZD) to select a volume-limited sample of disk galaxies consisting of 3,164 Type 2 AGN hosts, 28,807 star-forming galaxies, and 712 undetermined galaxies. These activity sources are determined using emission-line diagrams, meaning that undetermined galaxies are those without much emission. Given that our sample consists only of disk galaxies, these undetermined galaxies are predominantly red spirals. We compare the AGN sample to the star-forming and undetermined galaxies (combined into one ‘inactive’ sample).

Each galaxy is labelled as either strongly barred, weakly barred or unbarred using the classifications in GZD. Given that this sample is  $\sim 100$  times bigger than that in Chapter 3, the uncertainties on the statistical analysis are much smaller. After controlling for  $(g-r)_0$  colour and stellar mass, the AGN fraction in strongly barred galaxies is  $f_{\text{AGN,SBAR}} = 0.316 \pm 0.009$ , in weakly barred galaxies is  $f_{\text{AGN,WBAR}} = 0.233 \pm 0.008$  and in unbarred galaxies is  $f_{\text{AGN,UBAR}} = 0.142 \pm 0.006$ . Strongly barred galaxies are, to a high confidence level, more likely to host AGN than either weakly barred or unbarred galaxies. This correlation is seen across colour–mass space, indicating that this relationship is not just present at one regime.

These two contrasting studies provide valuable insight into not only the interplay between bars and AGN, but into the importance of large-scale surveys and developing reliable analytical methods to deal with the copious amounts of data.

The first allowed us to investigate a more extreme sample, using the most luminous AGN in the most bulgeless galaxies to demonstrate the extreme possibilities of bar-driven fuelling, whereas the second allowed us to examine a larger, less constrained sample to investigate overall trends. Whilst the first showed the extreme possibilities of bar-driven fuelling, the second demonstrated that this correlation is pervasive throughout disk galaxies and demonstrated agreement with recent simulations such as [Kataria & Vivek \(2024\)](#).

Given that these two works lie at opposite ends of the sample selection spectrum, it would seem reasonable that a good compromise could be found, factoring

---

in the need for a large sample with the opposing needs for high-resolution spectroscopy, and stringent sample constraints. Yet it would appear that in doing so, we are still not able to obtain fully robust and reliable results.

Chapter 4 does not separate host galaxies by bulge prominence, meaning that we may not be looking exclusively at the merger-free regime. This is because Galaxy Zoo is not ideal for quantifying the bulge strength when there is also an AGN present in ground-based surveys. Volunteers can easily mistake a bright AGN for a bulge, contaminating the sample. Conversely, they may overcorrect and assume that the bulge is actually just AGN emission. This issue is not restricted to methods based on visual identification, and affects any attempt at bulge-disk decomposition if the AGN is not explicitly included.

This potentially large bulge component also means that we are not necessarily looking at young bars. We know that any bars in Chapter 3 are likely young bars since over time bars can build up pseudobulges (see Combes, 2009, for a review). The complete lack of bulge component in the sample of Chapter 3 indicates that any bars present have not had sufficient time to build up a pseudobulge. If a bar forms and quickly causes the switch-on of an AGN, this AGN is likely to be shorter lived than the bar. Potentially by the time we observe the source, the AGN is no longer present, but the bar still is, which can dilute results. Despite this caveat, Chapter 4 still demonstrates a clear correlation between bar and AGN presence that is not definitively seen in the small sample size of Chapter 3.

Chapters 3 and 4 both analyse the bar–AGN link in slightly different ways, with the former looking at the fraction of barred galaxies in a sample of AGN hosts, and the latter looking at the fraction of AGN hosts in a sample of barred galaxies, either strong or weak. This is because Chapter 3 aims to mitigate the caveat of bars and AGN having different lifetimes as much as possible, and looking at the bar fraction in AGNDISKS aids this. However, in Chapter 4, it is more appropriate to look at the AGN fraction to investigate to what extent bars can correlate with AGN.

For a more direct comparison, we note here that the stellar mass and  $(g-r)_0$  colour controlled sample in Chapter 4 yields a fraction of strong bars in the AGN sample of  $f_{\text{SBAR,AGN}} = 40.0 \pm 1.0\%$ , compared to  $f_{\text{SBAR,Inactive}} = 24.5 \pm 0.5\%$  in the inactive sample (consisting of undetermined and star-forming galaxies). Including

---

**Table 5.1:** The bar percentages for both AGN hosts and inactive galaxies in the GZD sample (Chapter 4). Conversely to the chapter, which looks at the activity fractions, looking at the bar fractions allows for a more direct comparison with the work done in Chapter 3.

	AGN hosts	Inactive galaxies
Strongly barred	$40.0 \pm 1.0$	$24.5 \pm 0.5$
Weakly barred	$34.7 \pm 1.0$	$43.2 \pm 0.6$
Unbarred	$25.3 \pm 1.0$	$32.3 \pm 0.5$

weak bars as well, these fractions become  $f_{\text{SBAR+WBAR,AGN}} = 74.7 \pm 1.0\%$  and  $f_{\text{SBAR+WBAR,Inactive}} = 56.8 \pm 0.7\%$ , respectively. These results are shown in Table 5.1.

Note that Table D.1 shows the raw counts, *i.e.*, before controlling for  $(g - r)_0$  colour and stellar mass. These are therefore not *directly* the values used to calculate bar fraction or AGN fraction. Using the raw values from the volume-limited sample to calculate these fractions would result in slightly different values, since the values would not be controlled for colour and stellar mass. For example, we would expect the fraction of barred galaxies in the AGN sample to be higher if we used controlled values than raw values, since both AGN and bar presence show a positive correlation with stellar mass (Kauffmann et al., 2003c; Aird et al., 2012; Skibba et al., 2012).

This bar fraction in the Chapter 4 AGN sample is in agreement with the results shown in Chapter 3, where the bar fraction in AGNDISKFIN is shown to be  $59 \pm 9\%$ , however as discussed in more detail in Chapter 3, the large error bars make drawing any substantial conclusion challenging. In both studies, the bar fraction in the AGN sample is higher than in the inactive sample.

This further cements the theory that there is a correlation between bars and AGN, and that either method (bar fraction or AGN fraction) yields qualitatively the same result. Given that the two chapters are in agreement with each other despite the former only looking at young bars, this indicates that bar age is not relevant to the observed bar–AGN correlation.

Galloway et al. (2015) also used ground-based surveys to identify AGN in disks, without folding in bulge prominence, but this only results in a sample of 681 AGN. They separated disks into barred and unbarred rather than strongly barred,

weakly barred and unbarred. This means that some of their barred sample will likely also contain weak bars. As shown in Chapter 4, the AGN–bar correlation is driven by strong bars, so including weak bars will dilute this effect. Ground-based surveys also mean that smaller bars may be missed, and strongly barred galaxies may be classified as weakly barred, or weakly barred as unbarred. The resolution of DESI compared to SDSS goes a long way in obtaining more accurate bar classifications, but we note it will still suffer from missed bars.

Simmons et al. (2017b) note that the AGN presence combined with SDSS resolution means that only an upper limit on bulge mass is possible, since smaller bulges may either be hidden under the AGN emission, or resolved out. In Chapter 3, we describe how the galaxies were examined by a single expert classifier using comparison between SDSS images and *HST* images, since separating the AGN and the bulge is easier in *HST*. This is highly impractical for larger datasets, and beyond the scope of this thesis with current published surveys. However, using this smaller dataset with high-resolution longslit spectroscopy allowed for precise controlling of parameters known to correlate with AGN presence, such as SFR and stellar mass. Again, collecting this level of spectroscopy for large samples is highly impractical.

## 5.1 Future Work

Although this work has demonstrated that large-scale galactic bars are correlated with AGN presence, there are a number of outstanding questions. The results outlined above confidently show this correlation to a high level of statistical significance, more so than currently in the literature. That we as a field can be more confident of the bar–AGN link, we can now look towards the open questions that remain unanswered.

In order to detect a correlation over the entire disk galaxy population, Chapter 4 does not remove disk-dominated galaxies with a bulge component. This means we are not fully isolating the merger-free regime. By adding a further constraint (that of bulgelessness) to this study, future work could investigate whether this

bar–AGN connection remains present in the absence of mergers. However, this requires high-resolution data over a large volume of the sky.

We need morphology classifications for space-based, large-scale surveys, which will soon be possible given that *Euclid* was successfully launched in July 2023, and has started collecting data. Over its six-year primary mission, *Euclid* will observe a third of the sky to a resolution on par with that of *HST*. This sheer volume of data means we will be able to obtain samples of the same order of magnitude as the Chapter 4 sample, but with more constraints applied, such as low bulge prominence. The resolution limit of *Euclid* means that bulge prominence will be identifiable by Galaxy Zoo volunteers (whose classifications will be used to train machine learning models) to the same accuracy as a single expert classifier using *HST* photometry.

There is much work to be done on understanding the physics behind this correlation. Why does the presence of a bar lead to a higher AGN fraction? Does the bar strength correspond to the accretion rate of the black hole? X-ray data can be used to find the accretion rate (*e.g.*, Torbaniuk et al., 2021), and by combining this with the bar strength (*e.g.*, using vote fractions from GZ as a proxy for strength), the existence of this spectrum can be investigated.

The second key avenue of physics that remains unexplored in this work is the effect of AGN presence on star-formation rate. High-resolution, optical IFU data would allow star formation rate to be measured across the galaxy after disentangling the AGN emission. The star-formation rate should be determined at varying distances away from the AGN, as well as at different angles to the bar. This could aid in tracing the distribution of gas within the galaxy with respect to both the AGN and the bar.

This work only investigates two subpopulations of AGN — that of luminous, Type 1 AGN, and that of optically detected, Type 2 AGN (as well as four additional sources from WISE). This leaves the X-ray detected regime, and the radio-detected sources yet to be investigated. Future work can investigate whether this correlation is present for AGN detected at all wavelengths, and how it changes depending on the detection method.

The high resolution in the infrared of *JWST* opens up this study to the potential for exploration at higher redshifts. As redshift increases, AGN activity

also increases (Figure 1.7), yet bar fraction decreases (*e.g.*, [Le Conte et al., 2024](#)). This means that bars are unlikely to be as significant in AGN fuelling at higher redshifts, and *JWST* would allow for this study to be undertaken.

# Appendix A

## Glossary

- **AGN.** Active Galactic Nucleus
- **BASS.** Beijing-Arizona Sky Survey
- **BH.** Black Hole
- **BLR.** Broad Line Region
- **CANDELS.** Cosmic Assembly Near-infrared Deep Extragalactic Legacy Survey
- **DECaLS.** DECam Legacy Survey
- **DECam.** Dark Energy Camera
- **DES.** Dark Energy Survey
- **DESI.** Dark Energy Spectroscopic Instrument
- **DESI-LS.** DESI Legacy Surveys
- **EAGLE.** Evolution and Assembly of GaLaxies and their Environments
- **EM.** ElectroMagnetic
- **FIRE.** Feedback In Realistic Environments

- 
- **GZ.** Galaxy Zoo
  - **HST.** Hubble Space Telescope
  - **IRAC.** InfraRed Array Camera
  - **LINER.** Low-Ionisation Nuclear Emission line Region
  - **LSST.** Legacy Survey of Space and Time
  - **MzLS.** Mayall z-band Legacy Survey
  - **NGC.** Northern Galactic Cap
  - **NLR.** Narrow Line Region
  - **SDSS.** Sloan Digital Sky Survey
  - **SFH.** Star Formation History
  - **SGC.** Southern Galactic Cap
  - **SMBH.** SuperMassive Black Hole
  - **WISE.** Wide-field Infrared Sky Explorer

# Appendix B

## Chapter 2

Table B.1 shows the galaxies that were observed on the campaign described in detail in Chapter 2. and Table B.2 shows the stars that were used as standard stars.

Table B.1: The galaxies observed with the Kast Double Spectrograph on the campaign that took place from October 2016 to November 2018. Those used in Chapter 3 are highlighted in bold, with a full table of their properties in Table 3.1. A number of these galaxies were not in the initial observing proposal, but were back-up targets from wider members of the collaboration that the PI was able to observe.

SDSS Object ID	PA /°	Exp Time /s	RA /°	Dec /°
587724197739495456	262.5	928	11.896387	14.155118
587724198817825040	196.7	928	22.740557	14.436502
587724198817825040	106.6	928	22.740557	14.436502
587724232105132134	137.7	750	20.146263	14.053301
587724232644755619	218.9	928	26.703212	13.772668
587724232644755619	128.9	928	26.703212	13.772668
587724233719218342	179.8	7600	28.375665	14.570941

Continued on next page

Table B.1: The galaxies observed with the Kast Double Spectrograph on the campaign that took place from October 2016 to November 2018. Those used in Chapter 3 are highlighted in bold, with a full table of their properties in Table 3.1. A number of these galaxies were not in the initial observing proposal, but were back-up targets from wider members of the collaboration that the PI was able to observe. (Continued)

SDSS Object ID	PA /°	Exp Time /s	RA /°	Dec /°
587724233719218342	175.5	1875	28.375665	14.570941
587724233719218342	217.2	2250	28.375665	14.570941
587724234256220340	213.5	928	28.868169	14.925302
587724234256220340	293.8	928	28.868169	14.925302
587725504484868436	126.4	1875	259.405909	56.936907
587725504484868436	216.4	1875	259.405909	56.936907
587725578036183361	118.7	1875	263.407090	59.497791
587725578036183361	208.5	1875	263.407090	59.497791
587727221943370027	64.5	1875	343.456792	13.986293
587727221943370027	155.0	1875	343.456792	13.986293
587727221949661431	225.1	1875	358.265800	14.886538
587727221949661431	135.2	1875	358.265800	14.886538
587727223012262207	50.8	1388	332.008629	13.386849
587727223012262207	140.9	1458	332.008629	13.386849
587727223557456064	127.6	1193	351.529386	15.778589
587727223557456064	217.6	1193	351.529386	15.778589
587727223558373588	71.2	1875	353.683822	15.977104
587727223558373588	161.2	1875	353.683822	15.977104
587727223558832317	180.2	1875	354.775878	15.934112
587727223558832317	89.6	1875	354.775878	15.934112
587729227152425018	124.8	1875	240.100302	52.899526
587729227152425018	214.6	1875	240.100302	52.899526

Continued on next page

Table B.1: The galaxies observed with the Kast Double Spectrograph on the campaign that took place from October 2016 to November 2018. Those used in Chapter 3 are highlighted in bold, with a full table of their properties in Table 3.1. A number of these galaxies were not in the initial observing proposal, but were back-up targets from wider members of the collaboration that the PI was able to observe. (Continued)

SDSS Object ID	PA /°	Exp Time /s	RA /°	Dec /°
587729233057087918	71.7	1875	257.380100	37.365528
587729233057087918	161.0	1875	257.380100	37.365528
587729653429174780	131.6	1875	259.681445	27.545968
587729653429174780	41.3	1875	259.681445	27.545968
587730772804698396	71.2	1875	335.927241	11.974310
587730772804698396	161.2	1875	335.927241	11.974310
587730772804698396	71.8	375	335.927241	11.974310
587730772804698396	71.7	1875	335.927241	11.974310
587730772804698396	160.9	1875	335.927241	11.974310
587730773344387381	195.6	1875	342.446152	13.097466
587730773344387381	285.0	2625	342.446152	13.097466
587730773880996145	205.0	1875	341.743135	13.511680
587730773880996145	115.0	1875	341.743135	13.511680
587730774415114540	207.8	4713	335.310191	13.105635
587730774415114540	207.7	1900	335.310191	13.105635
587730774415114540	208.5	3800	335.310191	13.105635
587730774415114540	117.8	2813	335.310191	13.105635
587730774417408317	96.4	1875	340.625345	13.878187
587730774417408317	186.4	1875	340.625345	13.878187
587730774950740380	160.0	1193	332.340204	13.281274
587730774950740380	250.0	1263	332.340204	13.281274
587730774965420341	143.5	2063	6.846040	15.561708

Continued on next page

Table B.1: The galaxies observed with the Kast Double Spectrograph on the campaign that took place from October 2016 to November 2018. Those used in Chapter 3 are highlighted in bold, with a full table of their properties in Table 3.1. A number of these galaxies were not in the initial observing proposal, but were back-up targets from wider members of the collaboration that the PI was able to observe. (Continued)

SDSS Object ID	PA /°	Exp Time /s	RA /°	Dec /°
587730774966420341	123.6	9690	6.846040	15.561708
587730774966420341	123.5	1710	6.846040	15.561708
587730775498162284	73.1	1875	357.102403	15.844780
587730775498162284	163.0	1875	357.102403	15.844780
587732156852797482	135.0	2614	120.087435	26.613531
587735235807215692	210.0	2485	120.152823	22.400052
587736782001340680	131.0	1850	250.973546	25.016199
587736782001340680	221.0	1875	250.973546	25.016199
587739844857168249	76.5	1875	242.017172	14.224046
587739844857168249	166.5	1875	242.017172	14.224046
587741386735616083	103.5	2485	120.088474	14.781841
587742616173740488	273.3	1875	243.515130	14.142904
587742616173740488	182.9	1875	243.515130	14.142904
<b>1237649953863368738</b>	<b>257.2</b>	<b>910</b>	<b>11.830793</b>	<b>14.703507</b>
<b>1237649953863368738</b>	<b>167.2</b>	<b>928</b>	<b>11.830793</b>	<b>14.703507</b>
<b>1237649953863368738</b>	<b>212.0</b>	<b>928</b>	<b>11.830793</b>	<b>14.703507</b>
<b>1237649953863368738</b>	<b>122.0</b>	<b>910</b>	<b>11.830793</b>	<b>14.703507</b>
<b>1237651190281797746</b>	<b>214.4</b>	<b>928</b>	<b>126.456478</b>	<b>47.174481</b>
<b>1237651190281797746</b>	<b>129.8</b>	<b>928</b>	<b>126.456478</b>	<b>47.174481</b>
<b>1237651192434327633</b>	<b>169.6</b>	<b>928</b>	<b>137.477548</b>	<b>56.709857</b>
<b>1237651192434327633</b>	<b>256.0</b>	<b>7600</b>	<b>137.477548</b>	<b>56.709857</b>
1237651249866867161	158.9	928	116.066630	35.977861

Continued on next page

Table B.1: The galaxies observed with the Kast Double Spectrograph on the campaign that took place from October 2016 to November 2018. Those used in Chapter 3 are highlighted in bold, with a full table of their properties in Table 3.1. A number of these galaxies were not in the initial observing proposal, but were back-up targets from wider members of the collaboration that the PI was able to observe. (Continued)

SDSS Object ID	PA /°	Exp Time /s	RA /°	Dec /°
1237651249866867161	248.9	928	116.066630	35.977861
1237651249866867161	162.0	1458	116.066630	35.977861
<b>1237651250439913597</b>	<b>209.7</b>	<b>765</b>	<b>241.886931</b>	<b>48.772268</b>
<b>1237651252578287712</b>	<b>146.3</b>	<b>765</b>	<b>214.049803</b>	<b>63.191177</b>
1237653438691934356	188.0	910	346.072136	-8.279502
1237653438691934356	98.0	910	346.072136	-8.279502
<b>1237654952137195588</b>	<b>144.8</b>	<b>928</b>	<b>259.008049</b>	<b>31.203834</b>
<b>1237655129307742214</b>	<b>183.7</b>	<b>675</b>	<b>256.395611</b>	<b>33.669934</b>
<b>1237655129307742214</b>	<b>273.6</b>	<b>675</b>	<b>256.395611</b>	<b>33.669934</b>
1237655375187869806	46.6	630	255.710281	33.736019
1237655375187869806	136.6	675	255.710281	33.736019
1237656564901740669	184.7	1380	269.034582	54.926871
1237656564901740669	94.7	1380	269.034582	54.926871
1237656567579804203	257.0	928	323.105296	-0.631927
1237656567579804203	167.0	928	323.105296	-0.631927
1237657234367250558	211.2	663	18.140417	0.293278
1237657234367250558	279.0	663	18.140417	0.293278
1237657234367250558	324.0	928	18.140417	0.293278
1237658778948665372	63.5	595	230.957867	4.233593
1237658778948665372	153.4	595	230.957867	4.233593
1237659149386973357	26.2	278	226.968863	51.853115
1237659149386973357	77.6	1875	226.968863	51.853115

Continued on next page

Table B.1: The galaxies observed with the Kast Double Spectrograph on the campaign that took place from October 2016 to November 2018. Those used in Chapter 3 are highlighted in bold, with a full table of their properties in Table 3.1. A number of these galaxies were not in the initial observing proposal, but were back-up targets from wider members of the collaboration that the PI was able to observe. (Continued)

SDSS Object ID	PA /°	Exp Time /s	RA /°	Dec /°
<b>1237659324953460779</b>	<b>175.6</b>	<b>765</b>	<b>242.027833</b>	<b>42.682746</b>
<b>1237659326553391154</b>	<b>139.5</b>	<b>675</b>	<b>211.520086</b>	<b>58.011569</b>
<b>1237659326553391154</b>	<b>62.8</b>	<b>765</b>	<b>211.520086</b>	<b>58.011569</b>
<b>1237659754447634570</b>	<b>182.0</b>	<b>675</b>	<b>8.797843</b>	<b>-0.821666</b>
<b>1237659754447634570</b>	<b>271.8</b>	<b>675</b>	<b>8.797843</b>	<b>-0.821666</b>
<b>1237659896713511217</b>	<b>54.9</b>	<b>1340</b>	<b>265.538582</b>	<b>51.018227</b>
<b>1237659896713511217</b>	<b>145.0</b>	<b>1340</b>	<b>265.538582</b>	<b>51.018227</b>
<b>1237659935903056079</b>	<b>136.4</b>	<b>1540</b>	<b>8.635498</b>	<b>39.310022</b>
<b>1237659935903056079</b>	<b>46.4</b>	<b>1540</b>	<b>8.635498</b>	<b>39.310022</b>
<b>1237659935903056079</b>	<b>151.5</b>	<b>1458</b>	<b>8.635498</b>	<b>39.310022</b>
<b>1237659935903056079</b>	<b>151.8</b>	<b>2485</b>	<b>8.635498</b>	<b>39.310022</b>
<b>1237659935903056079</b>	<b>234.0</b>	<b>1590</b>	<b>8.635498</b>	<b>39.310022</b>
<b>1237659935903056079</b>	<b>232.8</b>	<b>2485</b>	<b>8.635498</b>	<b>39.310022</b>
<b>1237660343925997873</b>	<b>151.8</b>	<b>928</b>	<b>121.499767</b>	<b>26.100667</b>
<b>1237660343925997873</b>	<b>214.0</b>	<b>928</b>	<b>121.499767</b>	<b>26.100667</b>
<b>1237660343925997873</b>	<b>152.0</b>	<b>563</b>	<b>121.499767</b>	<b>26.100667</b>
<b>1237660343925997873</b>	<b>173.3</b>	<b>3102</b>	<b>121.499767</b>	<b>26.100667</b>
1237660554375397927	130.5	190	65.233347	26.080576
1237660554375397927	130.7	1220	65.233347	26.080576
1237660554375397927	40.7	1400	65.233347	26.080576
1237661056893518573	67.0	938	53.565598	40.906427
1237661083733132764	148.0	938	41.855000	44.844111

Continued on next page

Table B.1: The galaxies observed with the Kast Double Spectrograph on the campaign that took place from October 2016 to November 2018. Those used in Chapter 3 are highlighted in bold, with a full table of their properties in Table 3.1. A number of these galaxies were not in the initial observing proposal, but were back-up targets from wider members of the collaboration that the PI was able to observe. (Continued)

SDSS Object ID	PA /°	Exp Time /s	RA /°	Dec /°
1237661121311998362	117.5	750	43.155704	43.163281
1237661121311998362	124.5	1875	43.155704	43.163281
1237661121315603197	198.2	938	52.409397	38.922342
<b>1237662195054673929</b>	<b>130.0</b>	<b>928</b>	<b>158.660816</b>	<b>39.641155</b>
<b>1237662195054673929</b>	<b>220.0</b>	<b>928</b>	<b>158.660816</b>	<b>39.641155</b>
1237662473157345548	208.0	563	242.998126	31.178196
1237662473157345548	208.1	1875	242.998126	31.178196
1237662473157345548	298.1	1875	242.998126	31.178196
1237662500012949661	59.7	765	252.763058	26.296453
1237662500012949661	66.8	765	252.763058	26.296453
<b>1237662504293892158</b>	<b>65.0</b>	<b>165</b>	<b>239.790118</b>	<b>35.029860</b>
<b>1237662504293892158</b>	<b>58.0</b>	<b>1920</b>	<b>239.790118</b>	<b>35.029860</b>
<b>1237662504293892158</b>	<b>148.0</b>	<b>1850</b>	<b>239.790118</b>	<b>35.029860</b>
<b>1237662504293892158</b>	<b>151.1</b>	<b>1875</b>	<b>239.790118</b>	<b>35.029860</b>
<b>1237662504293892158</b>	<b>61.2</b>	<b>1875</b>	<b>239.790118</b>	<b>35.029860</b>
1237662534356369436	90.1	585	228.560527	11.189072
1237662534356369436	180.2	595	228.560527	11.189072
1237662662680051805	193.5	1875	239.578143	25.856887
1237662662680051805	103.6	1875	239.578143	25.856887
<b>1237662719048548439</b>	<b>77.8</b>	<b>765</b>	<b>267.063875</b>	<b>58.393101</b>
<b>1237662719048548439</b>	<b>167.8</b>	<b>765</b>	<b>267.063875</b>	<b>58.393101</b>
<b>1237662981045292635</b>	<b>210.3</b>	<b>765</b>	<b>290.711444</b>	<b>-5.883094</b>

Continued on next page

Table B.1: The galaxies observed with the Kast Double Spectrograph on the campaign that took place from October 2016 to November 2018. Those used in Chapter 3 are highlighted in bold, with a full table of their properties in Table 3.1. A number of these galaxies were not in the initial observing proposal, but were back-up targets from wider members of the collaboration that the PI was able to observe. (Continued)

SDSS Object ID	PA /°	Exp Time /s	RA /°	Dec /°
<b>1237662981045292635</b>	<b>120.3</b>	<b>765</b>	<b>290.711444</b>	<b>-5.883094</b>
<b>1237663307453431955</b>	<b>55.1</b>	<b>765</b>	<b>359.689951</b>	<b>32.520928</b>
<b>1237663307453431955</b>	<b>145.2</b>	<b>765</b>	<b>359.689951</b>	<b>32.520928</b>
<b>1237663307453431955</b>	<b>201.0</b>	<b>1125</b>	<b>359.689951</b>	<b>32.520928</b>
<b>1237663531870191740</b>	<b>196.0</b>	<b>928</b>	<b>123.350008</b>	<b>54.376921</b>
<b>1237663531870191740</b>	<b>131.0</b>	<b>928</b>	<b>123.350008</b>	<b>54.376921</b>
<b>1237663655882064127</b>	<b>135.0</b>	<b>928</b>	<b>112.861145</b>	<b>45.371504</b>
<b>1237663655882064127</b>	<b>225.0</b>	<b>928</b>	<b>112.861145</b>	<b>45.371504</b>
<b>1237663655882064127</b>	<b>159.5</b>	<b>1988</b>	<b>112.861145</b>	<b>45.371504</b>
<b>1237663655882064127</b>	<b>84.8</b>	<b>1988</b>	<b>112.861145</b>	<b>45.371504</b>
<b>1237663789027688497</b>	<b>132.8</b>	<b>2198</b>	<b>115.636595</b>	<b>49.809727</b>
<b>1237663789027688497</b>	<b>236.0</b>	<b>1590</b>	<b>115.636595</b>	<b>49.809727</b>
<b>1237663789027688497</b>	<b>132.5</b>	<b>4524</b>	<b>115.636595</b>	<b>49.809727</b>
<b>1237664089672974631</b>	<b>126.9</b>	<b>1730</b>	<b>51.452472</b>	<b>13.894042</b>
<b>1237664089672974631</b>	<b>36.9</b>	<b>2090</b>	<b>51.452472</b>	<b>13.894042</b>
<b>1237664089672974631</b>	<b>218.4</b>	<b>2982</b>	<b>51.452472</b>	<b>13.894042</b>
<b>1237664089672974631</b>	<b>178.8</b>	<b>2982</b>	<b>51.452472</b>	<b>13.894042</b>
<b>1237665026513371141</b>	<b>147.6</b>	<b>3843</b>	<b>178.359296</b>	<b>35.948268</b>
<b>1237665026513371141</b>	<b>57.6</b>	<b>2650</b>	<b>178.359296</b>	<b>35.948268</b>
<b>1237665129637150884</b>	<b>136.3</b>	<b>1875</b>	<b>235.553803</b>	<b>25.084189</b>
<b>1237665129637150884</b>	<b>226.0</b>	<b>1313</b>	<b>235.553803</b>	<b>25.084189</b>
<b>1237665354556047389</b>	<b>171.4</b>	<b>690</b>	<b>246.846459</b>	<b>57.586793</b>

Continued on next page

Table B.1: The galaxies observed with the Kast Double Spectrograph on the campaign that took place from October 2016 to November 2018. Those used in Chapter 3 are highlighted in bold, with a full table of their properties in Table 3.1. A number of these galaxies were not in the initial observing proposal, but were back-up targets from wider members of the collaboration that the PI was able to observe. (Continued)

SDSS Object ID	PA /°	Exp Time /s	RA /°	Dec /°
<b>1237665354556047389</b>	<b>81.2</b>	<b>695</b>	<b>246.846459</b>	<b>57.586793</b>
<b>1237665356688392316</b>	<b>142.2</b>	<b>765</b>	<b>244.244572</b>	<b>23.132066</b>
<b>1237665356688392316</b>	<b>119.4</b>	<b>765</b>	<b>244.244572</b>	<b>23.132066</b>
<b>1237666076640870510</b>	<b>82.9</b>	<b>675</b>	<b>333.926211</b>	<b>-0.602669</b>
<b>1237666076640870510</b>	<b>173.1</b>	<b>675</b>	<b>333.926211</b>	<b>-0.602669</b>
<b>1237666186186063913</b>	<b>175.5</b>	<b>765</b>	<b>1.620716</b>	<b>37.541469</b>
<b>1237666186186063913</b>	<b>85.5</b>	<b>765</b>	<b>1.620716</b>	<b>37.541469</b>
<b>1237666186186063913</b>	<b>106.7</b>	<b>2120</b>	<b>1.620716</b>	<b>37.541469</b>
<b>1237666186186063913</b>	<b>195.4</b>	<b>2485</b>	<b>1.620716</b>	<b>37.541469</b>
<b>1237666186186063913</b>	<b>215.7</b>	<b>2485</b>	<b>1.620716</b>	<b>37.541469</b>
<b>1237666186186063913</b>	<b>242.1</b>	<b>2485</b>	<b>1.620716</b>	<b>37.541469</b>
<b>1237666245208507953</b>	<b>47.8</b>	<b>788</b>	<b>308.663564</b>	<b>14.569885</b>
<b>1237666245208507953</b>	<b>166.8</b>	<b>765</b>	<b>308.663564</b>	<b>14.569885</b>
<b>1237666245208507953</b>	<b>62.6</b>	<b>3728</b>	<b>308.663564</b>	<b>14.569885</b>
<b>1237666301045113365</b>	<b>75.0</b>	<b>510</b>	<b>302.128719</b>	<b>0.359315</b>
<b>1237666519551705229</b>	<b>113.4</b>	<b>130</b>	<b>88.906766</b>	<b>63.473691</b>
<b>1237666519551705229</b>	<b>105.1</b>	<b>910</b>	<b>88.906766</b>	<b>63.473691</b>
<b>1237666519551705229</b>	<b>195.0</b>	<b>665</b>	<b>88.906766</b>	<b>63.473691</b>
<b>1237666519551705229</b>	<b>189.1</b>	<b>994</b>	<b>88.906766</b>	<b>63.473691</b>
<b>1237666519551705229</b>	<b>168.8</b>	<b>1491</b>	<b>88.906766</b>	<b>63.473691</b>
<b>1237666519551705229</b>	<b>149.8</b>	<b>2982</b>	<b>88.906766</b>	<b>63.473691</b>
1237666661313544194	244.3	928	19.871114	-0.144325

Continued on next page

Table B.1: The galaxies observed with the Kast Double Spectrograph on the campaign that took place from October 2016 to November 2018. Those used in Chapter 3 are highlighted in bold, with a full table of their properties in Table 3.1. A number of these galaxies were not in the initial observing proposal, but were back-up targets from wider members of the collaboration that the PI was able to observe. (Continued)

SDSS Object ID	PA /°	Exp Time /s	RA /°	Dec /°
1237666661313544194	244.5	1188	19.871114	-0.144325
1237666661313544194	153.3	928	19.871114	-0.144325
<b>1237667224460722185</b>	<b>62.4</b>	<b>765</b>	<b>341.242458</b>	<b>-18.380334</b>
<b>1237667225536888887</b>	<b>124.0</b>	<b>765</b>	<b>347.213595</b>	<b>-18.182088</b>
<b>1237667229294788729</b>	<b>177.0</b>	<b>928</b>	<b>28.943249</b>	<b>7.317788</b>
<b>1237667229294788729</b>	<b>267.0</b>	<b>928</b>	<b>28.943249</b>	<b>7.317788</b>
<b>1237667229294788729</b>	<b>251.8</b>	<b>2485</b>	<b>28.943249</b>	<b>7.317788</b>
<b>1237667782815907862</b>	<b>55.3</b>	<b>1458</b>	<b>139.608343</b>	<b>16.305472</b>
<b>1237667782815907862</b>	<b>145.4</b>	<b>1403</b>	<b>139.608343</b>	<b>16.305472</b>
<b>1237667782815907862</b>	<b>257.8</b>	<b>5700</b>	<b>139.608343</b>	<b>16.305472</b>
<b>1237667782815907862</b>	<b>186.5</b>	<b>2614</b>	<b>139.608343</b>	<b>16.305472</b>
1237668631602464967	30.7	765	262.202027	0.798344
1237668757779710211	195.0	750	314.219631	-16.585812
1237668757779710211	122.0	750	314.219631	-16.585812
1237669679572975748	45.1	855	350.192815	6.399637
1237669679572975748	135.1	855	350.192815	6.399637
1237669679572975748	154.6	2485	350.192815	6.399637
1237669679572975748	134.9	2485	350.192815	6.399637
1237669679572975748	253.2	2485	350.192815	6.399637
1237670457507577902	115.0	1313	44.172885	33.704180
1237671067382514425	130.0	938	22.171464	41.009807
<b>1237673075284574990</b>	<b>50.9</b>	<b>180</b>	<b>16.782514</b>	<b>44.063400</b>

Continued on next page

Table B.1: The galaxies observed with the Kast Double Spectrograph on the campaign that took place from October 2016 to November 2018. Those used in Chapter 3 are highlighted in bold, with a full table of their properties in Table 3.1. A number of these galaxies were not in the initial observing proposal, but were back-up targets from wider members of the collaboration that the PI was able to observe. (Continued)

SDSS Object ID	PA /°	Exp Time /s	RA /°	Dec /°
<b>1237673075284574990</b>	<b>230.7</b>	<b>1140</b>	<b>16.782514</b>	<b>44.063400</b>
<b>1237673075284574990</b>	<b>140.8</b>	<b>660</b>	<b>16.782514</b>	<b>44.063400</b>
<b>1237673075284574990</b>	<b>177.6</b>	<b>2485</b>	<b>16.782514</b>	<b>44.063400</b>
<b>1237673075284574990</b>	<b>131.2</b>	<b>2485</b>	<b>16.782514</b>	<b>44.063400</b>
<b>1237673702350520379</b>	<b>203.5</b>	<b>913</b>	<b>32.618439</b>	<b>-11.005399</b>
<b>1237673702350520379</b>	<b>113.4</b>	<b>910</b>	<b>32.618439</b>	<b>-11.005399</b>
<b>1237673738862657863</b>	<b>82.8</b>	<b>665</b>	<b>110.573074</b>	<b>30.513914</b>
<b>1237673738862657863</b>	<b>172.8</b>	<b>665</b>	<b>110.573074</b>	<b>30.513914</b>
<b>1237673738862657863</b>	<b>218.8</b>	<b>2485</b>	<b>110.573074</b>	<b>30.513914</b>
<b>1237676304021127206</b>	<b>129.0</b>	<b>928</b>	<b>71.836353</b>	<b>-5.137248</b>
<b>1237676304021127206</b>	<b>219.0</b>	<b>928</b>	<b>71.836353</b>	<b>-5.137248</b>
1237678438090015153	186.0	2485	39.567417	1.930250
<b>1237678438090080275</b>	<b>55.7</b>	<b>610</b>	<b>39.614244</b>	<b>1.907709</b>
<b>1237678438090080275</b>	<b>235.9</b>	<b>1690</b>	<b>39.614244</b>	<b>1.907709</b>
<b>1237678438090080275</b>	<b>235.7</b>	<b>928</b>	<b>39.614244</b>	<b>1.907709</b>
<b>1237678438090080275</b>	<b>145.7</b>	<b>928</b>	<b>39.614244</b>	<b>1.907709</b>
<b>1237678620101443615</b>	<b>149.6</b>	<b>910</b>	<b>358.241807</b>	<b>3.338287</b>
<b>1237678620101443615</b>	<b>182.6</b>	<b>910</b>	<b>358.241807</b>	<b>3.338287</b>
<b>1237678620101443615</b>	<b>239.2</b>	<b>910</b>	<b>358.241807</b>	<b>3.338287</b>
<b>1237678622240014352</b>	<b>204.6</b>	<b>928</b>	<b>28.980550</b>	<b>4.105639</b>
<b>1237678622240014352</b>	<b>114.7</b>	<b>928</b>	<b>28.980550</b>	<b>4.105639</b>
<b>1237678661426610179</b>	<b>134.8</b>	<b>675</b>	<b>5.904914</b>	<b>4.706249</b>

Continued on next page

Table B.1: The galaxies observed with the Kast Double Spectrograph on the campaign that took place from October 2016 to November 2018. Those used in Chapter 3 are highlighted in bold, with a full table of their properties in Table 3.1. A number of these galaxies were not in the initial observing proposal, but were back-up targets from wider members of the collaboration that the PI was able to observe. (Continued)

SDSS Object ID	PA /°	Exp Time /s	RA /°	Dec /°
<b>1237678661426610179</b>	<b>225.9</b>	<b>675</b>	<b>5.904914</b>	<b>4.706249</b>
<b>1237678777941295144</b>	<b>128.0</b>	<b>900</b>	<b>0.048868</b>	<b>5.388201</b>
<b>1237678777941295144</b>	<b>217.8</b>	<b>900</b>	<b>0.048868</b>	<b>5.388201</b>
<b>1237678859539447915</b>	<b>95.5</b>	<b>855</b>	<b>346.181630</b>	<b>12.202850</b>
<b>1237678859539447915</b>	<b>185.5</b>	<b>855</b>	<b>346.181630</b>	<b>12.202850</b>
<b>1237678859539447915</b>	<b>240.0</b>	<b>4263</b>	<b>346.181630</b>	<b>12.202850</b>
1237678860094734405	97.3	765	29.332716	12.250690
1237678860094734405	241.2	3728	29.332716	12.250690
1237678920733687909	206.6	1320	341.690565	12.493223
1237678920733687909	116.6	1340	341.690565	12.493223
<b>1237679253595226141</b>	<b>180.0</b>	<b>928</b>	<b>28.762540</b>	<b>-5.142845</b>
<b>1237679253595226141</b>	<b>106.7</b>	<b>928</b>	<b>28.762540</b>	<b>-5.142845</b>
<b>1237679253595226141</b>	<b>90.0</b>	<b>928</b>	<b>28.762540</b>	<b>-5.142845</b>
1237679322311032840	102.8	1500	4.157942	-5.740247
1237679322849083511	117.6	938	6.994999	-5.217039
<b>1237679324456288300</b>	<b>209.9</b>	<b>495</b>	<b>359.137203</b>	<b>-4.066707</b>
<b>1237679324456288300</b>	<b>199.3</b>	<b>855</b>	<b>359.137203</b>	<b>-4.066707</b>
<b>1237679324456288300</b>	<b>109.4</b>	<b>360</b>	<b>359.137203</b>	<b>-4.066707</b>
<b>1237679324456288300</b>	<b>211.0</b>	<b>765</b>	<b>359.137203</b>	<b>-4.066707</b>
<b>1237679341105053743</b>	<b>135.0</b>	<b>1193</b>	<b>33.479768</b>	<b>-5.855919</b>
<b>1237679341105053743</b>	<b>238.0</b>	<b>928</b>	<b>33.479768</b>	<b>-5.855919</b>
<b>1237679433444950189</b>	<b>57.3</b>	<b>945</b>	<b>0.584322</b>	<b>-3.629124</b>

Continued on next page

Table B.1: The galaxies observed with the Kast Double Spectrograph on the campaign that took place from October 2016 to November 2018. Those used in Chapter 3 are highlighted in bold, with a full table of their properties in Table 3.1. A number of these galaxies were not in the initial observing proposal, but were back-up targets from wider members of the collaboration that the PI was able to observe. (Continued)

SDSS Object ID	PA /°	Exp Time /s	RA /°	Dec /°
<b>1237679433444950189</b>	<b>147.3</b>	<b>928</b>	<b>0.584322</b>	<b>-3.629124</b>
<b>1237679457600078017</b>	<b>258.0</b>	<b>675</b>	<b>337.581858</b>	<b>16.520197</b>
<b>1237679457600078017</b>	<b>167.9</b>	<b>675</b>	<b>337.581858</b>	<b>16.520197</b>
<b>1237679457600078017</b>	<b>79.2</b>	<b>2050</b>	<b>337.581858</b>	<b>16.520197</b>
<b>1237679457600078017</b>	<b>152.0</b>	<b>2253</b>	<b>337.581858</b>	<b>16.520197</b>
<b>1237679457600078017</b>	<b>147.8</b>	<b>3728</b>	<b>337.581858</b>	<b>16.520197</b>
1237679479084810289	148.3	938	9.633795	23.613414
<b>1237679504855597318</b>	<b>36.9</b>	<b>1230</b>	<b>359.615917</b>	<b>20.966290</b>
<b>1237679504855597318</b>	<b>126.6</b>	<b>1220</b>	<b>359.615917</b>	<b>20.966290</b>
<b>1237679504855597318</b>	<b>193.5</b>	<b>2485</b>	<b>359.615917</b>	<b>20.966290</b>
<b>1237679562834968871</b>	<b>141.8</b>	<b>765</b>	<b>14.624071</b>	<b>26.654110</b>
<b>1237679997698965522</b>	<b>195.2</b>	<b>855</b>	<b>344.508073</b>	<b>-2.329121</b>
<b>1237679997698965522</b>	<b>105.2</b>	<b>855</b>	<b>344.508073</b>	<b>-2.329121</b>
<b>1237680045474709585</b>	<b>207.5</b>	<b>1960</b>	<b>4.257468</b>	<b>8.079234</b>
<b>1237680045474709585</b>	<b>117.5</b>	<b>1640</b>	<b>4.257468</b>	<b>8.079234</b>
1237680066952036680	118.4	1875	330.745877	-3.303304
<b>1237680071783612535</b>	<b>139.5</b>	<b>928</b>	<b>14.031974</b>	<b>25.801315</b>
<b>1237680071783612535</b>	<b>228.8</b>	<b>928</b>	<b>14.031974</b>	<b>25.801315</b>
<b>1237680071783612535</b>	<b>232.5</b>	<b>3728</b>	<b>14.031974</b>	<b>25.801315</b>
1237680245200453741	220.8	938	352.020185	18.531438
1237680247887954176	163.8	2485	359.587757	20.998178
1237680249489457373	236.0	938	35.646745	25.137420

Continued on next page

Table B.1: The galaxies observed with the Kast Double Spectrograph on the campaign that took place from October 2016 to November 2018. Those used in Chapter 3 are highlighted in bold, with a full table of their properties in Table 3.1. A number of these galaxies were not in the initial observing proposal, but were back-up targets from wider members of the collaboration that the PI was able to observe. (Continued)

SDSS Object ID	PA /°	Exp Time /s	RA /°	Dec /°
<b>1237680529738825995</b>	<b>186.8</b>	<b>1705</b>	<b>339.976780</b>	<b>27.409289</b>
<b>1237680529738825995</b>	<b>96.8</b>	<b>1340</b>	<b>339.976780</b>	<b>27.409289</b>
<b>1237680529738825995</b>	<b>237.9</b>	<b>2485</b>	<b>339.976780</b>	<b>27.409289</b>
<b>1237680529738825995</b>	<b>172.4</b>	<b>2485</b>	<b>339.976780</b>	<b>27.409289</b>
<b>1237680529738825995</b>	<b>86.0</b>	<b>2485</b>	<b>339.976780</b>	<b>27.409289</b>
DRAGN J-113+0106	154.3	480	18.421417	1.084972
DRAGN J-113+0106	77.9	1225	18.421417	1.084972
DRAGN J-113+0106	154.3	1470	18.421417	1.084972
J012406.59+083806.9	254.0	2243	21.027458	8.635250
J162147.78+543921.9	174.8	928	245.449083	54.656083
J162147.78+543921.9	224.0	2115	245.449083	54.656083
J234811.86-001147.8	170.0	7590	357.049417	-0.196611
PG2213-006B	207.2	345	334.091625	-0.364222
QSO-J1612+5946	74.8	720	243.102333	59.769389
UGC 11700	201.4	300	318.102875	11.408683
UGC 11700	201.2	1500	318.102875	11.408683
UGC 11700	111.3	1500	318.102875	11.408683
UGC 11700	201.0	928	318.102875	11.408683
UGC 11700	110.0	928	318.102875	11.408683
Voorwerp41	194.0	1875	357.172833	2.239917
Voorwerp75	131.2	2813	10.220125	-7.702611
Voorwerp76	140.3	2813	10.666292	30.297556

Continued on next page

Table B.1: The galaxies observed with the Kast Double Spectrograph on the campaign that took place from October 2016 to November 2018. Those used in Chapter 3 are highlighted in bold, with a full table of their properties in Table 3.1. A number of these galaxies were not in the initial observing proposal, but were back-up targets from wider members of the collaboration that the PI was able to observe. (Continued)

SDSS Object ID	PA /°	Exp Time /s	RA /°	Dec /°
Voorwerp76	217.2	938	10.666292	30.297556
Voorwerp88	131.0	750	328.108417	-8.173722
Voorwerp88	220.8	2438	328.108417	-8.173722
Voorwerp88	104.0	938	328.108417	-8.173722
WLR3	213.1	1050	106.845875	59.457250
WLR4	195.7	900	106.893708	50.489500

Table B.2: The standard stars used throughout the campaign that took place from October 2016 to November 2018. Each source in Table B.1 was matched to a standard star that was taken on the same night and was close to the source in RA and Dec.

Object	PA/°	Slit Width /"	Exp Time/s	RA/°	Dec/°
BD+262606	49.3	2.0	210	222.259667	25.702556
BD+262606	61.1	2.0	245	222.259667	25.702556
BD+262606	56.3	2.0	255	222.259667	25.702556
BD+284211	114.7	2.0	175	327.795833	28.863861
BD+284211	122.8	2.0	160	327.795833	28.863861
BD+284211	65.2	2.0	225	327.795833	28.863861
BD+284211	121.3	2.0	135	327.795833	28.863861
BD+284211	33.3	2.0	135	327.795833	28.863861
BD+284211	50.9	2.0	180	327.795833	28.863861

Continued on next page

Table B.2: The standard stars used throughout the campaign that took place from October 2016 to November 2018. Each source in Table B.1 was matched to a standard star that was taken on the same night and was close to the source in RA and Dec. (Continued)

Object	PA/°	Slit Width /"	Exp Time/s	RA/°	Dec/°
BD+284211	239.2	2.0	255	327.795833	28.863861
BD+284211	128.5	3.0	240	327.795833	28.863861
BD+284211	128.5	2.0	180	327.795833	28.863861
BD+284211	180.0	3.0	263	327.795833	28.863861
BD+284211	130.0	3.0	263	327.795833	28.863861
BD+284211	211.0	3.0	263	327.795833	28.863861
BD+284211	140.0	1.5	263	327.795833	28.863861
BD+284211	140.0	1.5	188	327.795833	28.863861
BD+284211	116.0	2.0	320	327.795833	28.863861
BD+284211	174.4	2.0	200	327.795833	28.863861
BD+284211	177.0	1.5	210	327.795833	28.863861
BD+284211	140.0	2.0	418	327.795833	28.863861
BD+332642	46.1	2.0	240	237.999625	32.948583
BD+332642	71.4	2.0	135	237.999625	32.948583
BD+332642	67.6	2.0	150	237.999625	32.948583
BD+332642	90.0	2.0	180	237.999625	32.948583
BD+332642	64.5	3.0	228	237.999625	32.948583
BD+332642	65.0	1.5	180	237.999625	32.948583
BD+332642	71.0	1.5	270	237.999625	32.948583
BD+332642	200.0	1.5	188	237.999625	32.948583
BD+332642	71.0	1.5	188	237.999625	32.948583
BD+332642	40.9	1.5	188	237.999625	32.948583
BD+332642	41.2	1.5	188	237.999625	32.948583
BD+332642	70.1	1.5	180	237.999625	32.948583

Continued on next page

Table B.2: The standard stars used throughout the campaign that took place from October 2016 to November 2018. Each source in Table B.1 was matched to a standard star that was taken on the same night and was close to the source in RA and Dec. (Continued)

Object	PA/°	Slit Width /"	Exp Time/s	RA/°	Dec/°
BD+332642	75.0	3.0	188	237.999625	32.948583
BD+332642	72.0	3.0	225	237.999625	32.948583
Feige 110	159.5	2.0	283	349.993375	-5.165694
Feige 110	173.7	2.0	270	349.993375	-5.165694
Feige 110	167.8	2.0	270	349.993375	-5.165694
Feige 110	181.0	2.0	270	349.993375	-5.165694
Feige 110	180.2	2.0	225	349.993375	-5.165694
Feige 110	210.0	3.0	180	349.993375	-5.165694
Feige 110	180.0	3.0	263	349.993375	-5.165694
Feige 110	170.0	2.0	263	349.993375	-5.165694
Feige 110	174.0	3.0	188	349.993375	-5.165694
Feige 110	150.0	3.0	188	349.993375	-5.165694
Feige 34	100.0	3.0	263	159.902792	43.102583
Feige 34	95.6	3.0	263	159.902792	43.102583
Feige 34	84.0	3.0	150	159.902792	43.102583
Feige 34	110.0	3.0	263	159.902792	43.102583
Feige 34	95.0	3.0	928	159.902792	43.102583
Feige 34	108.2	3.0	315	159.902792	43.102583
G191B2B	52.0	2.0	140	76.377500	52.831694
G191B2B	210.0	2.0	245	76.377500	52.831694
G191B2B	180.1	2.0	245	76.377500	52.831694
G191B2B	190.0	3.0	263	76.377500	52.831694
G191B2B	210.0	3.0	263	76.377500	52.831694
G191B2B	212.1	2.0	418	76.377500	52.831694

Continued on next page

Table B.2: The standard stars used throughout the campaign that took place from October 2016 to November 2018. Each source in Table B.1 was matched to a standard star that was taken on the same night and was close to the source in RA and Dec. (Continued)

Object	PA/°	Slit Width /"	Exp Time/s	RA/°	Dec/°
G191B2B	127.2	2.0	418	76.377500	52.831694
G193-74	80.0	3.0	263	118.364042	52.493222
G193-74	230.0	3.0	263	118.364042	52.493222
G193-74	216.9	3.0	430	118.364042	52.493222
G193-74	140.0	2.0	793	118.364042	52.493222
G193-74	90.0	2.0	793	118.364042	52.493222
G24-9	200.8	3.0	473	303.483042	6.715278
G24-9	201.2	2.0	338	303.483042	6.715278
GD 248	191.4	2.0	340	351.527792	16.005833
GD 248	60.5	2.0	338	351.527792	16.005833
GD 248	271.8	2.0	338	351.527792	16.005833
GD 248	222.8	2.0	263	351.527792	16.005833
GD 248	231.7	2.0	263	351.527792	16.005833
GD 248	231.7	3.0	263	351.527792	16.005833
GD 248	205.0	3.0	263	351.527792	16.005833
GD 248	227.7	3.0	263	351.527792	16.005833
GD 248	198.8	1.5	338	351.527792	16.005833
GD 248	229.7	1.5	413	351.527792	16.005833
GD 248	139.8	1.5	188	351.527792	16.005833
GD 248	33.6	1.5	338	351.527792	16.005833
GD 248	200.1	3.0	338	351.527792	16.005833
GD 248	160.0	2.0	338	351.527792	16.005833
GD 248	160.0	3.0	338	351.527792	16.005833
GD 248	215.0	2.0	270	351.527792	16.005833

Continued on next page

Table B.2: The standard stars used throughout the campaign that took place from October 2016 to November 2018. Each source in Table B.1 was matched to a standard star that was taken on the same night and was close to the source in RA and Dec. (Continued)

Object	PA/°	Slit Width /"	Exp Time/s	RA/°	Dec/°
GD 248	215.0	3.0	270	351.527792	16.005833
GD 248	179.7	2.0	268	351.527792	16.005833
GD 248	240.0	2.0	268	351.527792	16.005833
GD 248	130.0	2.0	268	351.527792	16.005833
GD 248	192.6	2.0	418	351.527792	16.005833
GD 248	189.0	2.0	418	351.527792	16.005833
GD 248	233.0	2.0	418	351.527792	16.005833
GD 248	145.2	3.0	248	351.527792	16.005833
GD 248	180.0	3.0	368	351.527792	16.005833
GD 248	185.0	3.0	45	351.527792	16.005833
GD 248	180.1	1.5	263	351.527792	16.005833
GD 248	215.3	1.5	263	351.527792	16.005833
GD 248	208.0	1.5	263	351.527792	16.005833
HD 157881	197.7	2.0	90	261.438292	2.111361
HD 183143	227.0	1.5	49	291.860917	18.295806
HD 19445	130.0	2.0	26	47.106708	26.330861
HD 19445	162.3	3.0	51	47.106708	26.330861
HD 19445	61.9	3.0	85	47.106708	26.330861
HD 84937	152.2	2.0	268	147.233250	13.744806
HD 84937	128.0	3.0	165	147.233250	13.744806
HD 84937	130.0	3.0	210	147.233250	13.744806
Hip 11099	246.0	2.0	207	35.726042	41.480083
Hip 114520	178.9	3.0	85	347.934292	8.720139
Hip 114520	195.2	3.0	20	347.934292	8.720139

Continued on next page

Table B.2: The standard stars used throughout the campaign that took place from October 2016 to November 2018. Each source in Table B.1 was matched to a standard star that was taken on the same night and was close to the source in RA and Dec. (Continued)

Object	PA/°	Slit Width /"	Exp Time/s	RA/°	Dec/°
Hip 30393	190.0	2.0	268	95.868792	20.392194
Hip 30393	179.9	2.0	268	95.868792	20.392194
Hip 30393	179.9	3.0	268	95.868792	20.392194
Hip 30393	227.0	3.0	268	95.868792	20.392194
Hip 85317	268.0	3.0	98	261.520042	58.652000
Hip 85317	90.0	2.0	85	261.520042	58.652000
Hip 85317	175.0	2.0	278	261.520042	58.652000
Hip 85317	98.4	2.0	191	261.520042	58.652000
HZ 4	83.7	2.0	380	58.840458	9.788389
HZ 4	140.2	2.0	260	58.840458	9.788389
HZ 4	150.1	2.0	315	58.840458	9.788389
HZ 4	154.2	3.0	180	58.840458	9.788389
HZ 4	160.4	3.0	225	58.840458	9.788389
HZ 4	175.5	1.5	238	58.840458	9.788389
HZ 4	145.7	3.0	375	58.840458	9.788389
HZ 4	214.0	3.0	293	58.840458	9.788389
HZ 4	163.0	3.0	263	58.840458	9.788389
KIC 8462852	100.0	3.0	165	301.564583	44.456972
KIC 8462852	100.1	2.0	165	301.564583	44.456972
KIC 8462852	68.5	2.0	263	301.564583	44.456972
KIC 8462852	84.7	3.0	330	301.564583	44.456972
KIC 8462852	105.0	1.5	218	301.564583	44.456972

# Appendix C

## Chapter 3

### C.1 SDSS thumbnails

Figure C.1 shows the full AGNDISKS sample imaged in SDSS, with the scale bar in each image representing 10 arcsec. The disk-dominated nature of the galaxies can be seen clearly, as well as a large-scale galactic bar in some images.

### C.2 *HST* thumbnails

Figure C.2 shows the galaxies for which we have *HST* data. Their position in the grid corresponds to their SDSS counterpart in Figure C.1, however their orientation does not. The scale bar in these images corresponds to 5 arcsec. The grey blank squares show galaxies for which we do not have *HST* photometric data.

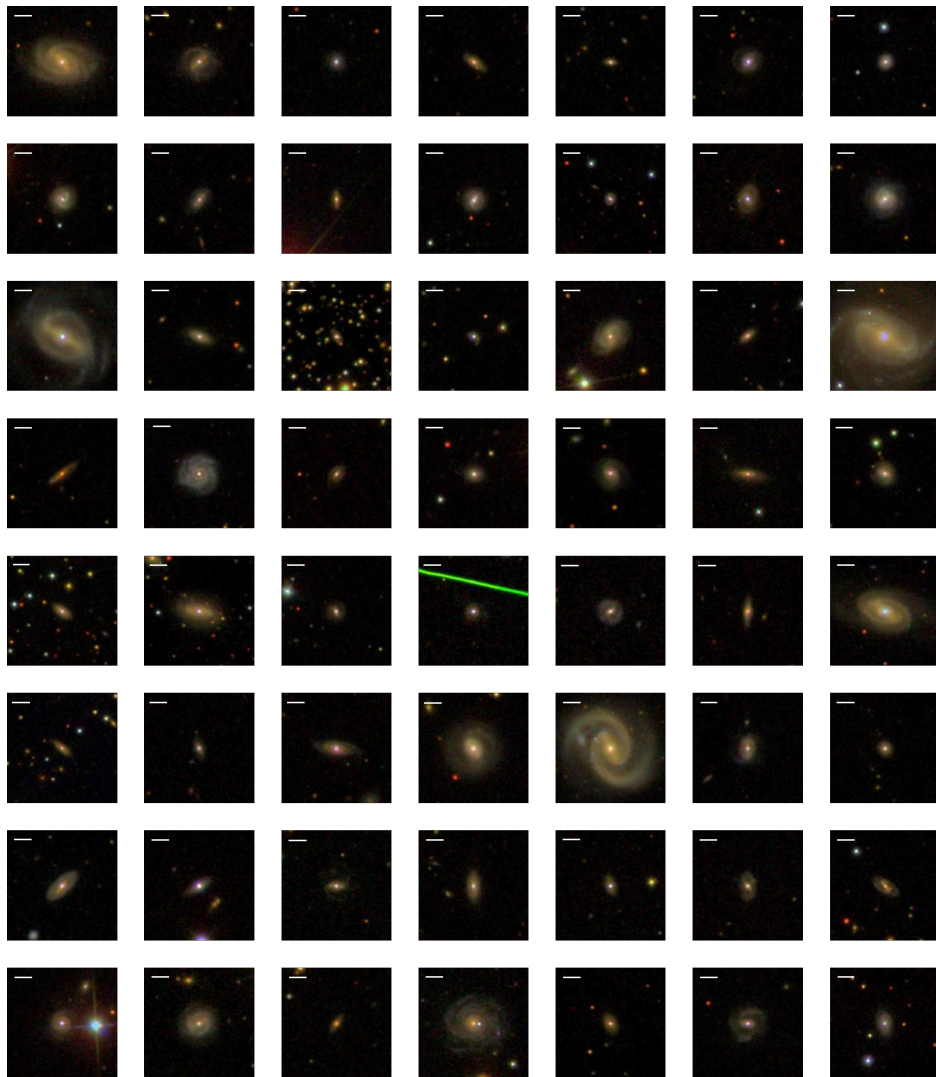


**Figure C.1:** SDSS postage stamps of all galaxies in AGNDISKS, including those that are constrained only by an upper limit in  $H\alpha$  and those with values. Images are taken from SDSS DR8 (Aihara et al., 2011). The scale bar in each upper left corner represents 10 arcsec. The position angles of the galaxies do not correspond to those in Figure C.2.

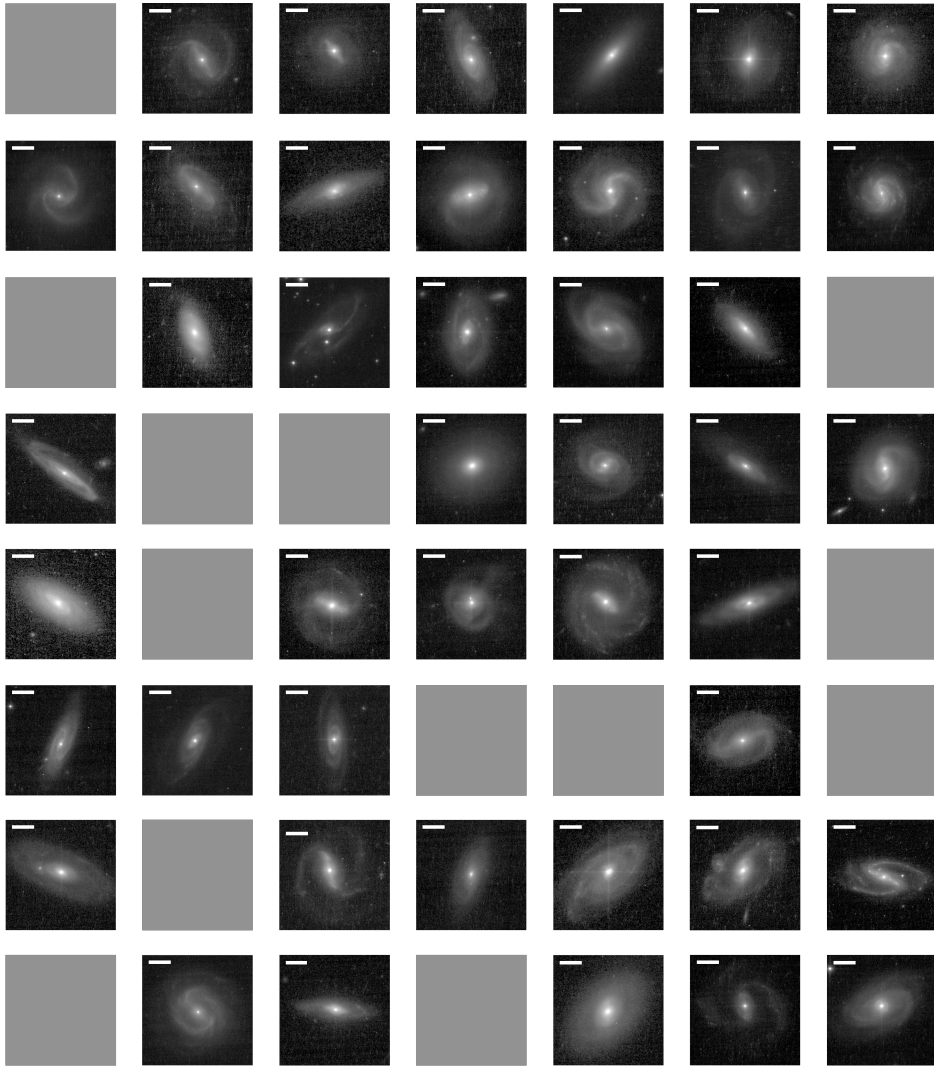


**Figure C.2:** *HST* postage stamps of the galaxies in AGNDISKS that have been imaged in *HST*. The galaxies' positions correspond to the galaxies in Figure C.1, and so the grey squares represent galaxies that have not yet been imaged with *HST*. The white scale bar in each top left corner represents 5 arcsec. The position angles of the galaxies do not correspond to those in Figure C.1.

# Appendix D

## Chapter 4

### D.1 Subsample Counts

Tab. [D.1](#) presents the full set of number counts of all subsamples in this work. While our analysis is confined to the volume-limited sample, we also present numbers for the full set of GZD classified galaxies with ancillary data presented in the MPA-JHU and NYU-VAGC catalogues.

### D.2 Full stellar mass and colour distributions

Figure [D.1](#) shows an identical plot to that in Figure [4.4](#), with the addition of the distributions in mass and colour for weakly barred galaxies for completeness.

**Table D.1:** Full breakdown of the number of galaxies in each activity class, and each bar category, both in the volume limited sample, and the total sample.

Subsample Counts		
	Total	In Volume Limit
Is Disk	112699	48871
Is Undetermined	218101	25004
Is Uncertain	124990	29355
Is Star-forming	280867	86917
Is Composite	75872	30540
Is LINER	49721	23152
Is AGN	37651	13406
Is Disk and:		
Is Undetermined	2652	712
Is Uncertain	11011	2518
Is Star-forming	66335	28807
Is Composite	17754	8669
Is LINER	7426	4843
Is AGN	6639	3164
Is Unbarred Disk and:		
Is Undetermined	1377	350
Is Uncertain	5432	1234
Is Star-forming	42045	18829
Is Composite	7051	3628
Is LINER	3086	2003
Is AGN	2455	1238
Is Weak Barred Disk and:		
Is Undetermined	860	212
Is Uncertain	4078	844
Is Star-forming	19791	7903
Is Composite	6545	2914
Is LINER	2405	1454
Is AGN	2504	1051
Is Strong Barred Disk and:		
Is Undetermined	415	150
Is Uncertain	1501	440
Is Star-forming	4499	2075
Is Composite	4158	2127
Is LINER	1935	1386
Is AGN	1680	875

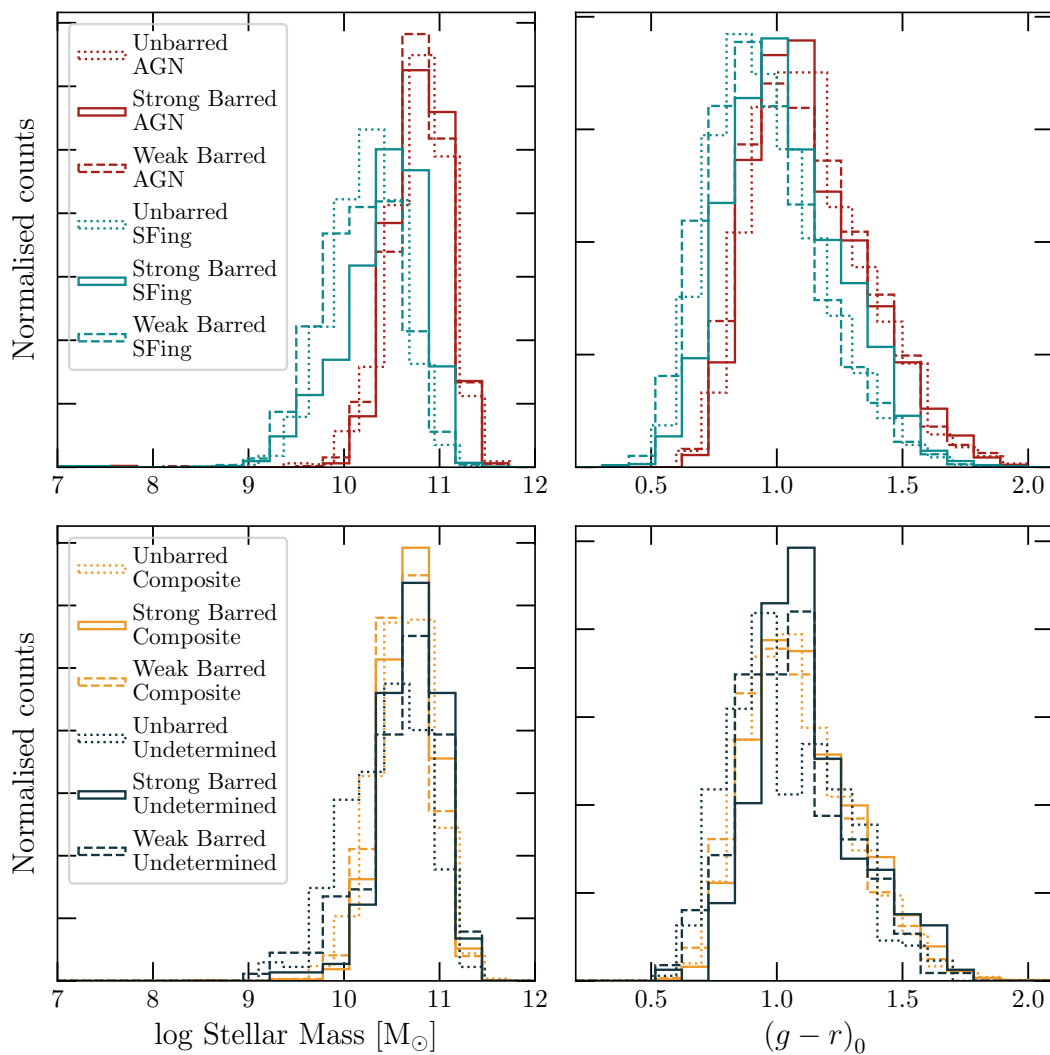


**Figure D.1:** The distributions in stellar mass and  $(g-r)_0$  colour for a variety of subsamples, with strongly barred galaxies in solid lines, unbarred in dotted lines and weakly barred in dashed lines. AGN are in teal, star-forming in red, composite in orange and undetermined in navy blue.

# References

- Abazajian K. N., et al., 2009, [ApJS](#), 182, 543
- Agertz O., Teyssier R., Moore B., 2011, [MNRAS](#), 410, 1391
- Agostino C. J., Salim S., 2019, [ApJ](#), 876, 12
- Aihara H., et al., 2011, [ApJS](#), 193, 29
- Aird J., et al., 2010, [MNRAS](#), 401, 2531
- Aird J., et al., 2012, [ApJ](#), 746, 90
- Aird J., Coil A. L., Georgakakis A., 2019, [MNRAS](#), 484, 4360
- Alonso M. S., Coldwell G., Lambas D. G., 2013, [A&A](#), 549, A141
- Alonso S., Coldwell G., Duplancic F., Mesa V., Lambas D. G., 2018, [A&A](#), 618, A149
- Ann H. B., Thakur P., 2005, [ApJ](#), 620, 197
- Antonucci R., 1993, [ARAA](#), 31, 473
- Assef R. J., Stern D., Noirot G., Jun H. D., Cutri R. M., Eisenhardt P. R. M., 2018, [ApJS](#), 234, 23
- Astropy Collaboration et al., 2013, [A&A](#), 558, A33
- Astropy Collaboration et al., 2018, [AJ](#), 156, 123
- Astropy Collaboration et al., 2022, [ApJ](#), 935, 167

- Athanassoula E., 1992, *MNRAS*, 259, 345
- Athanassoula E., 2003, *MNRAS*, 341, 1179
- Athanassoula E., Machado R. E. G., Rodionov S. A., 2013, *MNRAS*, 429, 1949
- Baillard A., et al., 2011, *A&A*, 532, A74
- Baldry I. K., Glazebrook K., Brinkmann J., Ivezić Ž., Lupton R. H., Nichol R. C., Szalay A. S., 2004, *ApJ*, 600, 681
- Baldry I. K., Balogh M. L., Bower R. G., Glazebrook K., Nichol R. C., Bamford S. P., Budavari T., 2006, *MNRAS*, 373, 469
- Baldwin J. A., Phillips M. M., Terlevich R., 1981, *PASP*, 93, 5
- Ball N. M., Loveday J., Brunner R. J., 2008, *MNRAS*, 383, 907
- Bamford S. P., et al., 2009, *MNRAS*, 393, 1324
- Barazza F. D., Jogee S., Marinova I., 2008, *ApJ*, 675, 1194
- Barnes J. E., 1989, *Nature*, 338, 123
- Barnes J. E., 1992, *ApJ*, 393, 484
- Barnes J. E., Hernquist L. E., 1991, *ApJ*, 370, L65
- Beckmann R. S., et al., 2024, *MNRAS*, 527, 10867
- Bell E. F., Monachesi A., Harmsen B., de Jong R. S., Bailin J., Radburn-Smith D. J., D'Souza R., Holwerda B. W., 2017, *ApJ*, 837, L8
- Berti E., Volonteri M., 2008, *ApJ*, 684, 822
- Binney J., Merrifield M., 1998, *Galactic Astronomy*
- Bizzocchi L., et al., 2014, *ApJ*, 782, 22
- Blanton M. R., et al., 2005, *AJ*, 129, 2562
- Brammer G. B., et al., 2009, *ApJ*, 706, L173

- 
- Brinchmann J., Charlot S., White S. D. M., Tremonti C., Kauffmann G., Heckman T., Brinkmann J., 2004, *MNRAS*, **351**, 1151
- Brusa M., et al., 2009, *A&A*, **507**, 1277
- Bundy K., et al., 2010, *ApJ*, **719**, 1969
- Bustamante S., Springel V., 2019, *MNRAS*, **490**, 4133
- Buta R. J., 2013, in Oswalt T. D., Keel W. C., eds, , Vol. 6, Planets, Stars and Stellar Systems. Volume 6: Extragalactic Astronomy and Cosmology. p. 1, [doi:10.1007/978-94-007-5609-0\\_1](https://doi.org/10.1007/978-94-007-5609-0_1)
- Buta R. J., Corwin H. G., Odewahn S. C., 2007, The de Vaucouleurs Atlas of Galaxies
- Calzetti D., Armus L., Bohlin R. C., Kinney A. L., Koornneef J., Storchi-Bergmann T., 2000, *ApJ*, **533**, 682
- Cameron E., 2011, *PASA*, **28**, 128
- Cameron E., et al., 2010, *MNRAS*, **409**, 346
- Casteels K. R. V., et al., 2013, *MNRAS*, **429**, 1051
- Cheung E., et al., 2013, *ApJ*, **779**, 162
- Cheung E., et al., 2015, *MNRAS*, **447**, 506
- Ciotti L., Ostriker J. P., 2012, AGN Feedback in Elliptical Galaxies: Numerical Simulations. Springer New York, New York, NY, pp 83–120, [doi:10.1007/978-1-4614-0580-1\\_4](https://doi.org/10.1007/978-1-4614-0580-1_4), [https://doi.org/10.1007/978-1-4614-0580-1\\_4](https://doi.org/10.1007/978-1-4614-0580-1_4)
- Ciotti L., D’Ercole A., Pellegrini S., Renzini A., 1991, *ApJ*, **376**, 380
- Ciotti L., Ostriker J. P., Proga D., 2010, *ApJ*, **717**, 708
- Cisternas M., et al., 2011, *ApJ*, **741**, L11
- Cisternas M., Sheth K., Salvato M., Knapen J. H., Civano F., Santini P., 2015, *ApJ*, **802**, 137

- 
- Coccatto L., Fabricius M. H., Saglia R. P., Bender R., Erwin P., Drory N., Morelli L., 2018, *MNRAS*, **477**, 1958
- Coelho P., Gadotti D. A., 2011, *ApJ*, **743**, L13
- Coldwell G. V., Alonso S., Duplancic F., Mesa V., 2018, *MNRAS*, **476**, 2457
- Combes F., 2009, in Jogee S., Marinova I., Hao L., Blanc G. A., eds, *Astronomical Society of the Pacific Conference Series Vol. 419, Galaxy Evolution: Emerging Insights and Future Challenges*. p. 31 ([arXiv:0901.0178](https://arxiv.org/abs/0901.0178))
- Conselice C. J., 2003, *ApJS*, **147**, 1
- DESI Collaboration et al., 2016, *arXiv e-prints*, p. [arXiv:1611.00036](https://arxiv.org/abs/1611.00036)
- DESI Collaboration et al., 2022, *AJ*, **164**, 207
- D’Onghia E., Burkert A., Murante G., Khochfar S., 2006, *MNRAS*, **372**, 1525
- D’Onghia E., Vogelsberger M., Hernquist L., 2013, *ApJ*, **766**, 34
- Davé R., Anglés-Alcázar D., Narayanan D., Li Q., Rafieferantsoa M. H., Appleby S., 2019, *MNRAS*, **486**, 2827
- Davies R. L., Illingworth G., 1983, *ApJ*, **266**, 516
- Davies R. I., Müller Sánchez F., Genzel R., Tacconi L. J., Hicks E. K. S., Friedrich S., Sternberg A., 2007, *ApJ*, **671**, 1388
- Davies R. I., Maciejewski W., Hicks E. K. S., Tacconi L. J., Genzel R., Engel H., 2009, *ApJ*, **702**, 114
- Deller A. T., Middelberg E., 2014, *AJ*, **147**, 14
- Delvecchio I., et al., 2014, *MNRAS*, **439**, 2736
- Dey A., et al., 2019, *AJ*, **157**, 168
- Di Matteo T., Springel V., Hernquist L., 2005, *Nature*, **433**, 604
- Domínguez A., et al., 2013, *ApJ*, **763**, 145

- Donner K. J., Thomasson M., 1994, *A&A*, **290**, 785
- Dotti M., Colpi M., Pallini S., Perego A., Volonteri M., 2013, *ApJ*, **762**, 68
- Drory N., Fisher D. B., 2007, *ApJ*, **664**, 640
- Dubois Y., Volonteri M., Silk J., 2014, *MNRAS*, **440**, 1590
- Edelson R., Malkan M., 2012, *ApJ*, **751**, 52
- Efstathiou G., Lake G., Negroponte J., 1982, *MNRAS*, **199**, 1069
- Elmegreen D. M., Sundin M., Elmegreen B., Sundelius B., 1991, *A&A*, **244**, 52
- Erwin P., 2018, *MNRAS*, **474**, 5372
- Eskridge P. B., et al., 2000, *AJ*, **119**, 536
- Fabian A., 2012, *ARAA*, **50**, 455
- Falcón-Barroso J., Lyubenova M., van de Ven G., 2015, in Cappellari M., Courteau S., eds, Vol. 311, *Galaxy Masses as Constraints of Formation Models*. pp 78–81 ([arXiv:1409.7786](https://arxiv.org/abs/1409.7786)), [doi:10.1017/S1743921315003439](https://doi.org/10.1017/S1743921315003439)
- Fanali R., Dotti M., Fiacconi D., Haardt F., 2015, *MNRAS*, **454**, 3641
- Fisher D. B., Drory N., 2008, *AJ*, **136**, 773
- Friedli D., Benz W., 1993, *A&A*, **268**, 65
- Gadotti D. A., 2009, *MNRAS*, **393**, 1531
- Galloway M. A., et al., 2015, *MNRAS*, **448**, 3442
- Gargiulo I. D., Cora S. A., Vega-Martínez C. A., Gonzalez O. A., Zoccali M., González R., Ruiz A. N., Padilla N. D., 2017, *MNRAS*, **472**, 4133
- Garland I. L., et al., 2023, *MNRAS*, **522**, 211
- George K., Joseph P., Mondal C., Subramanian S., Subramaniam A., Paul K. T., 2019, *A&A*, **621**, L4

- 
- Géron T., Smethurst R. J., Lintott C., Kruk S., Masters K. L., Simmons B., Stark D. V., 2021, *MNRAS*, **507**, 4389
- Géron T., et al., 2023, *MNRAS*, **521**, 1775
- Glikman E., Simmons B., Maily M., Schawinski K., Urry C. M., Lacy M., 2015, *ApJ*, **806**, 218
- Goodwin S. P., Gribbin J., Hendry M. A., 1998, *The Observatory*, **118**, 201
- Goulding A. D., et al., 2017, *ApJ*, **843**, 135
- Governato F., Willman B., Mayer L., Brooks A., Stinson G., Valenzuela O., Wadsley J., Quinn T., 2007, *MNRAS*, **374**, 1479
- Greene J. E., et al., 2010, *ApJ*, **721**, 26
- Häring N., Rix H.-W., 2004, *ApJ*, **604**, L89
- Harris C. R., et al., 2020, *Nature*, **585**, 357
- Harrison C. M., 2017, *Nature Astronomy*, **1**, 0165
- Hawarden T. G., Mountain C. M., Leggett S. K., Puxley P. J., 1986, *MNRAS*, **221**, 41P
- Heckman T. M., 1980, *A&A*, **87**, 152
- Heckman T. M., Best P. N., 2014, *ARAA*, **52**, 589
- Hinshaw G., et al., 2013, *ApJS*, **208**, 19
- Ho L. C., Filippenko A. V., Sargent W. L. W., 1997, *ApJ*, **487**, 591
- Hopkins P. F., Hernquist L., 2006, *ApJS*, **166**, 1
- Hubble E. P., 1926, *ApJ*, **64**, 321
- Hubble E. P., 1930, *ApJ*, **71**, 231
- Hubble E. P., 1936, *Realm of the Nebulae*

- 
- Hudson M. J., Stevenson J. B., Smith R. J., Wegner G. A., Lucey J. R., Simard L., 2010, [MNRAS](#), **409**, 405
- Huertas-Company M., Aguerri J. A. L., Bernardi M., Mei S., Sánchez Almeida J., 2011, [A&A](#), **525**, A157
- Hunt J. A. S., Hong J., Bovy J., Kawata D., Grand R. J. J., 2018, [MNRAS](#), **481**, 3794
- Hunter J. D., 2007, [Computing in Science and Engineering](#), **9**, 90
- Ishibashi W., Fabian A. C., 2012, [MNRAS](#), **427**, 2998
- Ivezić Ž., et al., 2019, [ApJ](#), **873**, 111
- Jarvis B. J., Freeman K. C., 1985, [ApJ](#), **295**, 314
- Jiang Y.-F., Greene J. E., Ho L. C., Xiao T., Barth A. J., 2011, [ApJ](#), **742**, 68
- Jones M. L., Hickox R. C., Black C. S., Hainline K. N., DiPompeo M. A., Goulding A. D., 2016, [ApJ](#), **826**, 12
- Jordan Raddick M., et al., 2013, [Astronomy Education Review](#), **12**, 010106
- Joye W. A., Mandel E., 2003, in Payne H. E., Jedrzejewski R. I., Hook R. N., eds, *Astronomical Society of the Pacific Conference Series Vol. 295, Astronomical Data Analysis Software and Systems XII*. p. 489
- Kataria S. K., Vivek M., 2024, [MNRAS](#), **527**, 3366
- Kauffmann G., et al., 2003a, [MNRAS](#), **341**, 33
- Kauffmann G., et al., 2003b, [MNRAS](#), **341**, 54
- Kauffmann G., et al., 2003c, [MNRAS](#), **346**, 1055
- Kennicutt Robert C. J., Tamblyn P., Congdon C. E., 1994, [ApJ](#), **435**, 22
- Kereš D., Katz N., Weinberg D. H., Davé R., 2005, [MNRAS](#), **363**, 2

- 
- Kewley L. J., Dopita M. A., Sutherland R. S., Heisler C. A., Trevena J., 2001, [ApJ](#), 556, 121
- Kewley L. J., Groves B., Kauffmann G., Heckman T., 2006, [MNRAS](#), 372, 961
- Knapen J. H., Beckman J. E., Heller C. H., Shlosman I., de Jong R. S., 1995, [ApJ](#), 454, 623
- Knapen J. H., Shlosman I., Peletier R. F., 2000, [ApJ](#), 529, 93
- Kocevski D. D., et al., 2012, [ApJ](#), 744, 148
- Kolmogorov A., 1933, *Inst. Ital. Attuari, Giorn.*, 4, 83
- Kormendy J., Ho L. C., 2013, [ARAA](#), 51, 511
- Kormendy J., Illingworth G., 1982, [ApJ](#), 256, 460
- Kormendy J., Kennicutt Robert C. J., 2004, [ARAA](#), 42, 603
- Kormendy J., Cornell M. E., Block D. L., Knapen J. H., Allard E. L., 2006, [ApJ](#), 642, 765
- Kraljic K., Bournaud F., Martig M., 2012, [ApJ](#), 757, 60
- Kruk S. J., et al., 2017, [MNRAS](#), 469, 3363
- Kruk S. J., et al., 2018, [MNRAS](#), 473, 4731
- Laine S., Shlosman I., Knapen J. H., Peletier R. F., 2002, [ApJ](#), 567, 97
- Lang M., Holley-Bockelmann K., Sinha M., 2014, [ApJ](#), 790, L33
- Laurikainen E., Salo H., Buta R., 2004, [ApJ](#), 607, 103
- Le Conte Z. A., et al., 2024, [MNRAS](#), 530, 1984
- Lee G.-H., Woo J.-H., Lee M. G., Hwang H. S., Lee J. C., Sohn J., Lee J. H., 2012, [ApJ](#), 750, 141

- 
- Lick-Observatory 2021, Shane Telescope – lickobservatory.org, <https://www.lickobservatory.org/explore/research-telescopes/shane-telescope/>
- Lin L.-H., Wang H.-H., Hsieh P.-Y., Taam R. E., Yang C.-C., Yen D. C. C., 2013, *ApJ*, 771, 8
- Lintott C. J., et al., 2008, *MNRAS*, 389, 1179
- Lintott C., et al., 2011, *MNRAS*, 410, 166
- Lokas E. L., 2018, *ApJ*, 857, 6
- Lokas E. L., 2022, *A&A*, 668, L3
- Maciejewski W., 2004, *MNRAS*, 354, 892
- Maciejewski W., Teuben P. J., Sparke L. S., Stone J. M., 2002, *MNRAS*, 329, 502
- Madau P., Dickinson M., 2014, *ARAA*, 52, 415
- Mahajan S., et al., 2020, *MNRAS*, 491, 398
- Margalef-Bentabol B., 2023, in Galactic Bars: Driving and Decoding Galaxy Evolution. p. 32, [doi:10.5281/zenodo.8130460](https://doi.org/10.5281/zenodo.8130460)
- Marinova I., Jogee S., 2007, *ApJ*, 659, 1176
- Martig M., Bournaud F., Croton D. J., Dekel A., Teyssier R., 2012, *ApJ*, 756, 26
- Martin G., et al., 2018, *MNRAS*, 476, 2801
- Martini P., Regan M. W., Mulchaey J. S., Pogge R. W., 2003, *ApJ*, 589, 774
- Masters K. L., et al., 2010, *MNRAS*, 405, 783
- Masters K. L., et al., 2011, *MNRAS*, 411, 2026
- Masters K. L., et al., 2012, *MNRAS*, 424, 2180
- Masters K. L., et al., 2019, *MNRAS*, 487, 1808

- 
- McAlpine S., Harrison C. M., Rosario D. J., Alexander D. M., Ellison S. L., Johansson P. H., Patton D. R., 2020, *MNRAS*, 494, 5713
- Melvin T., et al., 2014, *MNRAS*, 438, 2882
- Méndez-Abreu J., Sánchez-Janssen R., Aguerri J. A. L., Corsini E. M., Zarattini S., 2012, *ApJ*, 761, L6
- Miller J. S., 1994, The Kast Double Spectrograph, <https://mthamilton.ucolick.org/techdocs/instruments/kast/Tech%20Report%2066%20KAST%20Miller%20Stone.pdf>
- Miller R. H., Smith B. F., 1979, *ApJ*, 227, 785
- Mo H. J., Mao S., White S. D. M., 1998, *MNRAS*, 295, 319
- Moorthy B. K., Holtzman J. A., 2006, *MNRAS*, 371, 583
- Mulcahey C. R., et al., 2022, arXiv e-prints, p. arXiv:2206.01195
- Mulchaey J. S., Regan M. W., 1997, *ApJ*, 482, L135
- Mullaney J. R., et al., 2012, *ApJ*, 753, L30
- Mullaney J. R., et al., 2015, *MNRAS*, 453, L83
- Nair P. B., Abraham R. G., 2010, *ApJS*, 186, 427
- Navarro J. F., Benz W., 1991, *ApJ*, 380, 320
- Navarro J. F., White S. D. M., 1994, *MNRAS*, 267, 401
- Nedkova K. V., et al., 2024, arXiv e-prints, p. arXiv:2406.14613
- Noguchi M., 1987, *MNRAS*, 228, 635
- O’Ryan D., et al., 2023, *ApJ*, 948, 40
- Oh K., Sarzi M., Schawinski K., Yi S. K., 2011, *ApJS*, 195, 13
- Oh S., Oh K., Yi S. K., 2012, *ApJS*, 198, 4

- Oppenheimer B. D., Davé R., 2006, [MNRAS](#), **373**, 1265
- Osterbrock D. E., 1989, *Astrophysics of gaseous nebulae and active galactic nuclei*. University Science Books
- Osterbrock D. E., De Robertis M. M., 1985, [PASP](#), **97**, 1129
- Parry O. H., Eke V. R., Frenk C. S., 2009, [MNRAS](#), **396**, 1972
- Peng C. Y., Ho L. C., Impey C. D., Rix H.-W., 2002, [AJ](#), **124**, 266
- Peng C. Y., Ho L. C., Impey C. D., Rix H.-W., 2010, [AJ](#), **139**, 2097
- Perlmutter S., et al., 1999, [ApJ](#), **517**, 565
- Pflamm-Altenburg J., Weidner C., Kroupa P., 2007, [ApJ](#), **671**, 1550
- Read J. I., Trentham N., 2005, [Philosophical Transactions of the Royal Society of London Series A](#), **363**, 2693
- Regan M. W., Elmegreen D. M., 1997, [AJ](#), **114**, 965
- Regan M. W., Teuben P. J., 2004, [ApJ](#), **600**, 595
- Riess A. G., et al., 1998, [AJ](#), **116**, 1009
- Rodrigo C., Solano E., 2020, in XIV.0 Scientific Meeting (virtual) of the Spanish Astronomical Society. p. 182
- Rodrigo C., Solano E., Bayo A., 2012, SVO Filter Profile Service Version 1.0, IVOA Working Draft 15 October 2012, [doi:10.5479/ADS/bib/2012ivoa.rept.1015R](https://doi.org/10.5479/ADS/bib/2012ivoa.rept.1015R)
- Rodriguez-Gomez V., et al., 2017, [MNRAS](#), **467**, 3083
- Rosario D. J., Mendel J. T., Ellison S. L., Lutz D., Trump J. R., 2016, [MNRAS](#), **457**, 2703
- Rowlands K., et al., 2012, [MNRAS](#), **419**, 2545
- Sakamoto K., 1996, [ApJ](#), **471**, 173

- 
- Sakamoto K., Okumura S. K., Ishizuki S., Scoville N. Z., 1999, *ApJ*, **525**, 691
- Salim S., et al., 2007, *ApJS*, **173**, 267
- Sánchez S. F., et al., 2004, *ApJ*, **614**, 586
- Sancisi R., Fraternali F., Oosterloo T., van der Hulst T., 2008, *A&AR*, **15**, 189
- Sandage A., 1965, *ApJ*, **141**, 1560
- Sandage A., 1986, in *Star-forming Dwarf Galaxies and Related Objects*. pp 31–40
- Sandage A., Freeman K. C., Stokes N. R., 1970, *ApJ*, **160**, 831
- Satyapal S., Böker T., Mcalpine W., Gliozzi M., Abel N. P., Heckman T., 2009, *ApJ*, **704**, 439
- Satyapal S., et al., 2016, *ApJ*, **827**, 58
- Schawinski K., Thomas D., Sarzi M., Maraston C., Kaviraj S., Joo S.-J., Yi S. K., Silk J., 2007, *MNRAS*, **382**, 1415
- Schawinski K., et al., 2009, *MNRAS*, **396**, 818
- Schawinski K., Treister E., Urry C. M., Cardamone C. N., Simmons B., Yi S. K., 2011, *ApJ*, **727**, L31
- Schawinski K., Simmons B. D., Urry C. M., Treister E., Glikman E., 2012, *MNRAS*, **425**, L61
- Schawinski K., Koss M., Berney S., Sartori L. F., 2015, *MNRAS*, **451**, 2517
- Schaye J., et al., 2015, *MNRAS*, **446**, 521
- Schmidt M., 1963, *Nature*, **197**, 1040
- Schnorr-Müller A., Storch-Bergmann T., Nagar N. M., Ferrari F., 2014, *MNRAS*, **438**, 3322
- Schwarzschild K., 1916, *Sitzungsberichte der Königlich Preussischen Akademie der Wissenschaften*, pp 189–196

- 
- Schweizer F., 1990, in Wielen R., ed., , Dynamics and Interactions of Galaxies. pp 60–71
- Sellwood J. A., 1981, *A&A*, **99**, 362
- Sellwood J. A., 2014, *Reviews of Modern Physics*, **86**, 1
- Seo W.-Y., Kim W.-T., Kwak S., Hsieh P.-Y., Han C., Hopkins P. F., 2019, *ApJ*, **872**, 5
- Sérsic J. L., 1968, Atlas de Galaxias Australes. Observatorio Astrònomico
- Seyfert C. K., 1943, *ApJ*, **97**, 28
- Shankar F., Weinberg D. H., Miralda-Escudé J., 2009, *ApJ*, **690**, 20
- Shapiro S. S., Wilk M. B., 1965, *Biometrika*, **52**, 591
- Shen J., Sellwood J. A., 2004, *ApJ*, **604**, 614
- Sheth K., et al., 2008, *ApJ*, **675**, 1141
- Shlosman I., Frank J., Begelman M. C., 1989, *Nature*, **338**, 45
- Shlosman I., Begelman M. C., Frank J., 1990, *Nature*, **345**, 679
- Silk J., 2013, *ApJ*, **772**, 112
- Silva-Lima L. A., Martins L. P., Coelho P. R. T., Gadotti D. A., 2022, *A&A*, **661**, A105
- Silverman J. D., et al., 2009, *ApJ*, **696**, 396
- Simmons B. D., Urry C. M., 2008, *ApJ*, **683**, 644
- Simmons B. D., Van Duyne J., Urry C. M., Treister E., Koekemoer A. M., Grogin N. A., GOODS Team 2011, *ApJ*, **734**, 121
- Simmons B. D., Urry C. M., Schawinski K., Cardamone C., Glikman E., 2012, *ApJ*, **761**, 75

- 
- Simmons B. D., et al., 2013, [MNRAS](#), 429, 2199
- Simmons B. D., et al., 2014, [MNRAS](#), 445, 3466
- Simmons B. D., et al., 2017a, [MNRAS](#), 464, 4420
- Simmons B. D., Smethurst R. J., Lintott C., 2017b, [MNRAS](#), 470, 1559
- Skibba R. A., et al., 2009, [MNRAS](#), 399, 966
- Skibba R. A., et al., 2012, [MNRAS](#), 423, 1485
- Skrutskie M. F., et al., 2006, [AJ](#), 131, 1163
- Slater R., et al., 2019, [A&A](#), 621, A83
- Smethurst R. J., Simmons B. D., Lintott C. J., Shanahan J., 2019, [MNRAS](#), 489, 4016
- Smethurst R. J., et al., 2021, [MNRAS](#), 507, 3985
- Smethurst R. J., et al., 2022, [MNRAS](#), 510, 4126
- Smethurst R. J., et al., 2024, [MNRAS](#), 527, 10855
- Sommer-Larsen J., Götz M., Portinari L., 2003, [ApJ](#), 596, 47
- Sparke L. S., Sellwood J. A., 1987, [MNRAS](#), 225, 653
- Spinoso D., Bonoli S., Dotti M., Mayer L., Madau P., Bellovary J., 2017, [MNRAS](#), 465, 3729
- Steinmetz M., Navarro J. F., 2002, [NA](#), 7, 155
- Stern D., et al., 2005, [ApJ](#), 631, 163
- Student 1908, *Biometrika*, 6, 1
- Taylor M. B., 2005, in Shopbell P., Britton M., Ebert R., eds, *Astronomical Society of the Pacific Conference Series Vol. 347, Astronomical Data Analysis Software and Systems XIV*. p. 29

- 
- Tody D., 1986, in Crawford D. L., ed., Society of Photo-Optical Instrumentation Engineers (SPIE) Conference Series Vol. 627, Instrumentation in astronomy VI. p. 733, [doi:10.1117/12.968154](https://doi.org/10.1117/12.968154)
- Tody D., 1993, in Hanisch R. J., Brissenden R. J. V., Barnes J., eds, Astronomical Society of the Pacific Conference Series Vol. 52, Astronomical Data Analysis Software and Systems II. p. 173
- Toomre A., 1964, [ApJ](#), **139**, 1217
- Toomre A., Toomre J., 1972, [ApJ](#), **178**, 623
- Torbaniuk O., Paolillo M., Carrera F., Cavuoti S., Vignali C., Longo G., Aird J., 2021, [MNRAS](#), **506**, 2619
- Trump J. R., et al., 2015, [ApJ](#), **811**, 26
- Urrutia T., Lacy M., Becker R. H., 2008, [ApJ](#), **674**, 80
- Urry C. M., Padovani P., 1995, [PASP](#), **107**, 803
- Veilleux S., Osterbrock D. E., 1987, [ApJS](#), **63**, 295
- Virtanen P., et al., 2020, [Nature Methods](#), **17**, 261
- Voges W., et al., 1999, [A&A](#), **349**, 389
- Walmsley M., et al., 2022, [MNRAS](#), **509**, 3966
- Walmsley M., et al., 2023a, [MNRAS](#), p. stad2919
- Walmsley M., et al., 2023b, [The Journal of Open Source Software](#), **8**, 5312
- White S. D. M., Frenk C. S., 1991, [ApJ](#), **379**, 52
- Willett K. W., et al., 2013, [MNRAS](#), **435**, 2835
- Willett K. W., et al., 2017, [MNRAS](#), **464**, 4176
- Willmer C. N. A., et al., 2006, [ApJ](#), **647**, 853

Wright E. L., et al., 2010, [AJ](#), **140**, 1868

York D. G., et al., 2000, [AJ](#), **120**, 1579

Zee W.-B. G., Paudel S., Moon J.-S., Yoon S.-J., 2023, [ApJ](#), **949**, 91

al Sūfī A. a.-R., 964, Suwar al-kawākib

de Vaucouleurs G., 1959, [Handbuch der Physik](#), **53**, 275

de Vaucouleurs G., 1963, [ApJS](#), **8**, 31

van Dokkum P. G., 2001, [PASP](#), **113**, 1420